

Gate-based superconducting quantum computing

Sangil Kwon,^{1, a)} Akiyoshi Tomonaga,^{1,2} Gopika Lakshmi Bhai,^{1,2} Simon J. Devitt,³ and Jaw-Shen Tsai^{1,2}

¹⁾*Department of Physics, Tokyo University of Science, Shinjuku, Tokyo 162-0825, Japan*

²⁾*RIKEN, Center for Emergent Matter Science (CEMS), Wako, Saitama 351-0198, Japan*

³⁾*Centre for Quantum Software and Information (QSI), Faculty of Engineering and Information Technology, University of Technology Sydney, Sydney, NSW, 2007, Australia*

(Dated: 16 May 2022)

In this tutorial, we introduce basic conceptual elements to understand and build a gate-based superconducting quantum computing system.

CONTENTS

I. Introduction	2	2. Josephson Parametric Amplifier	23
II. Universal Quantum Computing System	3	C. Single-Qubit Gate	25
A. Essential Elements	3	D. Two-Qubit Gate	26
1. Quantum Bit	3	1. iSWAP: Coherent Exchange	26
2. Quantum Gate	4	2. iSWAP and bSWAP: Parametric Coupling	27
B. Structure	4	3. CZ: Adiabatic Excursion	28
III. Superconducting Qubit	5	4. CZ: Coherent Exchange and Parametric Coupling	29
A. Design Criteria	5	5. CR: All Microwave Control	29
B. Josephson Junction	5	E. Initialization	31
C. Elementary Circuits	6	1. Entropy Dumping	31
1. Generic Hamiltonian	6	2. Measurement-Based Initialization	31
2. Island-Based Qubit	7	VII. Quantum Error Correction	31
3. Loop-Based Qubit	7	A. Introduction	31
IV. Effect of Noise	10	B. Surface Code	33
A. Relaxation	10	1. Definition	33
1. Concept	10	2. Logical Qubit Construction	34
2. Thermalization	10	3. Error Detection and Correction	34
3. Dephasing	12	4. Logical Gate Operation	35
B. Noise-Resilient Designs	12	C. Proposed Device Architectures	37
1. Island-Based Qubit	12	VIII. Characterizing a Quantum System	37
2. Loop-Based Qubit	13	A. Spectroscopy	38
V. Coupling	14	1. Single-Tone Spectroscopy	38
A. Two Coupled Classical Oscillators	14	2. Two-Tone Spectroscopy	38
B. From Circuit to Atom	16	3. Dispersive Shift	38
1. Qubit, Resonator, and Somewhere between Them	16	B. Time-Domain Measurement	39
2. Qubit-Resonator Coupling	17	1. Rabi Oscillation	39
3. Qubit-Qubit Coupling	18	2. Relaxation Time: T_1	40
C. Strong (Transverse) Coupling	19	3. Relaxation Time: T_2	40
VI. Implementation of Quantum Computation	20	IX. Controlling a Quantum System	40
A. Equation of Motion	20	A. Elementary Pulse Shaping	41
B. Readout	21	1. Excitation Bandwidth	41
1. Dispersive Readout	21	2. Pulse Distortion	42
		B. Numerical Optimization	42
		1. GRAPE Algorithm	43
		2. Example: Controlling Excitation Bandwidth	44
		C. Refocusing Technique	45
		D. Evaluation of Gate Operation	47
		Acknowledgments	49

^{a)}Electronic mail: kwon2866@gmail.com

I. INTRODUCTION

Quantum computing is considered as a next-generation information processing technology. The basic element of a quantum computing system is a quantum bit, often called a qubit. Over the last decades, considerable progress has been made toward realizing quantum computing systems by physically implementing a qubit in various systems such as ion traps, quantum dots, nuclear spins, and cavity quantum electrodynamics. The scalability of such a qubit is considered to be a prerequisite for a practical quantum computer of the future. In this regard, a solid-state qubit has been considered to be indispensable. Superconducting quantum systems are one of the most promising candidates because, in these systems, qubits are intrinsically integrated in a solid-state device, and their wide range of choice for the qubit parameters is a considerable advantage, which in turn gives flexibility in designing such quantum circuits.

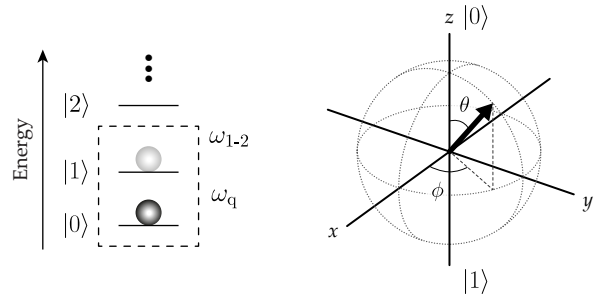
In this tutorial, we try to provide basic conceptual elements to understand and build a potentially scalable superconducting quantum computing system based on gate operations. The logical flow is roughly from principle to practice. After introducing the qubit and structure of a universal quantum computing system (Sec. II), we explain a superconducting circuit that can be used as a qubit (Secs. III and IV) and how to implement basic functions that are required for quantum computation (Secs. V and VI). Then, we introduce a quantum error correction scheme, called the surface code, that is believed to be suitable for superconducting qubit systems (Sec. VII). Lastly, we deal with practical topics, such as how to characterize and control a quantum system (Secs. VIII and IX).

Since this is a tutorial, the topics covered here are very selective rather than comprehensive. Hence, we cite references that are more accessible to readers. Another reason for this is that many concepts and experimental techniques for superconducting circuits were originally developed in other branches of science—tracing all historical literature is not meaningful for readers. For comprehensive reviews on this field, see Refs. 1–6.

Regarding the difficulty of this tutorial, we assume that readers are somewhat familiar with quantum mechanics, especially the Dirac notation and the occupation number representation (second quantization), and elementary statistical mechanics, such as the Boltzmann distribution. Since superconducting quantum computing systems are electrical circuits, knowledge on basic electrical engineering will be helpful, especially the S-parameters. However, readers do not need to be masters of these topics. Reading this tutorial does not require deep physical insights—it is more like learning a new language.⁷ Once you get used to it, you will enjoy it.

Before entering the main part, we would like to point out that the word “scaling” in quantum engineering is different from that in the semiconductor industry. In the semiconductor industry, scaling means reducing the size

(a) Bloch sphere representation of the qubit state



(b) Changing a frame of reference

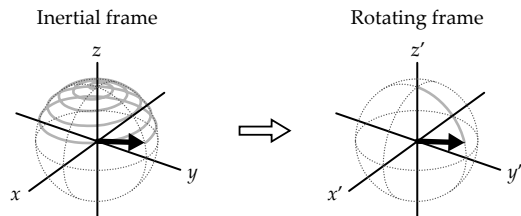


FIG. 1. (a) Bloch sphere representation of the qubit state. In the energy level diagram, the two lowest states in the dashed boundary are used for computation. This subspace is called the computational subspace. To selectively control these two levels, $\omega_q \neq \omega_{1-2}$ is required, where ω_q is the transition frequency between $|0\rangle$ and $|1\rangle$, and ω_{1-2} is the transition frequency between $|1\rangle$ and $|2\rangle$. (b) In the rotating frame, “trivial evolution” is eliminated such that we can concentrate on the dynamics we are interested in. The axes with the prime indicate that we are in the rotating frame. As in the majority of the literature, all Bloch spheres in this tutorial are in the rotating frame.

of the information processing device used, such as a transistor, and the energy cost per bit, so that we can integrate more and more devices into a chip. In quantum engineering, “scaling” simply means adding more qubits because physical quantities involved in operations of a superconducting quantum computing platform, such as the charge of a Cooper pair and magnetic flux quantum, are already at the quantum limit, and a quantum information processing device is lossless. Thus, the dramatic size reduction as demonstrated in Moore’s law may not be expected for superconducting qubits.

A set of formulas for deriving equations in this tutorial are summarized in Table V at the end of the main text.

II. UNIVERSAL QUANTUM COMPUTING SYSTEM

A. Essential Elements

1. Quantum Bit

A qubit is a two-level system whose quantum mechanical state displays phase coherence between two basis states, $|0\rangle$ and $|1\rangle$. The phase coherence between two quantum states can be defined as follows. The quantum state of a qubit, in general, is a linear superposition of the two basis states $|0\rangle$ and $|1\rangle$,

$$|\psi\rangle = \alpha|0\rangle + \beta|1\rangle, \quad (1)$$

where α and β are complex numbers and $|\alpha|^2 + |\beta|^2 = 1$. We can define the relative quantum phase φ of the two basis states as

$$\varphi \equiv \arg(\alpha^*\beta). \quad (2)$$

If φ of a given quantum mechanical state has a definite value, we say that a given quantum mechanical state displays phase coherence (often just called coherence) between the states $|0\rangle$ and $|1\rangle$.

An arbitrary qubit state can also be expressed in the density matrix form:

$$\hat{\rho} = |\psi\rangle\langle\psi| = \begin{array}{cc} & \langle 0| & \langle 1| \\ \begin{array}{c} |0\rangle \\ |1\rangle \end{array} & \begin{pmatrix} |\alpha|^2 & \alpha\beta^* \\ \alpha^*\beta & |\beta|^2 \end{pmatrix} \end{array}, \quad (3)$$

where kets and bras around the density matrix indicate the basis. Note that the diagonal elements represent the populations of the basis states and the off-diagonal elements represent the phase coherences between these states. Hence, the populations and coherences depend on the chosen basis.

Note that a qubit and a spin-1/2 system are mathematically identical. This allows us to represent the qubit state conveniently as an arrow, called the Bloch vector, in the Bloch sphere [Fig. 1(a)]. Conventionally, the qubit quantization axis is set as the z -axis, and the north and south poles represent $|0\rangle$ and $|1\rangle$, respectively. Hence, the longitudinal component of the Bloch vector corresponds to the polarization of the qubit, and the transverse component corresponds to the coherence between the two basis states.

In spherical coordinates, the Bloch vector \vec{s} can be written as

$$\vec{s} = (\sin\theta \cos\phi, \sin\theta \sin\phi, \cos\theta), \quad (4)$$

where θ and ϕ are the polar and azimuthal angles, respectively [Fig. 1(a)]. Conversion from the Bloch vector to the density matrix can be done by using the Pauli

matrices:

$$\begin{aligned} \hat{\rho} &= \frac{1}{2}(\hat{I} + s_x\hat{\sigma}_x + s_y\hat{\sigma}_y + s_z\hat{\sigma}_z) \\ &= \begin{pmatrix} \cos^2\frac{\theta}{2} & e^{-i\phi}\cos\frac{\theta}{2}\sin\frac{\theta}{2} \\ e^{i\phi}\cos\frac{\theta}{2}\sin\frac{\theta}{2} & \sin^2\frac{\theta}{2} \end{pmatrix}. \end{aligned} \quad (5)$$

One possible mapping between Eqs. (3) and (5) is $\alpha = \cos(\theta/2)$ and $\beta = e^{i\phi}\sin(\theta/2)$.

The rotation of the Bloch vector with the angle η about the k -axis is done by the rotation operator $\hat{R}_k(\eta)$:

$$\hat{R}_k(\eta) \equiv \exp\left(-i\eta\frac{\hat{\sigma}_k}{2}\right) = \cos\left(\frac{\eta}{2}\right)\hat{I} - i\sin\left(\frac{\eta}{2}\right)\hat{\sigma}_k \quad (6)$$

Here, we used the formula

$$\begin{aligned} \exp(-i\eta\hat{A}) &= \left(1 - \frac{\eta^2}{2!} + \dots\right)\hat{I} - i\left(\eta - \frac{\eta^3}{3!} + \dots\right)\hat{A} \\ &= \cos(\eta)\hat{I} - i\sin(\eta)\hat{A}, \quad \text{if } \hat{A}^2 = \hat{I}. \end{aligned} \quad (7)$$

When we use the Bloch sphere, we are free to choose a frame of reference. In the majority of the literature, including this tutorial, the dynamics of the qubit state are described in the rotating frame [Fig. 1(b)]. To determine the rotating frame frequency, we have to know the dynamics we want to focus on. Then, we eliminate the trivial evolution by performing a unitary transformation, which changes our frame of reference. Note that this is conceptually and mathematically identical to switching into the interaction picture. Usually, the qubit frequency, the resonator frequency (see Sec. VB), or the external drive frequency (Sec. VIC) is chosen as the rotating frame frequency.

A qubit is often implemented by the two lowest states of a quantum system, such as (artificial or natural) atoms [Fig. 1(a)]. This subspace is called the computational subspace. In general, any Hilbert space whose dimension is truncated into two can be used as a qubit. This generalized definition of a qubit is essential for constructing a logical qubit (Sec. VII).

In this tutorial, the notations denoting the qubit states, $\{|0\rangle, |1\rangle, |2\rangle$ (higher excitation level) and $\{|g\rangle, |e\rangle, |f\rangle\}$, are used interchangeably and are not to be confused with the photon or the charge number states. In addition, ω_q , which we call the qubit frequency, is the transition frequency between $|0\rangle$ and $|1\rangle$, and ω_{i-j} (with a hyphen in the subscript) is the transition frequency between $|i\rangle$ and $|j\rangle$; ω_{ij} (without a hyphen in the subscript) indicates the energy level of the two-qubit state, $|i\rangle \otimes |j\rangle$ (or $|ij\rangle$ in the short form).

A generic two-qubit state can be written as

$$|\psi\rangle = \alpha|00\rangle + \beta|01\rangle + \gamma|10\rangle + \delta|11\rangle, \quad (8)$$

where α , β , γ , and δ are complex numbers and $|\alpha|^2 +$

TABLE I. Universal quantum gate set. $\hat{R}_k(\eta)$ ($k = x, y, z$) is the rotation operator defined in Eq. (6). $|\psi\rangle_{t(c)}$ indicates the quantum state of the target (control) qubit. \hat{X} is the X gate in the operator form.

Name	Function	Symbol	Matrix
Pauli- X (X)	$\hat{R}_x(\pi)$	$\text{---}\boxed{X}\text{---}$	$\begin{pmatrix} 0 & 1 \\ 1 & 0 \end{pmatrix}$
Pauli- Y (Y)	$\hat{R}_y(\pi)$	$\text{---}\boxed{Y}\text{---}$	$\begin{pmatrix} 0 & -i \\ i & 0 \end{pmatrix}$
Pauli- Z (Z)	$\hat{R}_z(\pi)$	$\text{---}\boxed{Z}\text{---}$	$\begin{pmatrix} 1 & 0 \\ 0 & -1 \end{pmatrix}$
Hadamard (H)	$\hat{R}_x(\pi)\hat{R}_x(\pi/2)$	$\text{---}\boxed{H}\text{---}$	$\frac{1}{\sqrt{2}}\begin{pmatrix} 1 & 1 \\ 1 & -1 \end{pmatrix}$
Phase (S)	$\hat{R}_z(\pi/2)$	$\text{---}\boxed{S}\text{---}$	$\begin{pmatrix} 1 & 0 \\ 0 & i \end{pmatrix}$
$\pi/8$ (T)	$\hat{R}_z(\pi/4)$	$\text{---}\boxed{T}\text{---}$	$\begin{pmatrix} 1 & 0 \\ 0 & e^{i\pi/4} \end{pmatrix}$
Controlled-NOT (CNOT)	$\hat{X} \psi\rangle_t$ if $ \psi\rangle_c = 1\rangle$	$\begin{array}{c} \bullet \\ \text{---}\bigoplus\text{---} \end{array}$	$\begin{pmatrix} 1 & 0 & 0 & 0 \\ 0 & 1 & 0 & 0 \\ 0 & 0 & 0 & 1 \\ 0 & 0 & 1 & 0 \end{pmatrix}$

$|\beta|^2 + |\gamma|^2 + |\delta|^2 = 1$. In the density matrix form,

$$\hat{\rho} = \begin{array}{c} |00\rangle \\ |01\rangle \\ |10\rangle \\ |11\rangle \end{array} \begin{pmatrix} \langle 00| & \langle 01| & \langle 10| & \langle 11| \\ \alpha|\alpha|^2 & \alpha\beta^* & \alpha\gamma^* & \alpha\delta^* \\ \alpha^*\beta & |\beta|^2 & \beta\gamma^* & \beta\delta^* \\ \alpha^*\gamma & \beta^*\gamma & |\gamma|^2 & \gamma\delta^* \\ \alpha^*\delta & \beta^*\delta & \gamma^*\delta & |\delta|^2 \end{pmatrix}. \quad (9)$$

2. Quantum Gate

A quantum gate is a discrete control acting on qubits inducing the unitary evolution of the quantum states of the qubits. Quantum computation is basically a series of quantum gate operations.

Consider a closed quantum system described by the time-independent Hamiltonian \hat{H} . The time evolution of such a system is described by a unitary operator $\hat{U}(t)$, which is called the time-evolution operator or the propagator:^{8,9}

$$|\psi(t)\rangle = \hat{U}(t) |\psi(0)\rangle. \quad (10)$$

The Schrödinger equation connects $\hat{U}(t)$ and \hat{H} :

$$\hat{U}(t) = e^{-i\hat{H}t/\hbar}. \quad (11)$$

Thus, a gate operation is implemented by engineering the system Hamiltonian such that the resulting unitary evolution of the qubits implements the target gate.

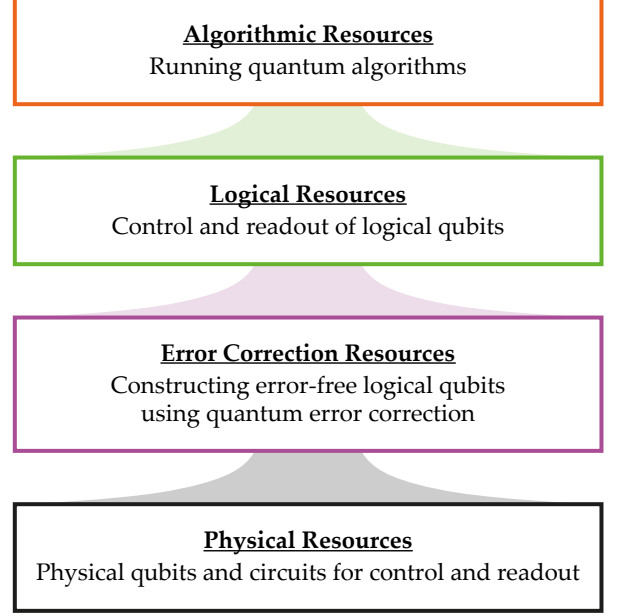


FIG. 2. Structure of a universal quantum computing system.

Any multiqubit gate operation can be decomposed into a set of single-qubit and controlled-NOT (CNOT) gates. Thus, the gate set {single-qubit gates, CNOT} is called a universal quantum gate set. An arbitrary single-qubit gate can be well approximated by the discrete gate set $\{H, S, T\}$ (Solovay-Kitaev theorem¹⁰). Hence, we can rewrite a universal gate set as $\{H, S, T, \text{CNOT}\}$. The definitions of these gates and other popular gates are summarized in Table I.

Among these universal quantum gates, the quantum gates generated by the H , S , and CNOT gates form a group called the Clifford group. This group is important in quantum computation, especially for quantum error correction (Sec. VII) and efficient gate qualification (Sec. IX D). However, it is known that a quantum computer operated by only Clifford gates can be simulated efficiently on a probabilistic classical computer (Gottesman-Knill theorem¹⁰). Thus, a non-Clifford gate, such as the T gate, is required to show the advantage of quantum computation.

B. Structure

A gate-operation-based, universal, and scalable superconducting quantum computer will likely have the following structure (Fig. 2):^{11,12}

Physical resources: This layer is a collection of physical qubits and necessary circuits for the control and readout of the physical qubits.

Error correction resources: In this layer, errors act-

ing on quantum information stored in a set of physical qubits are corrected. This operation produces a single error-free logical qubit. For this, high fidelity controls, such as initialization, gate operation, readout, and feedback, for physical qubits are required.

Logical resources: Initialization, gate operation, and readout of logical qubits are performed in this layer.

Algorithmic resources: Quantum algorithms, such as Shor's factoring and Grover's search algorithms, are performed in this layer.

In this tutorial, the physical resources, the error correction resources, and part of the logical resources are briefly covered. For quantum algorithms, see the standard textbooks on quantum computation, such as Refs. 10 and 13.

III. SUPERCONDUCTING QUBIT

A. Design Criteria

A superconducting qubit is the two lowest energy eigenstates of an artificial atom made of a superconducting circuit. To be a useful qubit, the circuit must be designed to satisfy the following conditions:

1. *Proper operating frequency range:* A qubit must have a transition frequency that is significantly higher than the thermal energy of a typical solid-state system to observe quantum nature. The only continuous refrigeration method for solid state devices below 0.3 K is to use a dilution refrigerator, whose base temperature is usually about 10 mK (~ 200 MHz). This means that the transition frequency of a qubit must be at least a few gigahertz. At the same time, the qubit transition frequency should be sufficiently lower than the superconducting energy gap of the host superconductor so as not to excite quasiparticles. For aluminum, which is the most popular material for superconducting qubit systems, the energy gap is about 20 GHz.
2. *Large anharmonicity:* To be a well-defined two-level system, a qubit should have anharmonicity $\alpha \equiv \omega_{1-2} - \omega_q$ of at least ~ 100 MHz to perform a reasonably fast gate operation. (See Sec. IX A 1 for the gate time and frequency selectivity.) Recently, it has been found that having a third level in an accessible frequency range can be beneficial, such as for initialization or two-qubit gate operation. (See Secs. VID and VIE 1.)
3. *Long coherence time:* The assigned quantum state should last for a long time compared with the time for gate operations.
4. *Ease of coupling:* For readout and (multi)qubit gate operation, a reasonably strong coupling between

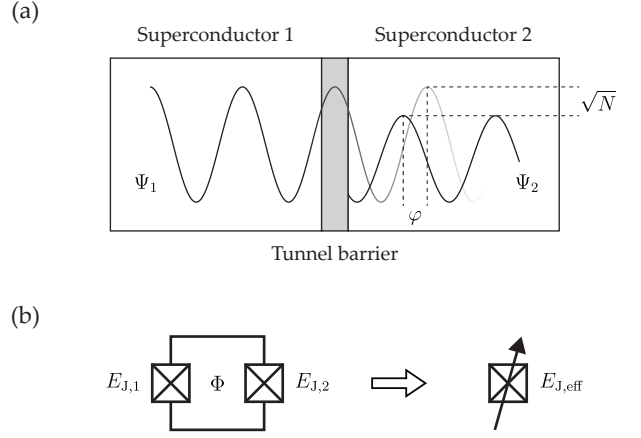


FIG. 3. (a) Schematic diagram of a Josephson junction where a pair of superconductors are weakly coupled via an oxide tunnel barrier. The phase and the number difference of the macroscopic wavefunctions Ψ_1 and Ψ_2 fully determine the physics of the junction. (b) A DC SQUID can be considered as a variable Josephson junction tuned by an external magnetic flux Φ . The symbol of a cross in a square represents a Josephson junction.

a qubit and another quantum system, such as a resonator or neighboring qubit, should be achieved easily.

5. *Ease of control:* The quantum state should be brought to a superposition easily and straightforwardly by an external mean.
6. *Ease of fabrication:* A qubit should be easy to fabricate with standard nanotechnology for good reproducibility.

B. Josephson Junction

A superconductor is a macroscopic quantum mechanical system in the sense that it can be described by a single macroscopic wavefunction, i.e., the order parameter Ψ . However, this property is not a sufficient condition for being a qubit; we need a confinement potential to have discrete energy eigenstates such as electrons in the Coulomb potential forming an atom. Moreover, to control the two lowest energy eigenstates selectively, the potential must be anharmonic to have distinct energy separation between eigenstates.

The solution for discrete energy eigenstates is to make an electrical circuit. In a superconducting circuit, the quantized energy level emerges from the quantization of the charge and the magnetic flux stored in various electrical components just like the position and the momentum of electrons in a real atom.¹

¹ Since the charge and the magnetic flux are collective coordinates

The solution for the anharmonicity is a Josephson junction where a pair of superconductors are weakly coupled [Fig. 3(a)]. In a superconducting circuit, a Josephson junction acts as a nonlinear inductor, resulting in an anharmonic potential. Since a superconductor is a macroscopic quantum mechanical system, only two quantities are required to describe the physics of a Josephson junction: the number imbalance of electrons N and the relative phase φ between the two superconductors. Here, N corresponds to the difference in $|\Psi|^2$ of the two superconductors. The equations of motion regarding these two quantities, called the Josephson equations, are given by¹⁵

$$\frac{dN(t)}{dt} = \frac{2E_J}{\hbar} \sin \varphi(t) \quad \text{and} \quad \frac{d\varphi(t)}{dt} = -\frac{2e}{\hbar} V(t), \quad (12)$$

where E_J is the Josephson energy, which is a measure of the ability of Cooper pairs to tunnel through the junction; \hbar is the reduced Planck constant; e is the magnitude of the charge carried by a single electron; and V is the voltage difference maintained across the junction. The popular form of the left equation in Eq. (12) is¹⁶

$$I_s(t) = I_c \sin \varphi(t), \quad (13)$$

where I_s is a zero-voltage supercurrent flow through the junction and $I_c (= 2eE_J/\hbar)$ is the maximum current that can flow through the junction, i.e., the critical current of the junction.

Here, we point out that a DC Superconducting Quantum Interference Device (DC SQUID), which consists of two Josephson junctions and a superconducting loop [Fig. 3(b)], can be considered as a variable Josephson junction whose effective Josephson energy $E_{J,\text{eff}}$ as a function of the external flux bias Φ is given by

$$E_{J,\text{eff}}(\varphi_{\text{ext}}) = \sqrt{E_{J,1}^2 + E_{J,2}^2 + 2E_{J,1}E_{J,2} \cos \varphi_{\text{ext}}}, \quad (14)$$

where $\varphi_{\text{ext}} (\equiv 2\pi\Phi/\Phi_0)$ is the phase offset due to the external flux bias. This idea is useful for making tunable superconducting devices.

C. Elementary Circuits

1. Generic Hamiltonian

We can categorize elementary circuits of superconducting qubits into two groups, an island and a loop (Fig. 4). In the early literature, these two kinds of qubits were called a charge qubit and a flux qubit, respectively, on the basis of the spread of the wavefunctions in the number (charge) and phase (flux) bases [typical wavefunctions of a charge qubit are shown in Fig. 5(d)].¹⁷ How-

that represent the cooperative motion of large numbers of electrons, the circuit quantization is essentially phenomenological.¹⁴

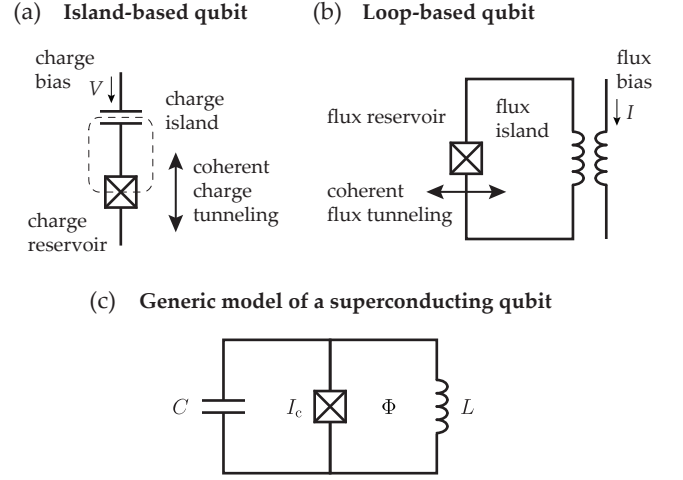


FIG. 4. (a) and (b) Elementary circuits of a superconducting qubit. The dashed boundary line indicates the charge island. In a certain parameter range, their operations as qubits can be understood as the coherent tunneling of charge or flux (see Secs. III C 2 and III C 3). (c) Parallel circuit composed of an inductor with L , a capacitor with C , and a Josephson junction with the critical current I_c as a generic model of a superconducting qubit.

ever, such a classification is valid only for a certain parameter range; it does not work well for sophisticated qubits whose wavefunctions often show exotic distributions in both the number and the phase bases. Therefore, we simply categorize circuits of superconducting qubits based on the geometry. Then, we will show how the qubit properties change as we tune the circuit parameters. The knowledge acquired in this way can also be used for analyzing more complex qubits.

We introduce a Hamiltonian for a parallel circuit composed of a capacitor with the capacitance C including the intrinsic capacitance of a junction, an inductor with the inductance L , and a Josephson junction, as a generic model of a superconducting qubit [Fig. 4(c)]. This particular circuit is easily quantized by treating N and φ as the operators \hat{N} and $\hat{\varphi}$. (The standard introduction to superconducting circuit quantization is Ref. 18.) Here, the number operator \hat{N} is conjugate to the phase operator $\hat{\varphi}$: $\hat{N} = -i\partial/\partial\hat{\varphi}$.² The resulting circuit Hamiltonian $\hat{\mathcal{H}}_q$ is given by

$$\hat{\mathcal{H}}_q = 4E_C(\hat{N} - N_{\text{ext}})^2 + \frac{1}{2}E_L\hat{\varphi}^2 - E_J \cos(\hat{\varphi} - \varphi_{\text{ext}}), \quad (15)$$

² They satisfy the relation $e^{i\hat{\varphi}}\hat{N}e^{-i\hat{\varphi}} = \hat{N} - 1$. The popular form of this relation is $[\hat{\varphi}, \hat{N}] = i$. However, this form is not mathematically rigorous because the phase operator is not Hermitian. It holds approximately only if \hat{N} and $\hat{\varphi}$ are the *relative* number and phase operators between two superconductors, and this number imbalance of electrons is much less than the number of electrons in each superconductor. For details, see Refs. 15 and 19.

where $E_C(\equiv e^2/2C)$ is the capacitive energy, which is the energy cost to charge a capacitor with a single electron (the factor of 4 comes from the Cooper pairing), and $E_L[\equiv (\Phi_0/2\pi)^2/L]$ is the inductive energy, which is the energy cost to “charge” an inductor with a single flux quantum Φ_0 . The E_J term, which represents the energy stored in the junction, was obtained by integrating the electrical work $\int I_s V dt$ with Eqs. (12) and (13). Lastly, N_{ext} is the charge offset due to the external voltage bias and $\varphi_{\text{ext}}(\equiv 2\pi\Phi/\Phi_0)$ is the phase offset due to the external flux bias Φ . Inserting this phase offset in the Josephson junction term is based on the assumption that a magnetic flux penetrates into the loop through the junction, not through the inductor.

Equation (15) suggests that characteristics of a superconducting qubit can be engineered by three circuit parameters, E_J , E_C , and E_L . In the following subsections, we explore how these circuit parameters determine the basic properties of a qubit.

2. Island-Based Qubit

The Hamiltonian of an island-based qubit is Eq. (15) in the $E_L \rightarrow 0$ and $\varphi_{\text{ext}} \rightarrow 0$ limits:

$$\hat{H}_q = 4E_C(\hat{N} - N_{\text{ext}})^2 - E_J \cos \hat{\varphi}. \quad (16)$$

Therefore, the properties of an island-based qubit are mainly determined by the ratio E_J/E_C .

In the small E_J/E_C limit, the E_C term is dominant in Eq. (15); as a result, the wavefunctions are localized in the number basis as shown in Fig. 5(d), suggesting that the number basis will be more convenient to describe the physics in this regime. In Fig. 5(a), the gray lines indicate the E_C term associated with $|N=0\rangle$ and $|\pm 1\rangle$. At $N_{\text{ext}} = 0.5$, $|N=0\rangle$ and $|1\rangle$ are energetically degenerated. Here, the E_J term hybridizes these two states via coherent charge tunneling [Fig. 4(a)], resulting in an anticrossing whose size is approximately E_J . At zero bias, a similar, but significantly smaller, hybridization occurs between $|N=-1\rangle$ and $|1\rangle$. This results in the first excitation level at $\approx 4E_C$.

As E_J/E_C increases, the contribution from the anticrossing dominates [Fig. 5(b)]; eventually, in the large E_J/E_C limit, the energy levels become flat, i.e., insensitive to N_{ext} [Fig. 5(c)]. In this regime, the wavefunctions are localized in the phase basis as shown in Fig. 5(e); hence, it is reasonable to treat the E_J term in Eq. (15) as the periodic potential and the E_C term as the kinetic term. In addition, since the kinetic term is much less than the potential term ($E_J/E_C \gg 1$), the displacement in the phase basis during the evolution of the qubit state is small. Thus, as depicted in Fig. 5(f), we can approximate the periodic potential (solid line) as a weakly nonlinear harmonic potential (dashed line). Then, the qubit frequency can be obtained by approximating Eq. (16) as a

quantum harmonic oscillator ($\cos \hat{\varphi} \approx 1 - \hat{\varphi}^2/2$),

$$\hat{H}_q \approx 4E_C \hat{N}^2 + \frac{1}{2} E_J \hat{\varphi}^2, \quad (17)$$

where N_{ext} is ignored because the energy levels are insensitive to N_{ext} . By comparing Eq. (17) with a standard spring-block harmonic oscillator with the spring constant k and the mass m , we obtain $\omega_q \approx \sqrt{8E_J E_C}/\hbar$ from $\omega_0 = \sqrt{k/m}$, where ω_0 is the resonance frequency of the spring-block oscillator. Since we are considering the regime where $\hat{\varphi}$ is localized, C corresponds to m , and L_J^{-1} corresponds to k , where $L_J[\equiv (\Phi_0/2\pi)^2/E_J]$ is the effective inductance of the junction. Moreover, in this large E_J/E_C regime, the anharmonicity will decrease with an increase in E_J/E_C because the Hamiltonian [Eq. (16)] becomes closer to that of a quantum harmonic oscillator [Eq. (17)] in this direction.

More systematic plots regarding the two observations, (i) the flattening of the energy band and (ii) the suppression of the anharmonicity in the large E_J/E_C limit, are given in Fig. 5(g) and (h), respectively. Note that the difference between the transition frequencies at $N_{\text{ext}} = 0$ and 0.5, denoted by $\Delta\omega_q$, decreases exponentially as shown in the inset of Fig. 5(g). This indicates that the energy levels are completely flat if $E_J/E_C \gtrsim 50$.

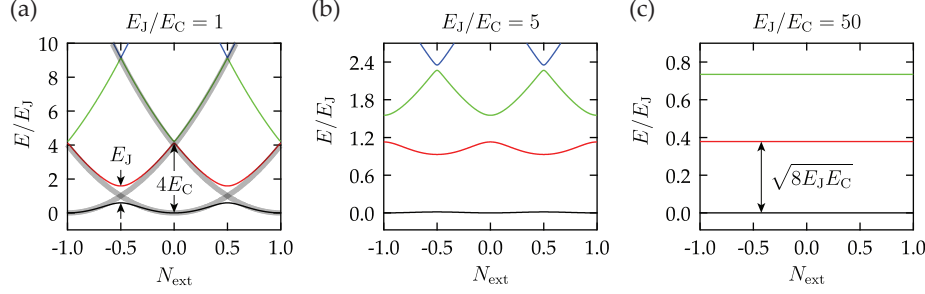
The anharmonicity at $N_{\text{ext}} = 0$ and 0.5 also collapses into a single curve because of the flattening of the energy band [Fig. 5(h)]. The crucial observation is that, although α is also approaching zero, its slope is algebraic rather than exponential. This suggests that we can use the circuit in the large E_J/E_C limit as a charge-insensitive qubit, which is called a transmon (see Sec. IV B for the implementation of a transmon).²⁰

3. Loop-Based Qubit

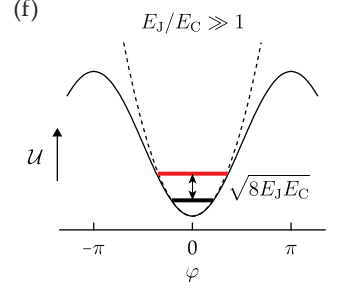
A loop-based qubit is not as simple as an island-based qubit because we have to consider all terms in Eq. (15). We start with the effect of E_L . Since E_L is a function of φ , it is convenient to take the phase basis, and consequently, to treat E_J and E_L terms as the potential. We first consider the regime in which $E_J/E_L \gg 1$. In this regime, the periodic shape is prominent in the potential as shown in Fig. 6(a)–(d). When $E_J/E_C \ll 1$ [Fig. 6(e)], the energy level diagram is almost independent of Φ , and $\omega_q \approx \sqrt{8E_L E_C}/\hbar$. The reason is that the oscillating potential is averaged out owing to the large kinetic energy [Fig. 6(a)], and consequently, only the harmonic terms are effective in Eq. (15). In this regime, \hat{N} is localized. Thus, \hat{N} corresponds to the position in the spring-block oscillator analogy, L corresponds to the mass, and C^{-1} corresponds to the spring constant.

For $E_J/E_C > 1$, the physics of a loop-based qubit can be understood in a similar way to that of an island-based qubit. In Fig. 6(f) and (g), the gray lines show the E_L term in Eq. (15) associated with $|\varphi=0\rangle$ and

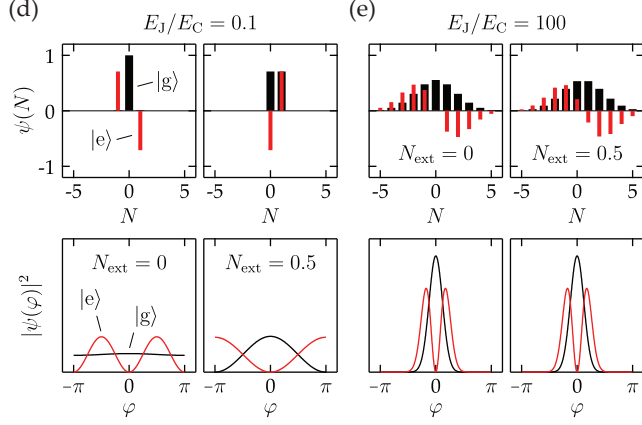
Energy levels of an island-based qubit



Weakly anharmonic potential



Wavefunctions of the ground and excited states



Engineering transition frequency and anharmonicity

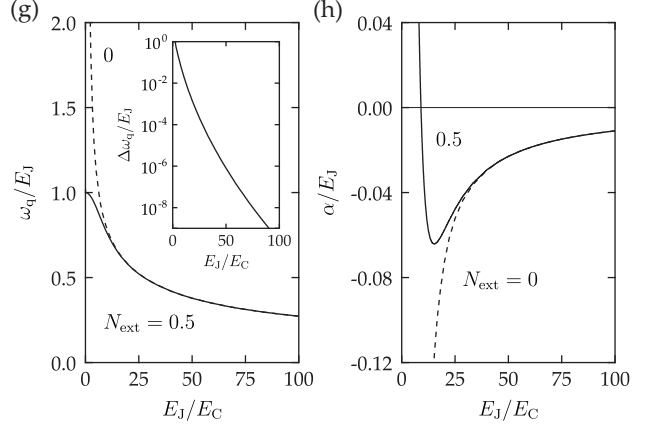


FIG. 5. (a)–(c) Energy levels of an island-based qubit with three different E_J/E_C ratios. (d) and (e) Wavefunctions of the ground state $|g\rangle$ and the excited state $|e\rangle$ in the number and phase bases. (f) If the displacement in the phase basis is reasonably small, which is the case when $E_J/E_C \gg 1$, we can approximate the cosine potential \mathcal{U} (solid line) as a weakly nonlinear harmonic potential (dashed line). (g) Transition frequency between $|g\rangle$ and $|e\rangle$, ω_q , as a function of E_J/E_C ratio at $N_{\text{ext}} = 0$ (dashed line) and 0.5 (solid line). The inset shows the E_J/E_C dependence of $\Delta\omega_q \equiv \omega_q(N_{\text{ext}}=0) - \omega_q(0.5)$. (h) Anharmonicity $\alpha \equiv \omega_{e-f} - \omega_q$, where ω_{e-f} is the transition frequency between $|e\rangle$ and the higher excitation level $|f\rangle$ as a function of E_J/E_C ratio.

$|\pm 2\pi\rangle$, which means that the numbers of trapped fluxes in the loop are 0 and ± 1 , respectively. Note that, at $\Phi/\Phi_0 = 0.5$ ($\varphi_{\text{ext}} = \pi$), the potential has a double-well shape, resulting in energy degeneracy between $|\varphi \approx +\pi\rangle$ and $|\varphi \approx -\pi\rangle$. These degenerated states correspond to two superposed currents circulating in opposite directions [Fig. 6(b) and its inset]. Similarly to the degeneracy point in an island-based qubit, the hybridization mediated by the kinetic energy (E_C term) breaks the degeneracy, resulting in an anticrossing. This process can be understood as coherent flux tunneling between the flux island (loop) and the flux reservoir [Fig. 4(b)]. On the basis of this explanation, it is easy to understand that ω_q at $\Phi/\Phi_0 = 0.5$ decreases monotonically as a function of E_J/E_C [Fig. 6(m)].

At zero flux bias, the first excitation level is formed through the hybridization of states $|\varphi \approx \pm 2\pi\rangle$, as shown in Fig. 6(c). Since this hybridization requires the tunneling of two potential barriers, the energy gap is significantly smaller than that at $\Phi/\Phi_0 = 0.5$. Hence, ω_q at zero bias is approximately $2\pi^2 E_L [= E_L(\pm 2\pi)^2/2]$ and weakly depends on E_J/E_C . This explains why ω_q at zero

bias shows a plateau in Fig. 6(m).

As E_C decreases further [Fig. 6(h)], the ground and excited states at zero bias become bound states within a well of the periodic potential. In this case, we can approximate the potential as a weakly nonlinear harmonic potential [Fig. 6(d)] as we did in Sec. III C 2. Hence, $\omega_q \approx \sqrt{8E_J E_C}/\hbar$. This explanation suggests that the physics of a loop-based qubit in this regime is actually close to that of two island-based qubits connected by an inductor, i.e., inductively shunted junction [the inset of Fig. 6(d)]. The reason is that L is very large in the regime $E_J/E_L \gg 1$ such that the reactance at ω_q is significant, whereas the circuit is electrically shorted at the low-frequency limit.

In the regime $E_J/E_L \sim 1$, the harmonic contribution to the potential is substantial; thus, it is difficult to separate the contributions from the periodic and harmonic potentials to the energy levels. One consequence is that the minimum of the potential becomes almost flat at $\Phi/\Phi_0 = 0.5$ as shown in Fig. 6(j). The other consequence is that, in Fig. 6(k) and (l), the first excitation level near zero bias already has a parabolic shape

Energy levels of a loop-based qubit

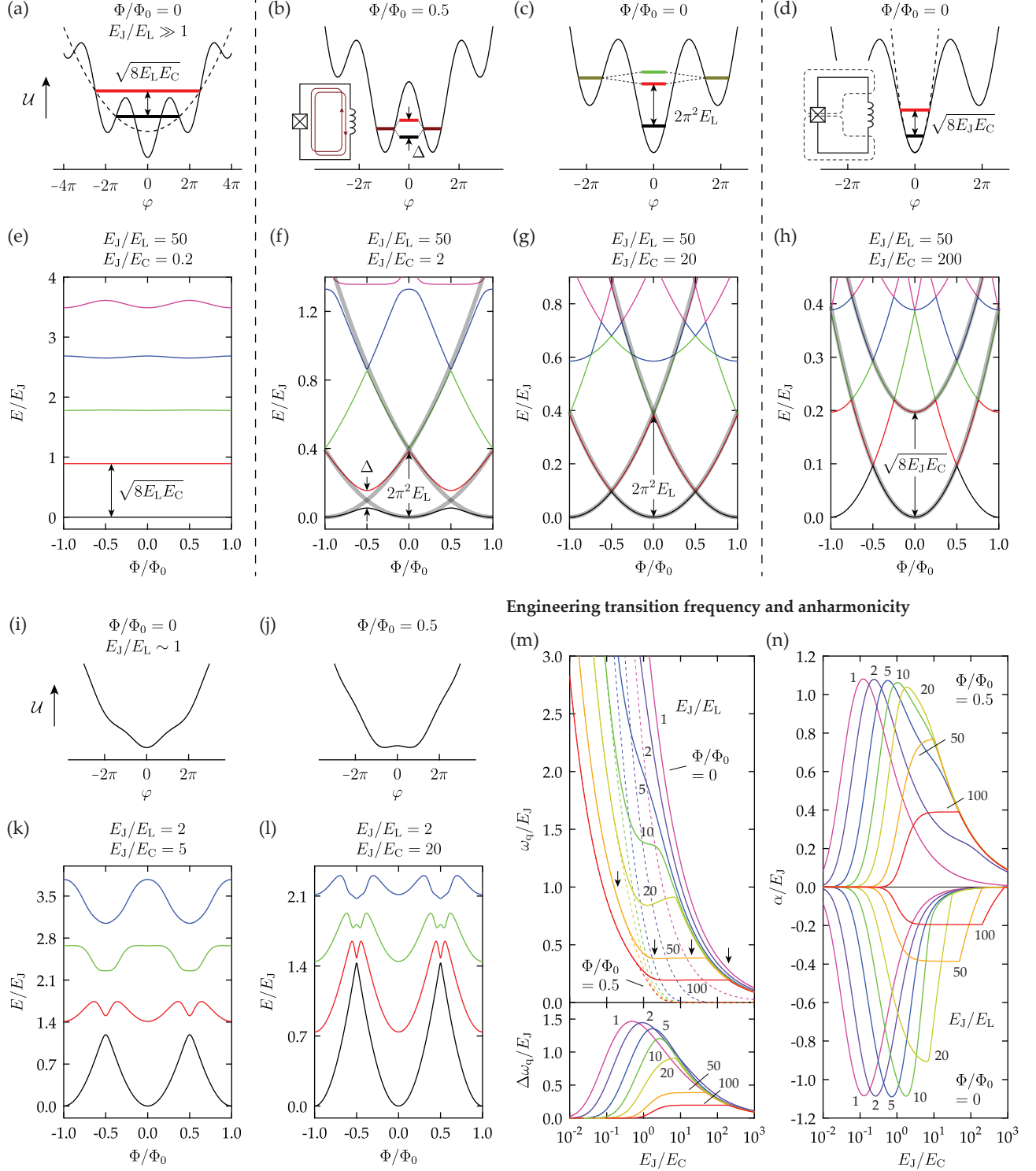


FIG. 6. (a)–(h) Potential U [(a)–(d)] and energy level diagrams [(e)–(h)] of a loop-based qubit when $E_J/E_L \gg 1$. The potential-energy level correspondence is [(a) and (e)], [(b), (c) and (f), (g)], and [(d) and (h)]. Φ is the external flux bias and Φ_0 is the flux quantum. The inset in (b) shows the circulating currents in the circuit; the inset in (d) shows a circuit describing a loop-based qubit as two charge islands (dashed lines) that are connected by an inductor. Gray lines in (f)–(h) indicate how the ground and first excited levels appear from Eq. (15). (i)–(l) Similar diagrams for the potential and the energy levels when $E_J/E_L \sim 1$. (m) Transition frequencies ω_q at $\Phi/\Phi_0 = 0$ (solid lines in the upper panel) and 0.5 (dashed lines), and their difference $\Delta\omega_q$ (lower panel) as a function of E_J/E_C . Arrows in the upper panel indicate the E_J/E_L and E_J/E_C ratios employed in (e)–(h). (n) Anharmonicity as a function of E_J/E_C . At $\Phi/\Phi_0 = 0.5$, α is positive, while it is negative at zero bias. In (m) and (n), the numbers near solid lines indicate the corresponding E_J/E_L ratios.

rather than a cross shape because the first excitation level at zero bias is mostly governed by the physics shown in Fig. 6(d), rather than the hybridization shown in Fig. 6(c). This explains why ω_q at $\Phi/\Phi_0 = 0$ in this regime decreases monotonically with increasing E_J/E_C without any plateau in Fig. 6(m).

The experimentally accessible range of E_J/E_C is typically from ~ 0.1 to ~ 100 . In this range, ω_q of a loop-based qubit with $E_J/E_L \gg 1$ at $\Phi/\Phi_0 = 0.5$ is often too low to satisfy condition 1 in Sec. III A, while ω_q of a qubit with $E_J/E_L \sim 1$ at zero bias is too high. Regarding the anharmonicity, a loop-based qubit with $E_J/E_L \gg 1$ is more advantageous than that with $E_J/E_L \sim 1$ as shown in Fig. 6(n). If E_L increases even further such that $E_J/E_L \ll 1$, the potential becomes almost harmonic, and as a result, the circuit does not show enough anharmonicity to be a qubit.

IV. EFFECT OF NOISE

A. Relaxation

1. Concept

In general, the states of a qubit cannot last forever; after some time, they relax back to the ground state because of the interaction between the qubit and the surrounding environment. This is the reason for having condition 3 in Sec. III A. We can define two experimentally measurable time scales that characterize the relaxation of a quantum state [Fig. 7(a)]: one is the longitudinal relaxation time (T_1) and the other is the transverse relaxation time (T_2). As the name implies, T_1 is the time constant for recovering the longitudinal component of the Bloch vector to its thermal equilibrium value. Thus, the physical process responsible for T_1 is thermalization of the qubit.³ T_2 is the time constant for the decay of the transverse component of the Bloch vector to zero. Note that there are two contributions to T_2 in Fig. 7(a): one is the shortening of arrows and the other is the spreading of arrows. The shortening of arrows is due to the growth of the longitudinal component, whereas the spreading is due to the loss of the phase coherence of the qubit, called dephasing. As shown in Fig. 7(b) and (c), dephasing is caused by the temporal fluctuation in qubit transition frequency. Hence, both thermalization and dephasing contribute to T_2 , while T_1 is entirely determined by thermalization. This explanation can be written as²¹

$$\frac{1}{T_1} = \Gamma_{\parallel}, \quad \frac{1}{T_2} = \frac{\Gamma_{\parallel}}{2} + \Gamma_{\varphi}, \quad (18)$$

³ A considerable number of papers use the term “depolarizing” to describe the physical process responsible for T_1 . We do not use this term to avoid confusion with the depolarizing channel, which contracts the Bloch vector *independently* of its direction.^{10,13}

where Γ_{\parallel} is the decay rate of the excited state population and Γ_{φ} is the dephasing rate. The reason for the factor of 2 in $\Gamma_{\parallel}/2$ will be given in Sec. VI A. The measurement procedures for T_1 and T_2 are described in Sec. VIII B.

The interaction with the surrounding environment is usually treated as various noise processes. The effects of noises are explained further in the following subsections.

2. Thermalization

Thermalization of a qubit occurs via incoherent energy exchange between the qubit and the environment [Fig. 7(d)]. The effect of such an interaction is usually modeled as the fluctuation in qubit Hamiltonian. In the qubit Hamiltonian, there are physical quantities that mediate the interaction between the qubit and the environment, such as external charge and flux biases. If we denote such a physical quantity as λ , the susceptibility of the qubit Hamiltonian to the fluctuation in λ , denoted by \hat{X}_{λ} , is given by the derivative of the qubit Hamiltonian $\hat{\mathcal{H}}_q$ with respect to λ . For example, the noise caused by fluctuating charges nearby, called charge noise, is coupled to the qubit through the external charge bias; hence, $\lambda = N_{\text{ext}}$. For the noise caused by fluctuating spins, called flux noise, $\lambda = \varphi_{\text{ext}}$. Similarly, the effect of the fluctuation in critical current can be estimated by $\lambda = E_J$ (or I_c). Then, for $\hat{\mathcal{H}}_q$ in Eq. (15), \hat{X}_{λ} for these quantities are given by

$$\hat{X}_N = \frac{\partial \hat{\mathcal{H}}_q}{\partial N_{\text{ext}}} = 8E_C \hat{N}, \quad (19)$$

$$\hat{X}_{\Phi} = \frac{\partial \hat{\mathcal{H}}_q}{\partial \varphi_{\text{ext}}} = -E_J \sin(\hat{\varphi} - \varphi_{\text{ext}}), \quad (20)$$

$$\hat{X}_{E_J} = \frac{\partial \hat{\mathcal{H}}_q}{\partial E_J} E_J = -E_J \cos(\hat{\varphi} - \varphi_{\text{ext}}). \quad (21)$$

Here, we insert E_J in Eq. (21) to set the dimension of \hat{X}_{E_J} identical to the other two equations for fair comparison.

To thermalize a qubit, the environment must be able to dissipate an electromagnetic energy near ω_q . Thus, the thermalization process is governed by the noise whose frequency is near ω_q . Using Fermi’s golden rule, Γ_{\parallel} can be written as²¹

$$\Gamma_{\parallel} = \frac{1}{\hbar^2} \sum_{\lambda} \left| \langle 1 | \hat{X}_{\lambda} | 0 \rangle \right|^2 |S_{\lambda}(\omega_q) - S_{\lambda}(-\omega_q)|, \quad (22)$$

where S_{λ} is the noise power spectral density associated with the fluctuation in λ . On the basis of Eq. (22), the thermalization process is often interpreted as the dipole transition associated with the effective dipole moment \hat{X}_{λ} .

In Eq. (22), $S_{\lambda}(\omega_q)$ and $S_{\lambda}(-\omega_q)$ represent emission (from $|1\rangle$ to $|0\rangle$) and absorption (from $|0\rangle$ to $|1\rangle$), respectively. When the qubit frequency is much greater than the temperature of the environment T , i.e., $\hbar\omega_q \gg k_B T$,

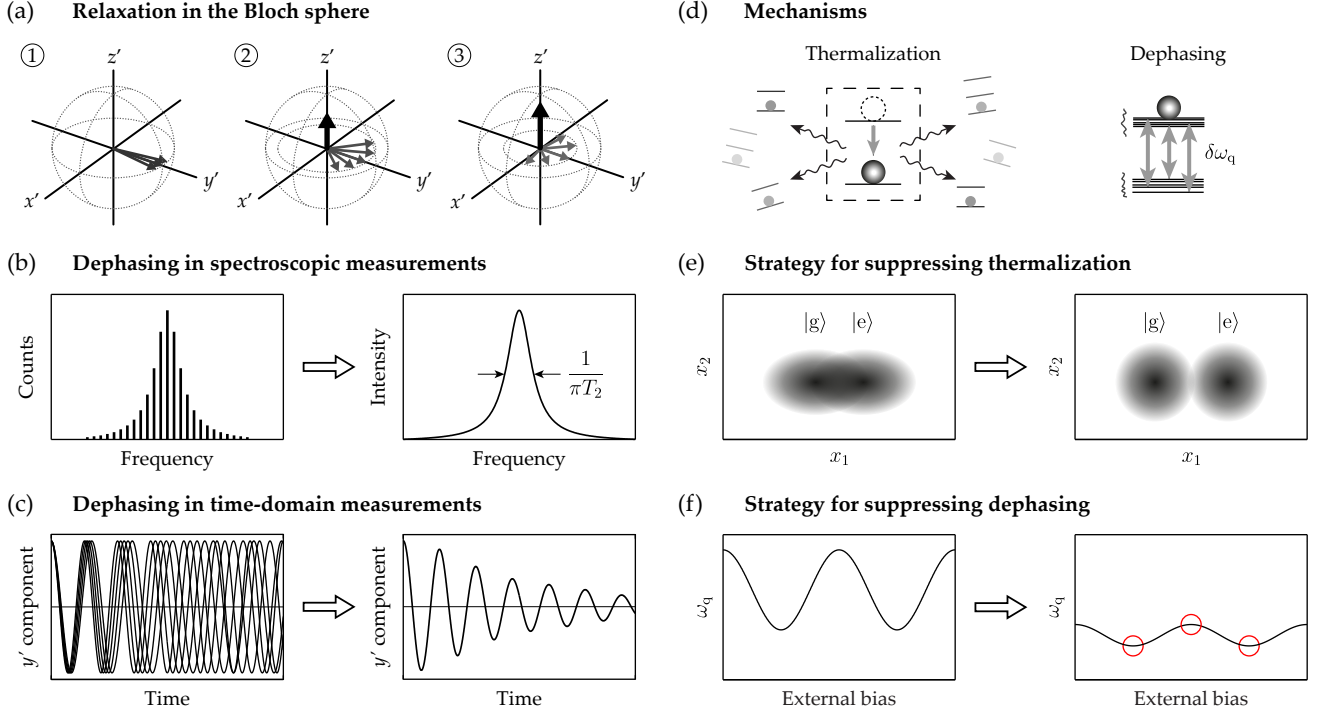


FIG. 7. (a) Relaxation of qubit states in a set of identical measurements represented in the Bloch sphere. Each arrow represents the qubit state for each measurement. Primes (') in the axes indicate the rotating frame with the average qubit transition frequency. The numbers in circles indicate the time instant during a single measurement. The thick arrow growing along the z' -axis represents the longitudinal relaxation, while spreading and shortening arrows in the $x'y'$ -plane represent the transverse relaxation. (b) In spectroscopic measurements, the qubit transition frequency varies with time because of noises from the surrounding environment. In general, a large deviation from the center is unlikely to occur as shown in the histogram (left figure). Such a fluctuation broadens the qubit spectrum (right figure). (The measurement procedure is described in Sec. VIII A 2.) This phenomenon, called dephasing, corresponds to the spreading of arrows in (a). (c) The temporal fluctuation in qubit transition frequency induces the loss of phase coherence between the signals obtained in each measurement (left figure). The averaged signal is a decaying signal with the time constant T_2 (right figure). (The measurement procedure is described in Sec. VIII B 3.) Note that the Fourier transform connects the decay in time-domain measurement and the spread in spectroscopic measurement; hence, the width of the qubit spectrum is about $1/\pi T_2$ in Hz as shown in (b). In (b) and (c), T_1 is assumed to be much longer than T_2 . (d) Relaxation mechanisms. Thermalization is due to the energy exchange between the qubit and the environment. Dephasing is due to the fluctuation in the transition frequency of the qubit, $\delta\omega_q$. (e) Thermalization can be suppressed by reducing the overlap between the ground-state and excited-state wavefunctions in the circuit variable space, such as \hat{N} and $\hat{\varphi}$ in Eq. (15). In this figure, the circuit variables are denoted by x_1 and x_2 for generality. (f) Dephasing can be suppressed by designing the qubit to be less sensitive to the external bias and operating the qubit at its sweet spot. The figure shows the schematic external bias dependence of the qubit transition frequency (ω_q). Red circles indicate sweet spots.

we can safely ignore the contribution from the absorption process. Then, we have

$$S_\lambda(\omega_q) - S_\lambda(-\omega_q) \approx A_\lambda^2 \left(\frac{2\pi \times 1 \text{ [Hz]}}{\omega_q} \right)^\mu, \quad (23)$$

where A_λ is the noise magnitude, and $\mu \approx 1$ for $1/f$ noise and $\mu \approx -1$ for Ohmic noise. It has been reported that Ohmic noise is chiefly responsible for Γ_\parallel (Refs. 22 and 23) and $1/f$ noise is responsible for Γ_φ (Refs. 24–26).

Equations (19)–(22) suggest that thermalization due to various noise processes acting on a qubit is determined by the circuit parameters and the off-diagonal matrix elements of \hat{N} and $\hat{\varphi}$, i.e., the overlap between wavefunctions in the circuit variable space.

Currently, there are three approaches to suppressing thermalization:

1. *Clean environment*: This approach eliminates the noise source by removing any unnecessary quantum systems, such as defects, which could possibly couple to the qubit. Naturally, this approach requires much knowledge and engineering regarding materials, such as host superconductors, substrates, and oxide layers.^{27–29} For example, it is known that a qubit on a silicon substrate usually shows a shorter T_1 than that on a sapphire substrate, partly because of a lossy amorphous silicon oxide layer.³⁰ For a comprehensive review for this approach, see Ref. 31.

2. *Reducing participation ratio*: This approach reduces losses in dielectric media, such as oxides or organics at the surface of a qubit, by minimizing the participation ratio that is defined as the fraction of the electric field energy stored within the volume of each dielectric medium.^{32,33} Since an electric field in a planar device is highly concentrated near the edges, a qubit made of large superconducting pads with a simple design shows good performance in general.^{30,32}
3. *Reducing wavefunction overlap*: We can engineer the potential by choosing the geometry and parameters of the circuit to minimize the effective dipole moment, i.e., the wavefunction overlap in the circuit variable space, as shown in Fig. 7(e). This is the strategy that the so-called protected qubit takes.^{34–39} However, reducing the effective dipole moment inevitably makes the qubit difficult to control [compare Eqs. (22) and (34)].

3. Dephasing

Dephasing is due to the temporal fluctuation in the transition frequency $\delta\omega_q$ [Fig. 7(d)], which can be expressed as²¹

$$\delta\omega_q \propto |\langle 1|\hat{X}_\lambda|1\rangle - \langle 0|\hat{X}_\lambda|0\rangle|. \quad (24)$$

Equation (24) suggests that the dephasing is determined by the diagonal matrix elements of \hat{N} and $\hat{\varphi}$ [Eqs. (19)–(21)]. In the Bloch sphere [Fig. 7(a)], if ω_q is the same as the frequency of the rotating frame, the transverse component will lie along the y' -axis. However, owing to the fluctuation in ω_q , the transverse component rotates around the z' -axis with amount of rotation differing from measurement to another measurement, resulting in the spreading of arrows [Fig. 7(a)]. As a result, the qubit loses the phase coherence and the averaged transverse component in the Bloch vector decays in time as shown in Fig. 7(c). To yield such a decay, the time scale of the fluctuation must be much slower than the qubit transition (thus, adiabatic) and should be a similar order of magnitude to the measurement time scale. Therefore, the dephasing rate Γ_φ is mainly determined by low-frequency noise.

To estimate Γ_φ , we have to perform an integration with respect to the frequency of the noise. For this, we set the low-frequency ω_{low} and high-frequency ω_{high} cutoffs. If our time scale of interest τ satisfies $\omega_{\text{low}}\tau \ll 1$ and $\omega_{\text{high}}\tau \gg 1$, Γ_φ is roughly given by^{20,21}

$$\Gamma_\varphi \sim A_\lambda \left| \frac{\partial\omega_q}{\partial\lambda} \right|, \quad (25)$$

where A_λ is the noise magnitude defined in Eq. (23).

On the basis of what we have learned thus far, we explain two approaches to suppressing dephasing.

1. *Geometry*: We can select a circuit geometry that is insensitive to a certain type of noise. A fixed-frequency island-based qubit is insensitive to flux noise simply because there is no loop that can contain a flux [Fig. 4(a)]. For a loop-based qubit, the sensitivity to flux noise depends on the circuit parameters. If the qubit is in a circuit parameter range in which the qubit states are the circulating current states shown in Fig. 4(b) and the inset of Fig. 6(b), the qubit is insensitive to charge noise. The reason is that a continuously flowing DC supercurrent does not allow any charge offset within the current path, i.e., the circuit is electrically shorted in the low-frequency limit. However, such a state is sensitive to flux noise. If the circuit parameters are chosen such that the qubit states are similar to the island-like qubit shown in the inset of Fig. 6(d), then the qubit states are sensitive to charge noise but less sensitive to flux noise.
2. *Bias dependence*: Since Γ_φ is proportional to $\partial_\lambda\omega_q$ [Eq. (25)], we can choose the circuit parameters that give minimal bias dependence as shown in Fig. 7(f). In this regard, operating a qubit at a bias at which $\partial_\lambda\omega_q = 0$, called a sweet spot [red circles in Fig. 7(f)], is necessary because the qubit is first-order insensitive to noise at this particular bias [$\Gamma_\varphi = 0$ in Eq. (24)].

Note that the energy of a qubit is conserved during dephasing, in contrast to thermalization. This allows us to recover the phase coherence by applying pulses that can revert the direction of the time evolution. Such a technique is called refocusing and will be discussed in Sec. IX C.

In Sec. IV B, we briefly explore several noise-resilient qubit designs and discuss how to improve the robustness of the qubit by tuning the circuit parameters.

B. Noise-Resilient Designs

1. Island-Based Qubit

The most successful noise-resilient design of an island-based qubit is a transmon. As mentioned in Sec. IV, the dephasing rate of an island-based qubit in Fig. 8(a) is insensitive to flux noise because of the absence of a loop. To suppress the effect of charge noise, the transmon design pushes strategy 2 in Sec. IV A 3 to the limit: eliminating the N_{ext} dependence by choosing $E_J/E_C = 50\text{--}100$ (Fig. 5).

This limit can be achieved by adopting a shunt capacitor [red capacitor in Fig. 8(a)]. The shunt capacitor takes the majority of the effect of the charge noise, thus minimizes this effect on the junction. The physics of this idea is the same as adding a heavy mass to reduce the sensitivity to mechanical noise.

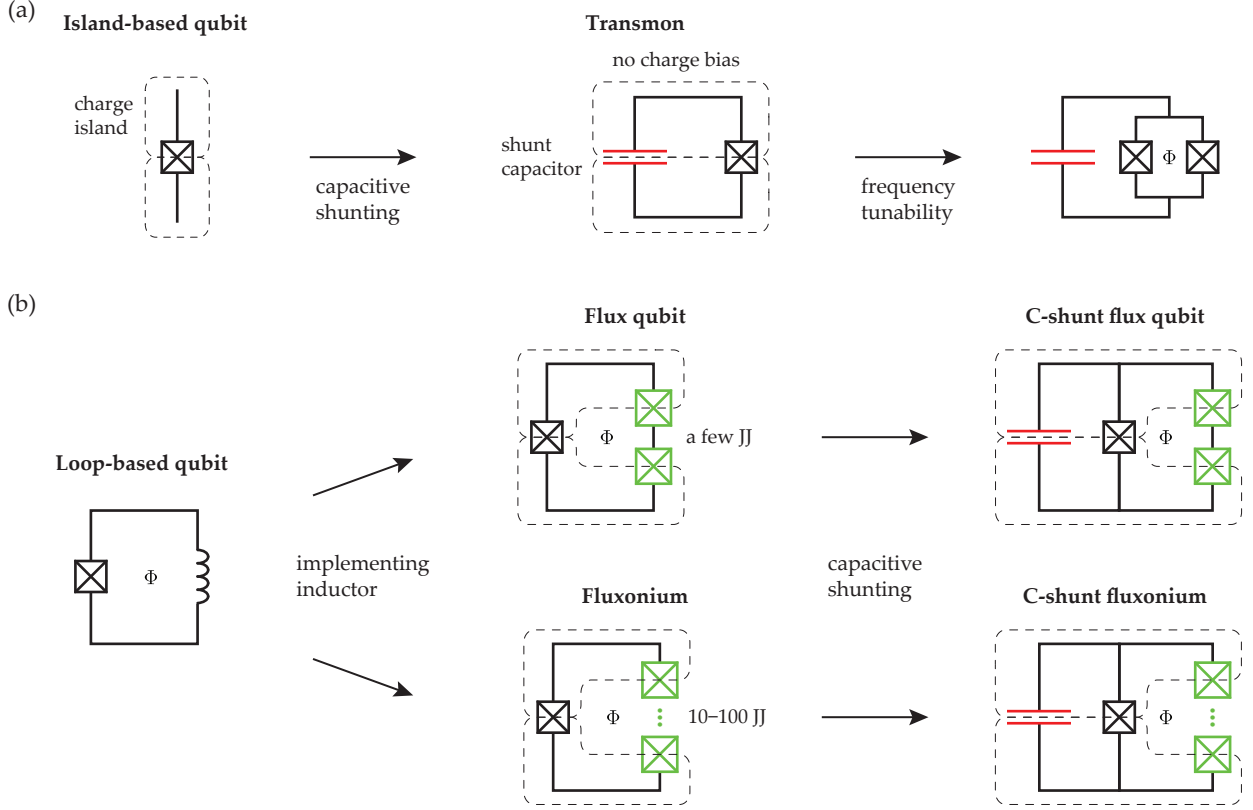


FIG. 8. Conceptual evolution of noise-resilient qubit designs from an island-based qubit (a) and a loop-based qubit (b). Dashed boundaries indicate islands. JJ stands for Josephson junction.

As mentioned in Sec. III C 2, the trade-off is the reduced anharmonicity: in the large E_J/E_C limit, the qubit wavefunctions are localized in the phase space; hence, a transmon is a weakly nonlinear harmonic oscillator. From this reasoning, we can easily imagine that, if we treat the qubit wavefunction as a rolling glass bead in a potential well, the bead sees more anharmonicity as the kinetic energy (E_C) increases. Indeed, the anharmonicity of a transmon is roughly given by $-E_C$ (see Sec. V B 1). E_C is usually chosen 100–500 MHz to satisfy condition 2 in Sec. III A. Then E_J must be 10–30 GHz to satisfy condition 1 in Sec. III A. The resulting circuit parameters are summarized in Table II.

A DC SQUID is employed to tune the qubit frequency as explained in Sec. III B [rightmost figure in Fig. 8(a)]. However, in this case, the transmon is exposed to the flux noise. Therefore, we need to design a DC SQUID with minimal flux dependence based on Eq. (14).⁴³ In addition, we have to operate the tunable transmon at the flux bias sweet spot.

2. Loop-Based Qubit

The main difficulty in implementing a loop-based qubit is designing an inductor with sufficiently large inductance

because the inductance of a superconducting loop made of aluminum or niobium is usually very small such that $E_L > E_J$. Consequently, the resulting anharmonicity is too small to satisfy condition 2 in Sec. III A as explained in Sec. III C 3.

A popular strategy is to add multiple Josephson junctions, where the Josephson energy for each junction is βE_J , as an effective inductor. Here, we still want to keep the current flowing in the loop dominated by the main junction [black junction in Fig. 8(b)].⁴ Since the flux tunneling rate through a Josephson junction is roughly proportional to $\exp(-\sqrt{E_J/E_C})$ (Ref. 44), β must be larger than 1.

The resulting potential term \hat{U} is given by

$$\hat{U} \approx -E_J \cos \hat{\varphi} - \beta E_J \sum_{i=1}^{N_J} \cos \hat{\varphi}_i, \quad (26)$$

where N_J is the number of additional Josephson junctions and $\hat{\varphi}_i$ is the phase difference across additional junction i . Note that the loop inductance does not appear

⁴ In the literature, the main junction is often called the “ α junction”, where $\alpha = \beta^{-1}$, for historical reasons.

in Eq. (26). The reason is that the phase variable associated with the loop inductance is nearly zero because of the large E_L ; thus, its contribution to the qubit dynamics is small compared with that from the additional junctions. On the other hand, in the phase dimensions associated with the additional junctions, the potential has periodic modulations that can support coherent flux tunneling.^{45,46}

First, we consider the case when N_J is 2 or 3 and $\beta \approx 2$ [upper figures in Fig. 8(b)]. The circuit with these parameters, which roughly corresponds to a loop-based qubit with $E_J/E_L \sim 1$, is called a flux qubit. Although the resulting energy level structure from Eq. (26) is not the same as that from Eq. (15), the overall dependence of the energy levels on the circuit parameters is qualitatively similar to that in Fig. 6(k)–(n).

For a noise-resilient qubit, we need to select E_J to minimize the φ_{ext} dependence as mentioned in Sec. IV. At the same time, we also need to satisfy condition 1 in Sec. III A. It was found that $E_J \sim 10\text{--}100$ GHz and $\beta \approx 2$ balance these two.²³ However, there is a trade-off: the qubit becomes sensitive to charge noise because the circulating currents are close to zero even at $\Phi/\Phi_0 = 0.5$. To circumvent this, a shunt capacitance is added to the main junction as we did for the transmon; thus, we have $E_C = 0.1\text{--}1$ GHz. The final circuit shown in Fig. 8(b) is called a capacitively shunted (C-shunt) flux qubit [upper rightmost figure in Fig. 8(b)].⁴⁷

One might ask, “can a flux-tunable transmon be considered as a kind of C-shunt flux qubit?” Our answer is yes, but the working flux bias at which criterion 1 in Sec. III A is satisfied is different: a transmon is usually operated at zero flux bias, while a C-shunt flux qubit is operated at $\Phi/\Phi_0 = 0.5$.

With a sufficiently large N_J ($\sim 10\text{--}100$), Eq. (26) can be treated as a linear inductor with $E_L \approx \beta E_J/N_J$ [lower figures in Fig. 8(b)], if the self-resonance frequency of the junction array is sufficiently higher than that of each junction, $\sqrt{8E_J E_C}/h$ (Ref. 48). This condition can be satisfied by limiting N_J to $N_J \lesssim \sqrt{C_J/C_g}$, where C_J is the capacitance across each junction and C_g is the capacitance between the junction array and the ground. By tuning β and N_J , we can satisfy $E_L \ll E_J$. A superconducting qubit in this regime is called a fluxonium or an RF SQUID qubit. In this case, it is easy for ω_q at zero bias to satisfy condition 1 in Sec. III A; at $\Phi/\Phi_0 = 0.5$, ω_q might be too low. This drawback can be resolved by employing active qubit initialization protocols (see Sec. VI E). According to Fig. 6(h), the anisotropy is significantly larger than that of a flux qubit. Capacitive shunting has also been applied to a fluxonium [lower rightmost figure in Fig. 8(b)], resulting in improved T_2 (Ref. 42).

Lastly, we would like to point out that a Josephson junction array as a linear inductor itself is an interesting system. The reason is that it is difficult, although not impossible,⁴⁹ to make a geometric inductor whose reactance exceeds the superconducting resistance quantum $R_Q = h/(2e)^2 \approx 6.5$ k Ω because of stray capacitance

TABLE II. Circuit parameters of several noise-resilient qubit designs. For the flux qubit and fluxonium, which have multiple junctions, E_J is for the smallest junction [the black junctions in Fig. 8(b)]. In addition, the flux qubit and fluxonium considered in this table are capacitively shunted ones.

Type	E_J [GHz]	E_J/E_C	E_J/E_L	β	N_J	Ref.
Transmon	10–30	50–100				40,41
Flux qubit	10–100	10–100	~ 1	≈ 2	2–3	23
Fluxonium	1–10	1–10	3–10	2–5	10–100	42

and radiation to vacuum, whose impedance is about 377 Ω . Such a linear inductor whose impedance is similar to or larger than R_Q is often called a superinductor. Thus, implementations of superinductors have usually been based on kinetic inductance,^{48,50,51} i.e., an inductive contribution to the impedance that arises from kinetic energy of the charge carrier, instead of geometric inductance. (For further discussion about kinetic inductance, see Sec. VI B 2.) Very recently, a qubit made of Josephson junction arrays with extremely high inductance ($E_L < 100$ MHz) succeeded in implementing the regime shown in Fig. 6(a) and (e).⁵²

V. COUPLING

Thus far, we have explained how to make a qubit out of superconductors. To perform actual computation, a qubit must be coupled to other systems so that the qubit state can be controlled or read. The most commonly used physics for these operations is the cavity quantum electrodynamics.⁵³ It provides an integrated control/readout scheme via the interaction between an atom and a cavity. The same physics can be applied to a superconducting circuit as the interaction between a qubit and a resonator. This circuit version of the cavity quantum electrodynamics is called the circuit Quantum ElectroDynamics (cQED).^{6,54,55} In addition, for multi-qubit gate operation, qubit-qubit coupling is required. In this section, we discuss how to couple a qubit to other systems.

A. Two Coupled Classical Oscillators

Before exploring a quantum system, considering a similar classical system is often helpful to understand the physics in the quantum regime. As we will see soon, the physics behind various couplings associated with qubits can be captured using two simple classical harmonic oscillators. Figure 9 shows a schematic diagram of our model system: it is composed of two classical simple harmonic oscillators, each made of a spring and a block. The two oscillators interact via the coupling spring, whose spring constant can be either static [Fig. 9(a) and (c)] or time-

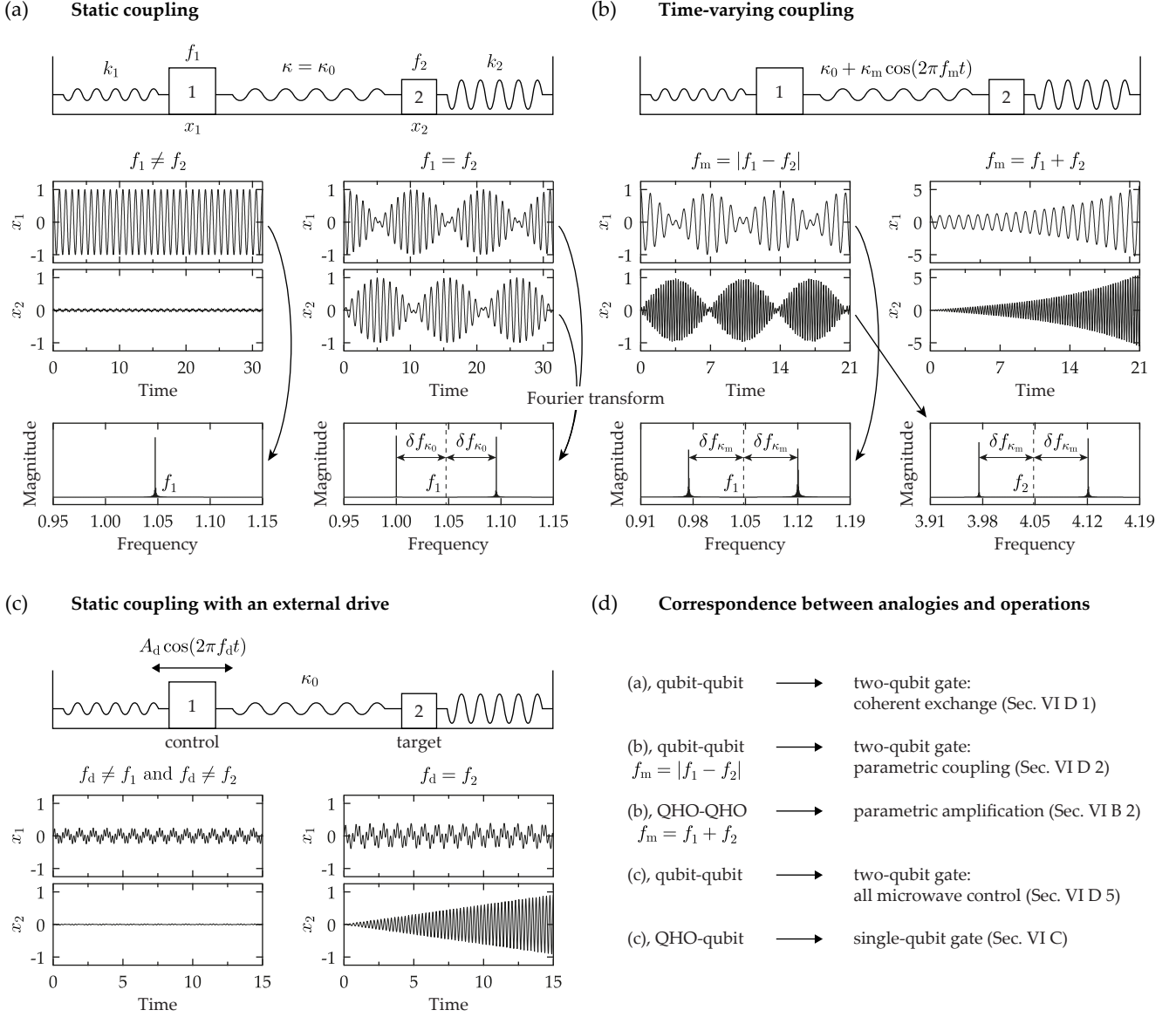


FIG. 9. Two coupled classical harmonic oscillators without damping. Each oscillator is composed of a spring and a block. k_i is the spring constant of oscillator i ; f_i is the resonance frequency; and x_i is the position. Two oscillators are coupled via a coupling spring whose spring constant is κ . The graphs show the solutions of Eq. (27) for various conditions. (a) Evolution of the system when the coupling is static: $\kappa = \kappa_0$. The two oscillators do not interact with each other if $f_1 \neq f_2$; however, if $f_1 = f_2$, the oscillators exchange their energy at a rate of $2\delta f_{\kappa_0}$, whose quantity is determined by κ_0 . As shown by the Fourier-transformed solution, the energy exchange can be interpreted as a splitting of the resonance frequency with $2\delta f_{\kappa_0}$. (b) Evolution of the system with a time-varying coupling constant $\kappa_0 + \kappa_m \cos(2\pi f_m t)$, where f_m is the modulation frequency. When $f_m = |f_1 - f_2|$, the two oscillators exchange their energy even if $f_1 \neq f_2$. The Fourier transform shows that the resonance frequency of each oscillator is split by $2\delta f_{\kappa_m}$ whose quantity is determined by κ_m . (c) Evolution of the system with the static coupling and an external drive acting on oscillator 1. Here, oscillator 1 is the control oscillator and oscillator 2 is the target oscillator. The amplitude and frequency of the drive are denoted by A_d and f_d , respectively. The parameter sets are given as follows: $\{m_1 = 10/(2\pi)^2, m_2 = 2.5/(2\pi)^2, k_1 = 10, k_2 = 40, \kappa_0 = 1\}$, if not specified. In (a), $k_2 = 10$ for $f_1 = f_2$. In (b), $\{\kappa_m = 3, f_m = |f_1 - f_2|\}$ and $\{\kappa_m = 0.75, f_m = f_1 + f_2\}$. In (c), $A_d = 30$, and $f_d = f_2 + 1$ or f_2 . The initial conditions are as follows: for (a) and (b), $\{x_1(t=0) = 1, \dot{x}_1(0) = 0, x_2(0) = 0, \dot{x}_2(0) = 0\}$; and for (c), $\{0, 0, 0, 0\}$. All numbers are unitless. (d) Correspondence between classical analogies in this figure and required operations for quantum computation covered in this tutorial. The left column indicates the analogies in this figure and actual quantum oscillators; the right column indicates the target operation. For example, the last row means that “we can understand the physics of the single-qubit gate operation by replacing oscillators 1 and 2 in (c) with a Quantum Harmonic Oscillator (QHO) and a qubit, respectively.”

varying [Fig. 9(b)]. In addition, oscillator 1 may be driven by an external force [Fig. 9(c)]. The equations of motion of this system are given by

$$\begin{aligned} m_1 \ddot{x}_1 &= -(k_1 + \kappa)x_1 + \kappa x_2 + A_d \cos(2\pi f_d t), \\ m_2 \ddot{x}_2 &= -(k_2 + \kappa)x_2 + \kappa x_1, \end{aligned} \quad (27)$$

where m_i is the mass of oscillator i , where $i = 1, 2$; k_i is the spring constant of oscillator i ; x_i is the position of the center of block i ; and κ is the spring constant of the coupling spring, which can be decomposed into two parts, namely, the static κ_0 and the time-varying $\kappa_m \cos(2\pi f_m t)$.

Note that, although the coupling spring is always present, its effect on the dynamics strongly depends on the system parameters. When κ is the static parameter κ_0 , the two oscillators exchange their energy only when they are on-resonance [Fig. 9(a)]. Even if the oscillators are off-resonance, we can force them to exchange their energy by modulating κ with the frequency difference between the two oscillators, $|f_1 - f_2|$, where $2\pi f_i = \sqrt{(k_i + \kappa_0)/m_i}$ [Fig. 9(b)]. These two phenomena can be seen in both classical and quantum systems regardless of whether statistics is fermionic (qubit) or bosonic (resonator).

Next, we inject energy into the system by two methods. One is to modulate the coupling constant with $f_m = f_1 + f_2$. In this case, as one can see in Fig. 9(b), both x_1 and x_2 increase exponentially with time. This is parametric amplification, which is important for realizing noiseless amplification. The concept and applications of parametric amplification will be discussed further in Sec. VIB 2. The other is to drive oscillator 1 with the frequency f_d . When $f_d = f_2$, x_2 increases linearly with time.

When we apply the physics learned from these energy injection processes, we need to consider the quantum statistics. If two coupled quantum systems are bosonic, we can simply interpret the displacement of the blocks as the population. However, if one or both of the systems are fermionic, we will see an oscillation in the population, instead of the linear increase that we saw in Fig. 9(c). Such an oscillation is called the Rabi oscillation, which will be discussed further in Sec. VIC.

B. From Circuit to Atom

1. Qubit, Resonator, and Somewhere between Them

Now that we are well equipped with the necessary physics, it is time to move back to quantum. In cQED, the circuit Hamiltonians for a qubit and a resonator are mapped to spin-1/2 fermionic and bosonic Hamiltonians, respectively:

$$\hat{\mathcal{H}}_q \rightarrow \hbar\omega_q \frac{\hat{\sigma}_z}{2}, \quad \hat{\mathcal{H}}_r \rightarrow \hbar\omega_r \hat{a}^\dagger \hat{a}, \quad (28)$$

where $\hat{\sigma}_z$ is the Pauli z operator and \hat{a}^\dagger (\hat{a}) is the bosonic creation (annihilation) operator.

Note that this mapping assumes an ideal two-level system and a single-mode resonator. As we will see in Secs. VID and VIE 1, however, higher excitation levels of a qubit have to be considered in many situations, especially for a transmon whose anharmonicity is weak. On the other hand, the resonator may show a small nonlinearity that has to be considered for high fidelity control. Hence, we sketch how to model a transmon in the second quantization formalism as an example of a weakly anharmonic/nonlinear system. By expanding Eq. (16), we have

$$\hat{\mathcal{H}}_q \approx 4E_C \hat{N}^2 + \frac{1}{2} E_J \hat{\varphi}^2 - \frac{1}{24} E_J \hat{\varphi}^4. \quad (29)$$

In Eq. (29), the first two terms, i.e., harmonic terms, can be diagonalized by defining

$$\hat{N} = -iN_0(\hat{b} - \hat{b}^\dagger), \quad \hat{\varphi} = \varphi_0(\hat{b} + \hat{b}^\dagger), \quad (30)$$

where $N_0^2 = \sqrt{E_J/32E_C}$ and $\varphi_0^2 = \sqrt{2E_C/E_J}$ are the zero-point fluctuations, and \hat{b}^\dagger (\hat{b}) is the bosonic creation (annihilation) operator for a transmon. Note that the zero-point fluctuations are determined by the E_J/E_C ratio. After normal ordering, we obtain

$$\hat{\mathcal{H}}_q \approx \left(\sqrt{8E_J E_C} - E_C \right) \hat{b}^\dagger \hat{b} - \frac{E_C}{2} \hat{b}^\dagger \hat{b}^\dagger \hat{b} \hat{b}. \quad (31)$$

Here, the terms whose mean excitation number is nonzero, such as $\hat{b}\hat{b}$ and $\hat{b}^\dagger\hat{b}^\dagger$, are ignored because the dynamics induced by these terms will be averaged out at the time scale we are interested in. (This is the rotating wave approximation, which will be introduced formally in Sec. VB 2). Thus, a transmon can be mapped into a harmonic oscillator with the Kerr-type nonlinearity:

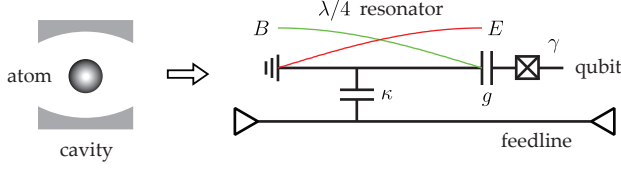
$$\hat{\mathcal{H}}_q \rightarrow \hbar\omega_q \hat{b}^\dagger \hat{b} + \frac{\hbar K}{2} \hat{b}^\dagger \hat{b}^\dagger \hat{b} \hat{b}, \quad (32)$$

where K is the Kerr coefficient. Equations (31) and (32) suggests that ω_q is about $\sqrt{8E_J E_C}/\hbar$ ($\because E_J/E_C \gg 1$) and the anharmonicity, i.e., $\hbar K$, is $-E_C$. These results are consistent with Secs. IIIC 2 and IV B 1.

Although Eq. (32) models several important properties of a weakly anharmonic/nonlinear system successfully, we still need a unified description of superconducting circuits in a wide range of nonlinearity for complicated circuits. Moreover, off-resonant resonator modes have been known to contribute substantially to the relaxation times of a qubit via the Purcell effect (see Sec. VIB 1).⁵⁶ To remedy these issues, semiclassical superconducting circuit quantization methods have been proposed and showed a good agreement with experimental data. Interested readers should see Refs. 33, 57–60.

For the rest of this section, we model a superconducting qubit as an ideal two-level system because this pro-

(a) Circuit implementation of atom-cavity coupling



(b) Types of qubit-resonator coupling

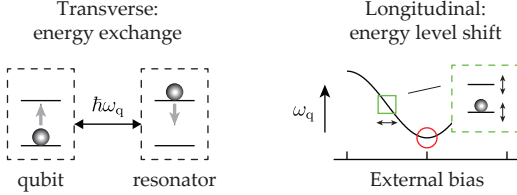


FIG. 10. (a) In a superconducting circuit, the atom-cavity interaction can be implemented by the qubit-resonator coupling. Here, the resonator can be either a planar resonator or a 3D cavity; in either case, it is usually modeled as an LC circuit. The circuit shows the capacitive coupling between a quarter-wavelength ($\lambda/4$) resonator and an island-based qubit. Here, g represents the strength of the transverse coupling between the resonator and the qubit; κ represents the loss rate of photons from the resonator; and γ represents the transverse relaxation rate of the qubit. (b) Mechanisms for the transverse and longitudinal coupling between a qubit and a resonator. For the longitudinal coupling, the change in bias shifts the qubit transition frequency ω_q at the bias shown by the green square, resulting in a strong longitudinal coupling; at the bias shown by the red circle, the longitudinal coupling is zero.

vides a qualitatively satisfactory picture to understand the physics of various couplings associated with a qubit at the level of this tutorial.

2. Qubit-Resonator Coupling

Consider a single qubit capacitively coupled to a single-mode resonator without an external drive;⁵ one example is shown in Fig. 10(a). In this case, the physical process of the coupling is the zero-point voltage fluctuation of the resonator acting on the net charge $2e\hat{N}$ ($2e$ is the charge of a Cooper pair) via the coupling capacitor between the qubit and the resonator [the capacitor labeled g in Fig. 10(a)]. Then, $2e\hat{N}$ can be considered as the effective dipole moment of this artificial atom [see Eq. (19)]. The qubit-resonator coupling Hamiltonian $\hat{\mathcal{H}}_{qr}$ can be

written as

$$\hat{\mathcal{H}}_{qr} = 2e\hat{N}\beta V_{r,0}(\hat{a} + \hat{a}^\dagger). \quad (33)$$

Here, $V_{r,0}(=\sqrt{\hbar\omega_r/2C_r})$, where C_r is the capacitance of the resonator) is the root-mean-square voltage of the zero-point fluctuation in the resonator; β is the ratio between the coupling and stored energies, which is the same as the ratio of the coupling capacitance to the total capacitance of the qubit; and $(\hat{a} + \hat{a}^\dagger)$ represents the process of populating/depopping the resonator. Defining the coupling constant

$$\hbar g_{ij} = 2e\beta V_{r,0} \langle i|\hat{N}|j\rangle, \quad (34)$$

where $|i\rangle$ and $|j\rangle$ ($i, j = 0, 1$) are the eigenstates of the bare qubit, yields

$$\begin{aligned} \hat{\mathcal{H}}_{qr} &= \hbar \sum_{i,j} g_{ij} |i\rangle\langle j| (\hat{a} + \hat{a}^\dagger) \\ &= \hbar(g_x \hat{\sigma}_x + g_z \hat{\sigma}_z)(\hat{a} + \hat{a}^\dagger), \end{aligned} \quad (35)$$

where g_x and g_z are defined by

$$g_x \equiv g_{01}(=g_{10}), \quad g_z \equiv \frac{g_{00} - g_{11}}{2}. \quad (36)$$

The g_x term is called the transverse coupling because the axis for the Pauli operator is perpendicular to the qubit quantization axis; the g_z term is called the longitudinal coupling. Here, a term associated with y is omitted because the choice of x or y is just a matter of convention.

The transverse coupling mediates the energy exchange between the qubit and the resonator [Fig. 10(b)]. Thus, the transverse coupling is effective when the coupled system has a mode whose frequency is close to ω_q as we saw in Fig. 9(a). The longitudinal coupling changes the qubit frequency. It is effective when ω_q varies considerably with the external bias [Fig. 10(b)]. Note that the physics of the relaxation processes in Sec. IV can be understood within this framework; the transverse and longitudinal couplings are actually the mechanisms for thermalization and dephasing, respectively.

Equations (34) and (36) suggest that, if ω_q does not depend on the physical parameter that is coupled to the effective dipole moment, the voltage in this case, there is no longitudinal coupling. Note that, because of this, the dominant coupling associated with a qubit at its sweet spot is the transverse coupling. One consequence is that the only possible coupling associated with a capacitively coupled transmon is the transverse coupling because ω_q of a transmon is insensitive to the external voltage fluctuation, i.e., a transmon is always at its charge bias sweet spot. To implement the longitudinal coupling, a transmon needs a flux-tunable element, such as a DC SQUID, and should be coupled to the target system inductively.⁶¹

Although Eq. (35) captures all the physics regarding the capacitive coupling, solving Eq. (35) with Eq. (28) is easy. We ignore the g_z term because the g_x term is the

⁵ Usually capacitive coupling is easier to design because, for inductive coupling, we need to consider not only geometric inductance but also kinetic inductance, which is harder to simulate or estimate than the capacitance.

dominant term at the sweet spot as mentioned above. Then, we have

$$\begin{aligned}\hat{\mathcal{H}}_{1q} &= \hat{\mathcal{H}}_q + \hat{\mathcal{H}}_r + \hat{\mathcal{H}}_{qr} \\ &= \hbar\omega_q \frac{\hat{\sigma}_z}{2} + \hbar\omega_r \hat{a}^\dagger \hat{a} + \hbar g \hat{\sigma}_x (\hat{a} + \hat{a}^\dagger).\end{aligned}\quad (37)$$

Here, we omit the subscript x in g for simplicity.

Now, we move to the rotating frame to focus on the dynamics induced by the coupling term. The Hamiltonian defining this frame is

$$\hat{\mathcal{H}}_0 = \hbar\omega_q \frac{\hat{\sigma}_z}{2} + \hbar\omega_r \hat{a}^\dagger \hat{a}. \quad (38)$$

The final single-qubit Hamiltonian in the rotating frame $\hat{\mathcal{H}}_{1q}^{\text{rot}}$ can be obtained by the unitary transformation:

$$\begin{aligned}\hat{\mathcal{H}}_{1q}^{\text{rot}} &= e^{i\hat{\mathcal{H}}_0 t/\hbar} (\hat{\mathcal{H}}_{1q} - \hat{\mathcal{H}}_0) e^{-i\hat{\mathcal{H}}_0 t/\hbar} \\ &= \hbar g [\hat{\sigma}_x \cos(\omega_q t) - i\hat{\sigma}_y \sin(\omega_q t)] (\hat{a} e^{-i\omega_r t} + \hat{a}^\dagger e^{i\omega_r t}) \\ &= \hbar g [\hat{\sigma}_+ \hat{a} e^{i(\omega_q - \omega_r)t} + \hat{\sigma}_- \hat{a}^\dagger e^{-i(\omega_q - \omega_r)t} \\ &\quad + \hat{\sigma}_+ \hat{a}^\dagger e^{i(\omega_q + \omega_r)t} + \hat{\sigma}_- \hat{a} e^{-i(\omega_q + \omega_r)t}],\end{aligned}\quad (39)$$

where $\hat{\sigma}_\pm = (\hat{\sigma}_x \pm i\hat{\sigma}_y)/2$. In the above equation, if g is a constant, all terms will be averaged out at the time scale we are interested in unless ω_q and ω_r are reasonably close. In this context, the transverse coupling is told to be effective only if $\omega_q \approx \omega_r$. Moreover, we can safely ignore fast-oscillating terms, $\hat{\sigma}_+ \hat{a}^\dagger$ and $\hat{\sigma}_- \hat{a}$, in most situations. Such an approximation is called the rotating wave approximation (RWA).

After applying the RWA, $\hat{\mathcal{H}}_{qr}$ becomes (now we move back to the inertial frame)

$$\hat{\mathcal{H}}_{qr} \approx \hbar g (\hat{\sigma}_+ \hat{a} + \hat{\sigma}_- \hat{a}^\dagger). \quad (40)$$

The physical meaning of g is the exchange of energy between a quantized electromagnetic field and a qubit at a rate of $g/2\pi$. Such an energy exchange with a well-defined period and phase is called coherent exchange; this will be useful for two-qubit gate operation (Sec. VI D). Equation (40), together with Eq. (28), is called the Jaynes-Cummings Hamiltonian $\hat{\mathcal{H}}_{JC}$ (Refs. 53 and 62):

$$\hat{\mathcal{H}}_{JC} = \hbar\omega_q \frac{\hat{\sigma}_z}{2} + \hbar\omega_r \hat{a}^\dagger \hat{a} + \hbar g (\hat{\sigma}_+ \hat{a} + \hat{\sigma}_- \hat{a}^\dagger). \quad (41)$$

Equation (41) will be the central equation in Sec. VI B 1.

3. Qubit-Qubit Coupling

The physics of qubit-qubit coupling is similar to that of qubit-resonator coupling. The Hamiltonian describing

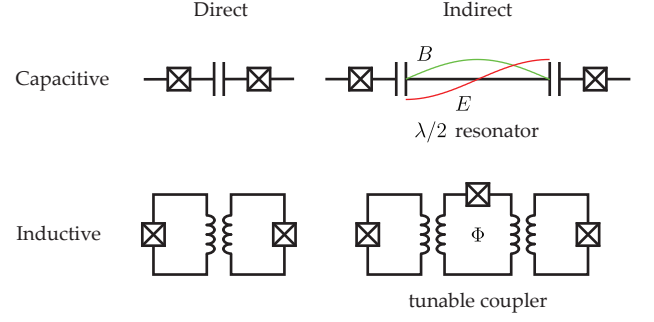


FIG. 11. Implementations of qubit-qubit coupling. Two qubits can be coupled either directly or indirectly via a coupling resonator. Here, a half-wavelength ($\lambda/2$) resonator and a tunable coupler are shown as examples. Solid lines labeled B and E represent magnetic and electric field profiles in the resonators, respectively. For fixed-frequency island-based qubits, the capacitive coupling is the only available coupling scheme. However, for loop-based qubits, not only inductive coupling but also capacitive coupling is possible because a loop-based qubit can also be understood as two superconducting islands as shown in the inset of Fig. 6(d). Note that the circuit for the tunable coupler is the same as that of the neighboring qubits. The qubit-qubit coupling constant is tuned by the external flux bias Φ .

the qubit-qubit coupling can be written as

$$\begin{aligned}\hat{\mathcal{H}}_{qq} &= \hbar (J_{xx} \hat{\sigma}_x^{(1)} \hat{\sigma}_x^{(2)} + J_{zx} \hat{\sigma}_z^{(1)} \hat{\sigma}_x^{(2)} \\ &\quad + J_{xz} \hat{\sigma}_x^{(1)} \hat{\sigma}_z^{(2)} + J_{zz} \hat{\sigma}_z^{(1)} \hat{\sigma}_z^{(2)}),\end{aligned}\quad (42)$$

where $\sigma_i^{(j)}$ ($i = x, z$) represents the Pauli operators for qubit j and J_{kl} is the qubit-qubit coupling constant. Note that we have four terms in the qubit-qubit coupling because both systems are fermions (see the last paragraph of Sec. V B 1). For better visibility, we call each term with its subscripts, for example, the J_{zz} term as the ZZ term or the ZZ interaction.

In Eq. (42), the XX interaction corresponds to the transverse interaction. Regarding the longitudinal interaction, there is ambiguity in its definition. If we follow the convention in the qubit-resonator interaction consistently, only the XZ and ZX interactions must be called the longitudinal interactions. However, a considerable number of papers designate all non-transverse interactions, which includes the ZZ interaction, as the longitudinal interactions. In this tutorial, we use the term “longitudinal interaction” for the qubit-resonator interaction only. For the qubit-qubit interaction, we call the type of interaction explicitly, such as the XZ interaction, for clarity.

We consider transmons coupled directly and capacitively (Fig. 11). In this case, the transverse (XX) interaction is the dominant interaction as discussed in Sec. V B 2. Hence, we consider the XX term only and omit the subscript xx for simplicity. Similarly to the capacitive qubit-resonator coupling, J is determined by the

coupling capacitance C_{12} and the voltage fluctuations of the ground states,

$$\hbar J = C_{12} V_{q,0}^{(1)} V_{q,0}^{(2)} \approx \frac{\hbar}{2} \frac{C_{12}}{\sqrt{C_{q1} C_{q2}}} \sqrt{\omega_{q1} \omega_{q2}}, \quad (43)$$

where $V_{q,0}^{(i)}$ ($i = 1, 2$) is the root-mean-square voltage of the ground state of qubit i ; ω_{qi} and C_{qi} are the transition frequency and total capacitance of qubit i , respectively. Since a transmon is a weakly nonlinear harmonic oscillator (Sec. IV B 1), $V_{q,0}^{(i)} \approx \sqrt{\hbar \omega_{qi} / 2 C_{qi}}$ if $C_{12} \ll C_{qi}$. Note that J depends on the transition frequency. Hence, for a coupling associated with a frequency-tunable qubit, J is also tunable.

The resulting two-qubit Hamiltonian is

$$\hat{\mathcal{H}}_{2q} = \hbar \omega_{q1} \frac{\hat{\sigma}_z^{(1)}}{2} + \hbar \omega_{q2} \frac{\hat{\sigma}_z^{(2)}}{2} + \hbar J \hat{\sigma}_x^{(1)} \hat{\sigma}_x^{(2)}. \quad (44)$$

We move to the rotating frame defined by

$$\hat{\mathcal{H}}_0 = \hbar \omega_{q1} \frac{\hat{\sigma}_z^{(1)}}{2} + \hbar \omega_{q2} \frac{\hat{\sigma}_z^{(2)}}{2}. \quad (45)$$

Then, we have an equation similar to Eq. (39):

$$\begin{aligned} \hat{\mathcal{H}}_{2q}^{\text{rot}} &= e^{i\hat{\mathcal{H}}_0 t / \hbar} (\hat{\mathcal{H}}_{2q} - \hat{\mathcal{H}}_0) e^{-i\hat{\mathcal{H}}_0 t / \hbar} \\ &= \hbar J [\hat{\sigma}_+^{(1)} \hat{\sigma}_-^{(2)} e^{i(\omega_{q1} - \omega_{q2})t} + \hat{\sigma}_-^{(1)} \hat{\sigma}_+^{(2)} e^{-i(\omega_{q1} - \omega_{q2})t} \\ &\quad + \hat{\sigma}_+^{(1)} \hat{\sigma}_+^{(2)} e^{i(\omega_{q1} + \omega_{q2})t} + \hat{\sigma}_-^{(1)} \hat{\sigma}_-^{(2)} e^{-i(\omega_{q1} + \omega_{q2})t}]. \end{aligned} \quad (46)$$

If J is static and $|\omega_{q1} - \omega_{q2}| \gg J$, it is clear that the coupling term will be averaged out, and consequently cannot be used for two-qubit gate operation unless one of the following actions is taken: (i) tuning ω_{q1} or ω_{q2} so that $\omega_{q1} \approx \omega_{q2}$; (ii) modulating J with the frequency $|\omega_{q1} \pm \omega_{q2}|$ to cancel out oscillating factors; or (iii) adding an additional drive term. These strategies are based on the lessons learned in Sec. V A and will be the basis of two-qubit gates in Sec. V D.

It is often necessary to couple two qubits separated by a macroscopic distance. In this case, a resonator or even a qubit is employed as a coupler—such a scheme is called indirect coupling (Fig. 11). Here, we need to be careful not to excite the coupler itself; otherwise, the information will leak to the Hilbert space of the coupler. Hence, the resonance frequency of the coupler must be significantly far from the transition frequency of the qubits such that $|\omega_r - \omega_{qi}| \gg g^{(i)}$, where $g^{(i)}$ is the transverse coupling constant associated with the resonator and qubit i . The coupler mediates the exchange of virtual photons between the two qubits. Such a system can also be modeled as Eq. (44).^{66,67}

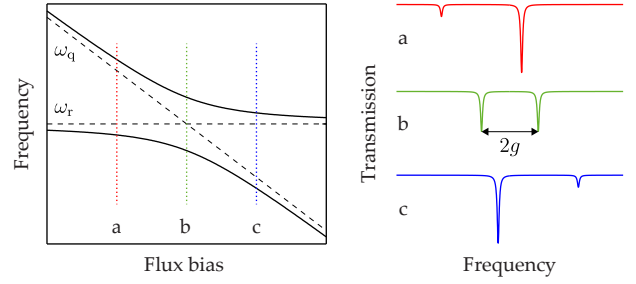


FIG. 12. Anticrossing due to strong qubit-resonator coupling for the circuit shown in Fig. 10(a). The splitting when $\omega_q = \omega_r$ is $2g$.

C. Strong (Transverse) Coupling

In this subsection, we consider how to quantify the strength of the transverse coupling because the current standard qubit control and readout methods are based on the transverse coupling.⁶ For efficient qubit control and readout, we need a reasonably strong qubit-resonator coupling; otherwise, the signal will be too small and the control will be too slow. Similarly, we also need a strong qubit-qubit interaction for efficient two-qubit gate operation. (See Secs. VIB 1 and VID for further explanation.) Then, what are the criteria that must be satisfied to be called a strong coupling?

The strength of the qubit-resonator coupling is usually characterized by three quantities: g , κ , and γ [Fig. 10(a)]. Here, $g/2\pi$ is the transverse coupling strength in Hz, $\kappa/2\pi$ is the loss rate of photons from the resonator, i.e., the spectral linewidth of the resonator, in Hz ($\kappa = \omega_r/Q$, where Q is the quality factor of the resonator), and $\gamma/2\pi (= 1/\pi T_2)$ is the transverse relaxation rate, i.e., the spectral linewidth, of the qubit in Hz. When the system satisfies $g > \kappa/2$, $\gamma/2$, the coupling is regarded as a strong coupling. The physical meaning is clear: to ensure a strong qubit-resonator interaction, the photon must stay in the resonator and the qubit needs to keep its coherence while the two systems exchange their energy.

The experimental signature of a strong qubit-resonator or qubit-qubit coupling is an anticrossing called the vacuum Rabi splitting (Fig. 12). Such a situation is well described by the Jaynes–Cummings Hamiltonian [Eq. (41)]. In the Jaynes–Cummings Hamiltonian, when the qubit and the resonator are far off-resonance, the ground state of the entire system is roughly given by $|g0\rangle$ (biases a and c in Fig. 12), where $|ij\rangle$ denotes the quantum state where the i th state of the bare qubit and the j th state of the bare resonator are occupied. At on-resonance, the ground state becomes $(|g1\rangle + |e0\rangle)/\sqrt{2}$ because of the

⁶ There are many studies on the potential use of the longitudinal qubit-resonator coupling for quantum computation. Interested readers should see Refs. 61, 63–65

hybridization between the qubit state and the resonator state (bias b in Fig. 12). In the time domain, the population of the two systems oscillates out-of-phase. This oscillation is called the vacuum Rabi oscillation.

The physics of the vacuum Rabi splitting/oscillation can be understood using our classical oscillators in Sec. V A. When the coupling is static and there is no external drive, Eq. (27) can be written in the Hamiltonian form

$$\mathcal{H} = \underbrace{\frac{p_1^2}{2m_1} + \frac{k_1 + \kappa_0}{2}x_1^2}_{\mathcal{H}_{\text{osc1}}} + \underbrace{\frac{p_2^2}{2m_2} + \frac{k_2 + \kappa_0}{2}x_2^2}_{\mathcal{H}_{\text{osc2}}} - \underbrace{\kappa_0 x_1 x_2}_{\mathcal{H}_c}. \quad (47)$$

The energy exchange and frequency splitting shown in Fig. 9(a) is caused by the coupling term \mathcal{H}_c . Thus, this coupling term corresponds to the transverse coupling.⁷ Although our classical oscillators show essentially the same physics, the vacuum Rabi splitting/oscillation is a highly quantum phenomenon because it is a consequence of coupling between the qubit and the *vacuum* mode of the resonator.

The strong transverse qubit-qubit coupling also yields a similar anticrossing. However, the transition probability, i.e., the strength of the signal, near the anticrossing is more complex than that of the qubit-resonator coupling. The reason is that there are two types of symmetry, triplet and singlet, associated with the quantum states of two entangled qubits, and transitions between different symmetries are forbidden.^{66,68}

Note that, compared with other quantum systems, superconducting planar circuit is particularly convenient system for realizing a strong coupling because the low-dimensional nature of this system results in a strongly concentrated electromagnetic field profile and consequently produces a large $V_{r,0}$ in Eq. (34).

VI. IMPLEMENTATION OF QUANTUM COMPUTATION

A. Equation of Motion

To implement functions required for quantum computation, we need to know how our qubits evolve during various operations. For a closed quantum system, the evolution of a density matrix $\hat{\rho}$ is fully described by the von

Neumann equation:

$$\frac{d\hat{\rho}}{dt} = \frac{1}{i\hbar}[\hat{\mathcal{H}}, \hat{\rho}], \quad (48)$$

where $\hat{\mathcal{H}}$ is the Hamiltonian of the system that the density matrix represents. Note that Eq. (48) is in the Schrödinger picture; in the Heisenberg picture, the density matrix is not time-dependent. If $\hat{\mathcal{H}}$ is time-independent, the solution of Eq. (48) is given by

$$\hat{\rho}(t) = e^{-i\hat{\mathcal{H}}t/\hbar}\hat{\rho}(0)e^{i\hat{\mathcal{H}}t/\hbar} = \hat{U}(t)\hat{\rho}(0)\hat{U}^\dagger(t), \quad (49)$$

which is the density matrix version of Eq. (10).

However, a qubit is actually an open quantum system—it is always interacting with the environment, a readout resonator, and other control lines, resulting in the relaxation of a quantum state as discussed in Sec. IV. Thus, this relaxation phenomenon have to be included in the equation of motion for precise control. To simplify the situation, we introduce three assumptions. The first one is the Born approximation, which assumes that the interaction between the qubit and the environment is reasonably weak such that the environment is practically unaffected by the system. The second one is the Markovian approximation, which assumes that the noise process acting on the system is memoryless. In other words, the internal dynamics of the environment hides any entanglement with the system as quickly as it arises. The last one is that the initial states of the system and environment are not entangled, i.e., $\hat{\rho}(t=0) = \hat{\rho}_{\text{sys}} \otimes \hat{\rho}_{\text{env}}$. With these approximations, the dynamics of the qubit can be well described by the Lindblad master equation, which is given by^{53,69}

$$\frac{d\hat{\rho}}{dt} = \frac{1}{i\hbar}[\hat{\mathcal{H}}, \hat{\rho}] + \sum_k \left(\hat{\mathcal{L}}_k \hat{\rho} \hat{\mathcal{L}}_k^\dagger - \frac{1}{2} \{ \hat{\mathcal{L}}_k^\dagger \hat{\mathcal{L}}_k, \hat{\rho} \} \right). \quad (50)$$

To describe the dynamics of the qubit properly, we need to choose the Lindblad operator $\hat{\mathcal{L}}_k$ based on the model we have. For example, the effects of an environment on a single qubit can be modeled by

$$\hat{\mathcal{L}}_1 = \sqrt{\Gamma_{\parallel}} \hat{\sigma}_-, \quad \hat{\mathcal{L}}_2 = \sqrt{\frac{\Gamma_{\varphi}}{2}} \hat{\sigma}_z. \quad (51)$$

Here, $\hat{\mathcal{L}}_1$ describes the thermalization process, i.e., the transition from $|1\rangle$ to $|0\rangle$ ($\hat{\sigma}_-$), and $\hat{\mathcal{L}}_2$ describes the dephasing process. Other effects can also be considered by introducing additional Lindblad operators. The unit of $\hat{\mathcal{L}}_k$ is $[\text{s}^{-1/2}]$.

Let us solve the equation with $\hat{\mathcal{L}}_1$ only for simplicity. Using the identity $\hat{\mathcal{L}}_1^\dagger \hat{\mathcal{L}}_1 = \Gamma_{\parallel} |1\rangle\langle 1|$ in Eq. (50), we obtain

$$\frac{d}{dt} \begin{pmatrix} \rho_{00} & \rho_{01} \\ \rho_{10} & \rho_{11} \end{pmatrix} = \Gamma_{\parallel} \begin{pmatrix} \rho_{11} & -\rho_{01}/2 \\ -\rho_{10}/2 & -\rho_{11} \end{pmatrix}. \quad (52)$$

⁷ There is no longitudinal coupling in our classical oscillators because this system is harmonic. The state of a harmonic system, i.e., boson, cannot be represented in the Bloch sphere because there is no well-defined geometrical quantization axis. However, bosons can couple to each other and exchange their energy; we just call this coupling transverse to be consistent with that for fermionic systems.

Solving this is straightforward:

$$\begin{pmatrix} \rho_{00}(t) & \rho_{01}(t) \\ \rho_{10}(t) & \rho_{11}(t) \end{pmatrix} = \begin{pmatrix} 1 - \rho_{11}(0)e^{-\Gamma_{\parallel}t} & \rho_{01}(0)e^{-\Gamma_{\parallel}t/2} \\ \rho_{10}(0)e^{-\Gamma_{\parallel}t/2} & \rho_{11}(0)e^{-\Gamma_{\parallel}t} \end{pmatrix}. \quad (53)$$

Note that the diagonal elements decay with the time constant Γ_{\parallel} , whereas the off-diagonal elements decay with $\Gamma_{\parallel}/2$. This explains Eq. (18).

The Lindblad master equation can also be applied to a resonator. In this case,

$$\hat{\mathcal{L}} = \sqrt{\frac{\kappa}{2\pi}} \hat{a}. \quad (54)$$

Although the Lindblad master equation is an appropriate tool to describe the dynamics of a quantum system induced by uncontrolled interactions with the environment, we need another formalism that describes the interaction between the system and a “controlled” environment, such as traveling electromagnetic fields through transmission lines, to model an actual experiment. Input-output theory is a theory for this. Here, “input” refers to the field that drives the system and “output” refers to the field that propagates away from the system. Interested readers should see Refs. 70–72.

B. Readout

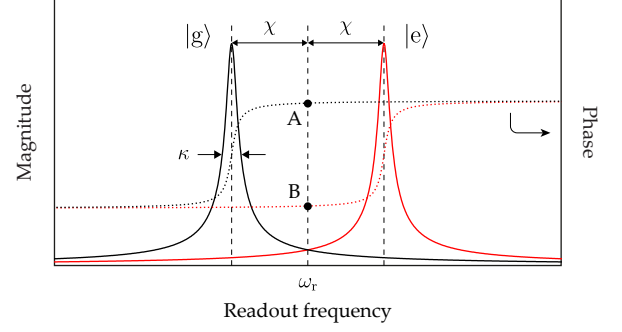
1. Dispersive Readout

Readout of a qubit state means to transfer the information of the qubit state to a change in a physical quantity of a classical device. At the time of writing, the standard method of detecting the superconducting qubit state is dispersive readout, i.e., detecting the qubit state by observing the shift in the resonance frequency of a readout resonator interacting with the qubit [Fig. 13(a)].

Advantages of dispersive readout are that (i) it does not rely on the dominant degree of freedom of a qubit, such as charge or flux, and (ii) its nondestructive nature. Before dispersive readout, a single-electron transistor was employed for island-based qubit readout and a DC SQUID was used for loop-based qubit readout because of their excellent sensitivity to charge and flux, respectively. The problem was that if the eigenstates of the qubit show significant spread or superposition in the number or phase basis [Fig. 5(d) and (e)], which happens in all noise-resilient qubits mentioned in Sec. IV B, these quantity-specific detection methods are not effective and often suffer from a strong backaction that disturbs the subsequent evolution of the measured observable. As a result, the qubit state becomes uncertain after the readout. This prevents any feedback scheme based on the measurement outcome.

In the dispersive readout scheme, a qubit state is detected and controlled by a resonator via a strong qubit-

(a) Shift in resonator frequency: dispersive shift



(b) Shift in qubit frequency: number splitting

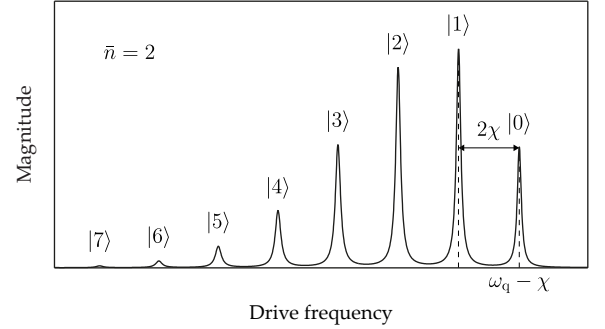


FIG. 13. (a) Qubit-state-dependent shift in resonator frequency. This frequency shift, called the dispersive shift, allows us to detect the qubit state by monitoring the S-parameters of the circuit. For the circuit shown in Fig. 10(a), the qubit state can be inferred by measuring the transmission of the circuit at ω_r . If the measured phase is A, then the qubit state is $|g\rangle$; if the phase is B, the qubit state is $|e\rangle$. (b) Resonator-state-dependent shift in qubit frequency. In the strong coupling regime, the qubit frequency can be split by the photon-state-dependent frequency shift. The resonator state is assumed to be a coherence state whose average photon number is \bar{n} . This figure was obtained by solving the Lindblad equation [Eq. (50)] with Eqs. (51), (54), and (57). For the solution, QuTiP was used.^{73,74}

resonator interaction. However, near on-resonance ($\omega_q \approx \omega_r$), we cannot selectively detect or control the qubit state because, in this regime, the strong qubit-resonator interaction hybridizes the qubit and resonator states (see Sec. V C). Hence, we detune ω_q such that the qubit-resonator detuning $\Delta_{qr} (\equiv \omega_r - \omega_q)$ is much greater than g and κ . This limit is called the dispersive limit. In this off-resonant regime, a qubit transition induced by photon exchange with the resonator is negligible. However, the qubit shows small but easily measurable frequency shifts that depend on the resonator state; at the same time, the resonator also shows a small frequency shift that depends on the qubit state. The qubit state is detected by measuring this frequency shift of the resonator.

To see the physics in the dispersive limit more clearly, we consider the Jaynes-Cummings Hamiltonian $\hat{\mathcal{H}}_{JC}$

[Eq. (41)]. Here, we treat the qubit-resonator interaction $\hat{\mathcal{H}}_{\text{qr}}$ [Eq. (40)] as the perturbation to the uncoupled qubit-resonator Hamiltonian $\hat{\mathcal{H}}_0$ [Eq. (38)]. Then, we take a unitary transformation that diagonalizes $\hat{\mathcal{H}}_{\text{JC}}$ perturbatively to first order in $\hat{\mathcal{H}}_{\text{qr}}$. Such a transformation is called the Schrieffer–Wolff transformation.^{75,76} (The same results can be obtained using the standard perturbation theory.^{53,62}) A unitary operator $\hat{U}_{\text{disp}} = e^{\hat{S}}$ for the Schrieffer–Wolff transformation is defined such that $\hat{S}^\dagger = -\hat{S}$ and $[\hat{S}, \hat{\mathcal{H}}_0] = -\hat{\mathcal{H}}_{\text{qr}}$. Then, we have (use the formulas in Table V)

$$\begin{aligned}\hat{\mathcal{H}}_{\text{JC}}^{\text{disp}} &= \hat{U}_{\text{disp}} \hat{\mathcal{H}}_{\text{JC}} \hat{U}_{\text{disp}}^\dagger \\ &= \hat{\mathcal{H}}_0 + \hat{\mathcal{H}}_{\text{qr}} + [\hat{S}, \hat{\mathcal{H}}_0] + [\hat{S}, \hat{\mathcal{H}}_{\text{qr}}] \\ &\quad + \frac{1}{2}[\hat{S}, [\hat{S}, \hat{\mathcal{H}}_0]] + \frac{1}{2}[\hat{S}, [\hat{S}, \hat{\mathcal{H}}_{\text{qr}}]] + \cdots \\ &\approx \hat{\mathcal{H}}_0 + \frac{1}{2}[\hat{S}, \hat{\mathcal{H}}_{\text{qr}}].\end{aligned}\quad (55)$$

In our case, \hat{U}_{disp} is given by

$$\hat{U}_{\text{disp}} = \exp\left[\frac{g}{\Delta_{\text{qr}}}(\hat{\sigma}_- \hat{a}^\dagger - \hat{\sigma}_+ \hat{a})\right].\quad (56)$$

From Eq. (55), we obtain

$$\hat{\mathcal{H}}_{\text{JC}}^{\text{disp}} \approx \hbar(\omega_{\text{q}} - \chi)\frac{\hat{\sigma}_z}{2} + \hbar(\omega_{\text{r}} - \chi\hat{\sigma}_z)\hat{a}^\dagger \hat{a},\quad (57)$$

where $\chi \equiv g^2/\Delta_{\text{qr}}$. The second term in Eq. (57) shows that the resonator frequency shifts by $\mp\chi$, depending on the qubit state [Fig. 13(a)]. Therefore, dispersive readout detects the longitudinal component of the Bloch vector. This is the novel feature of the dispersive readout—creating a qubit-resonator interaction with $\hat{\sigma}_z$, which enables us to detect the qubit state, from a purely transverse interaction by taking the dispersive limit.

Note that the dispersive term $[\chi\hat{\sigma}_z\hat{a}^\dagger\hat{a}]$ in Eq. (57) commutes with the bare qubit and bare resonator terms; in other words, measuring the qubit state does not disturb the subsequent evolution of the qubit and resonator, meaning that the dispersive readout scheme is nondestructive. Such a measurement scheme is called Quantum NonDemolition (QND) measurement.^{53,77,78} Here, we emphasize that the term “nondemolition” does not mean the absence of wavefunction collapse. If the measurement scheme is QND-type, a measured qubit remains in the eigenstate that we record as a measurement outcome, and subsequent measurements reproduce the outcome of the first measurement.

For quantum error correction, the state of an ancilla qubit (see Sec. VII) must be determined in a single shot—without averaging the output signals of repeated identical measurements. Thus, maximizing the Signal-to-Noise Ratio (SNR) is crucial. While we can enhance the SNR by increasing the probe power, i.e., the average number of photons \bar{n} for the detection of the resonator state, \bar{n}

must be significantly less than the critical photon number n_{crit} , which is given by $\Delta_{\text{qr}}/4g^2$ (Ref. 55). If not, Eq. (57) would no longer be valid. Then, the readout process is no longer QND, and the photons induce an unwanted qubit transition as a backaction.⁷⁹ The resulting change in qubit population during the readout process reduces the readout fidelity. In experiments, it was found that \bar{n} must be $\lesssim 10$ for high-fidelity readout.^{79,80}

The next question we have to consider is the following: with a given \bar{n} , what is the optimal readout condition that ensures fast readout with high fidelity? From Fig. 13(a), we can see that κ should not be too large compared with χ ; otherwise, the frequency shift would be difficult to observe. The opposite limit, the small κ limit, is not so good either—it would make the readout process inefficient because photons would stay too long in the resonator, resulting in a small signal. Careful theoretical and experimental studies^{80,81} found that the condition for the best SNR is $2\chi = \kappa$. In experiments, the quality factor ($=\omega_{\text{r}}/\kappa$) of the readout resonator is usually designed to be on the order of 100–1000 (Ref. 82). If we lower the quality factor further, the readout process will be faster; however, achieving a comparable χ might not satisfy the dispersive limit because a large χ is achieved by either enhancing g or reducing Δ_{qr} . Moreover, if g is on the order of $0.1\omega_{\text{q}}$ or larger, the qubit-resonator coupling enters the so-called ultrastrong coupling regime, in which the RWA is no longer applicable.^{83,84}

Another important phenomenon that must be considered is the Purcell effect that refers to the increase in the spontaneous emission rate of a qubit, i.e., the reduction in T_1 , by the resonator coupled to the qubit. The Purcell effect is maximized when $\omega_{\text{q}} = \omega_{\text{r}}$ because it is caused by the resonator concentrating the density of decay channels.⁶² Therefore, if Δ_{qr} is not large enough, T_1 will be severely limited.⁵⁶ The problem is that a large Δ_{qr} is not always desirable because the resulting χ might be too small to ensure a high readout fidelity. To maximize the readout fidelity while maintaining the fast readout capability, the Purcell filter was developed. Contrary to the Purcell effect, the Purcell filter “filters out” the density of decay channels near the qubit transition frequency; hence, it protects the qubit from the unwanted acceleration of energy relaxation. For details, see Refs. 85 and 86.

In a real experiment, the measured dispersive shift can be significantly different from the value of g^2/Δ_{qr} because of the contribution from higher excitation levels interacting with the resonator. To fully account for this contribution, we also need to calculate g_{ij} using Eq. (34), and $\chi_{ij} = |g_{ij}|^2/(\omega_{\text{r}} - \omega_{i-j})$, where ω_{i-j} is the energy *released* in the transition from $|i\rangle$ to $|j\rangle$ ($i \neq j$). (Note that ω_{i-j} is negative when $i < j$.) The total dispersive shift χ_{total} , which is what we observe in experiments, is given by $\sum_{j=0}^M[(\chi_{j1} - \chi_{1j}) - (\chi_{j0} - \chi_{0j})]/2$, where M is the cut-off energy level.^{87,88} Fortunately, by considering χ_{total} as an empirical χ , we can understand the readout process with the physics explained in this section.

We can also write Eq. (57) in the following form:

$$\hat{\mathcal{H}}_{JC}^{\text{disp}} \approx \hbar[\omega_q - \chi(1 + 2\hat{a}^\dagger\hat{a})]\frac{\hat{\sigma}_z}{2} + \hbar\omega_r\hat{a}^\dagger\hat{a}. \quad (58)$$

In this form, we can interpret the χ term as the Lamb (1 in parentheses) and AC Stark ($2\hat{a}^\dagger\hat{a}$) shifts in qubit frequency. This suggests that a different photon number state of the resonator yields a different shift in the qubit frequency, resulting in the splitting of the qubit spectrum, called number splitting, as shown in Fig. 13(b). Note that the AC Stark shift makes the qubit lose its phase coherence because the qubit state interacting with a different number state acquires different phases during the evolution. Such a process is called measurement-induced dephasing.

For the physics we have explored thus far, the dispersive readout process can be described as follows:⁸¹ (i) A set of photons, the energy of each of which is about ω_r , enter the resonator. (ii) The qubit state information is encoded to the photons, for example, as the phase of the transmission, by the qubit-resonator interaction. The measurement-induced dephasing caused by the same interaction makes the qubit state lose its phase coherence and collapse into $|0\rangle$ or $|1\rangle$. (iii) The photons escape from the resonator and are then detected.

2. Josephson Parametric Amplifier

Although dispersive readout can give a reasonably good SNR, achieving single-shot readout is still difficult because the SNR is deteriorated by thermal noise during travel from the chip to the room-temperature instruments. This is an inevitable consequence of the limited number of microwave photons, the energy of each of which is orders of magnitude smaller than the room-temperature thermal energy. Hence, the pre-amplification of the signal before detection is indispensable. One might think that using multiple amplifiers will solve the problem. However, this is not a good option because, if a signal passes a chain of amplifiers, the SNR is primarily established by the noise figure of the first amplifier in the chain (Friis formula). Therefore, having a good amplifier immediately after the qubit is important.

Commercially available High-Electron-Mobility Transistor (HEMT) amplifiers are widely used and installed in the output microwave wiring (at the 4K plate of the dilution refrigerator), typically providing a gain of 30–40 dB. Although an HEMT amplifier has a high gain and broad operation bandwidth, it adds on an average of 10–20 noise photons to the signal photons, which in turn worsens the SNR. To overcome this, practically noiseless parametric amplifiers were developed using Josephson junctions.

A parametric amplifier basically transfers energy from a strong pump to a weak signal by mixing the signal and pump frequencies via the modulation of the reac-

tance. Hence, the reactance is a time-varying parameter, from which the name of the amplifier originates. This type of amplifier has low noise because it modulates the reactance instead of the resistance. In superconducting circuits, a variable inductor can be implemented using Josephson junctions, hence the name Josephson Parametric Amplifier (JPA).

The physics of parametric amplification was introduced in Fig. 9(b): x_1 and x_2 correspond to the signal (non-zero initial value) and the idler (zero initial value), respectively. Here, the idler is a tone generated during the amplification process as a consequence of the energy conservation: $\omega_m = \omega_s + \omega_I$, where ω_m is the modulation frequency, ω_s is the signal frequency, and ω_I is the idler frequency.

In general, JPAs can be categorized on the basis of two factors. One is how to maximize the time for energy transfer from the pump to the signal. This can be achieved by using either a resonator (multiple bounces in a cavity) or a long waveguide. The other is how to modulate the inductance. Depending on the modulation method or operation conditions, ω_m can be either the same or twice the pump frequency ω_p .

For further explanation, we present a resonator-based JPA in Fig. 14(a) as an example. Note that the $\lambda/4$ resonator is terminated with a DC SQUID with a flux bias. As mentioned in Sec. IIIB, a DC SQUID is a variable junction whose effective inductance $L_{J,\text{eff}}$ is given by

$$\begin{aligned} L_{J,\text{eff}}(\varphi_{\text{ext}}) &= \left(\frac{\Phi_0}{2\pi}\right)^2 \frac{1}{E_{J,\text{eff}}(\varphi_{\text{ext}})} \\ &= \left(\frac{\Phi_0}{2\pi}\right)^2 \frac{1}{2E_J} \frac{1}{|\cos(\varphi_{\text{ext}}/2)|}. \end{aligned} \quad (59)$$

Here, Eq. (14) is used with the assumption that $E_{J1} = E_{J2} = E_J$. By varying the flux bias, we can modulate the inductance [red coil in Fig. 14(a)]. This type of modulation is called flux pumping.⁸⁹ Here, we decompose φ_{ext} into the DC component $\varphi_{\text{ext}}^{\text{dc}}$ and the pump component $\varphi_{\text{ext}}^{\text{p}}$. We can operate the amplifier in two regimes depending on $\varphi_{\text{ext}}^{\text{dc}}$:

1. If $\varphi_{\text{ext}}^{\text{dc}} = 0$ [bias a in Fig. 14(b)], $L_{J,\text{eff}}$ varies quadratically with $\varphi_{\text{ext}}^{\text{p}}$ because $1/\cos(x/2) \approx 1 + x^2/8$. This results that $\omega_m = 2\omega_p$, where $\omega_p = \omega_r$. Such a process is called the four-wave mixing process (ω_s , ω_I , and two ω_p).
2. For a suitable value of $\varphi_{\text{ext}}^{\text{dc}}$, we can have an appreciable contribution from the linear term in Eq. (59). Bias b in Fig. 14(b) is an example of this. In this case, $\omega_m = \omega_p$. The parametric amplification of the signals is then achieved by applying a pump tone with $\omega_p = 2\omega_r$. This process is called the three-wave mixing process (ω_s , ω_I , and one ω_p). Advantages of this operation are that (i) we can easily separate the pump tone and the signal in the frequency domain, and (ii) we can tune ω_r by adjusting $\varphi_{\text{ext}}^{\text{dc}}$.

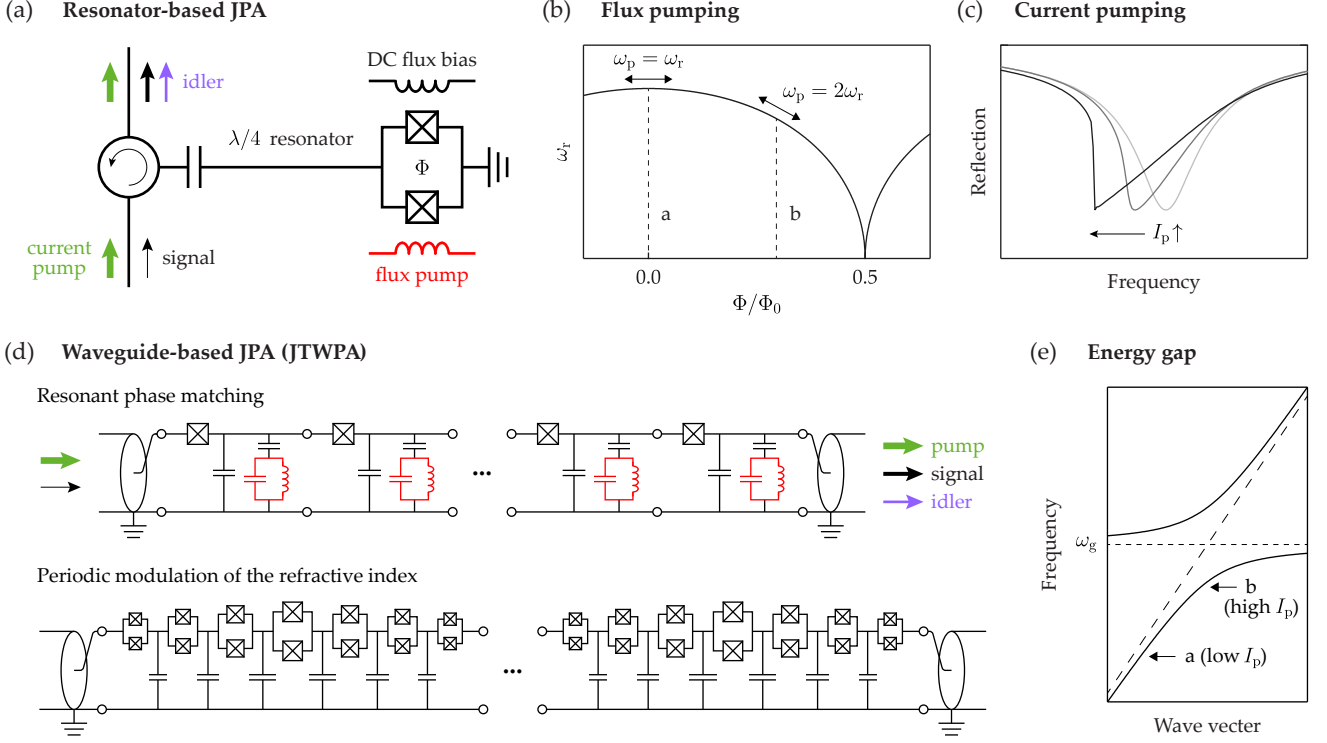


FIG. 14. (a) Josephson Parametric Amplifier (JPA) based on a quarter-wavelength resonator terminated by a DC SQUID for which the tunability is provided by a DC flux bias Φ . During the amplification process, another frequency tone is generated, called the idler, to satisfy the energy conservation. This type of JPA can be operated by either a flux pump or a current pump. (b) DC flux bias Φ dependence of ω_r . At zero DC bias (bias a), the pump frequency ω_p must be the same as ω_r to have parametric amplification, whereas ω_p can be $2\omega_r$ for an appreciable amount of DC bias (bias b). (c) Pump current I_p dependence of the resonator line shape. As I_p increases, the resonance frequency decreases because of the inductive contribution from I_p . (d) Schematic circuit diagrams of a Josephson Traveling-Wave Parametric Amplifier (JTWPA). The phases of interacting tones can be matched either by resonant structures (in red) or by the periodic modulation of the refractive index, i.e., the junction size. The inductance of this amplifier is modulated by current pump. (e) Dispersion relation engineered to have a gap at the frequency ω_g for phase matching. The long-dashed diagonal line shows the dispersion relation without the gap. Frequencies a and b are examples of possible pump frequencies at low and high pump currents, respectively.

There is another method for the inductance modulation, called current pumping [green arrows in Fig. 14(a)].⁹⁰ In this method, the inductance of a JPA is modulated by applying a large current, i.e., pumping current, flowing through the Josephson junctions. Roughly speaking, the number of charge carriers, i.e., Cooper pairs, is locally and partially reduced in a Josephson junction owing to its weak link nature. Because of this, the charge carriers must have a higher speed near the junctions to maintain the same current in and out of the junctions. The resulting large kinetic energy of the charge carriers contributes to the inductance of the circuit, in addition to the geometric inductance. This additional inductance is called the kinetic inductance. Since the kinetic energy is proportional to the square of the velocity of the charge carriers, the kinetic inductance is roughly proportional to the square of the pump current. Thus, the current-pumped amplification is a four-wave mixing process regardless of a DC flux bias.⁹³ Such an inductive contribution from current pumping shifts the res-

onance frequency of the resonator as shown in Fig. 14(c). This characteristic line shape can be modeled as a Duffing oscillator.^{91,92}

The resonator-based JPA is relatively easy to make but suffers from a gain-bandwidth trade-off. The reason is that, to have a higher gain, the signal must bounce in the resonator more; this requires a higher quality factor and inevitably reduces the bandwidth. A waveguide-based JPA is called a Josephson Traveling-Wave Parametric Amplifier (JTWPA). A JTWPA is free from the gain-bandwidth trade-off. This allows us to achieve high-bandwidth (several gigahertz) and high-gain (> 20 dB) amplification.⁹⁴ Since the waveguide has to be nonlinear to mix the signal and pump tones, it is implemented using a long Josephson junction array with current pumping.

The challenge in making a JTWPA is the phase matching: the phases of all interacting tones (pump, signal, and idler) must be matched. (A resonator-based JPA is free from this problem because it is geometrically confined.) The phase mismatch results from changes in phase veloc-

ity, i.e., the refractive index, caused by the interaction between the strong pump tone and the nonlinear medium. To match the phase, we create a local distortion in the dispersion relation as shown in Fig. 14(e). Then, depending on the pump current I_p , a value of ω_p that matches the phase can be chosen. If I_p is very small compared to the critical current of the junction, the phase mismatch will be small; thus, a frequency where the wave vector is close to that from the linear dispersion relation (long-dashed line) will match the phase well. Frequency a in Fig. 14(e) is an example for this. For I_p comparable to the junction critical current, we have to choose a frequency where the dispersion relation deviates significantly from the linear one as ω_p ; frequency b is such an example. For actual implementation, we can either insert a resonant structure near each Josephson junction^{94,95} or periodically modulate the refractive index similarly to what is done in photonic crystals [Fig. 14(d)].⁹⁶ Here, modulating the refractive index can be achieved by modulating the size of the junctions in DC SQUIDS.

These JPAs can perform as quantum-limited amplifiers, which add only the minimum noise allowed by the laws of quantum mechanics. For a phase-preserving linear amplifier, whose gain is the same regardless of the phase of the input signal, this minimum amount of added noise is equivalent to half a photon.^{97,98} For theories of parametric amplification, including JPA, see Refs. 72, 92, 99–101.

C. Single-Qubit Gate

As mentioned in Sec. II A 2, performing a gate operation is basically engineering the system Hamiltonian such that the resulting unitary evolution of a qubit implements the target gate. From Eq. (11),

$$\hat{U} = e^{-i\hat{H}t/\hbar} = \hat{U}_{\text{target}}. \quad (60)$$

Here, the method we use to engineer the system Hamiltonian is to apply an external drive.

Since the standard qubit readout technique is dispersive readout (Sec. VI B 1), we consider a qubit-resonator system and assume that the qubit is driven via the resonator. A classical analog of this system is shown in Fig. 9(c). As we drive oscillator 1 (control oscillator) with $f_d = f_2$, the amplitude of oscillator 2 (target oscillator) increases indefinitely. However, this does not happen for a qubit because it is intrinsically a nonlinear quantum object. Instead, the population of the qubit oscillates as a function of time or the amplitude of the drive. This oscillation in the qubit population is called the Rabi oscillation (Fig. 15).

Now we consider the counterclockwise rotation of the Bloch vector about the x -axis as an example. The external drive is usually modeled quantum mechanically^{53,55}

$$\hat{\mathcal{H}}_d(t) = \hbar \mathcal{E}_r(t)(\hat{a}^\dagger e^{-i\omega_d t} + \hat{a} e^{+i\omega_d t}), \quad (61)$$

Counterclockwise rotation about the x -axis: X gate

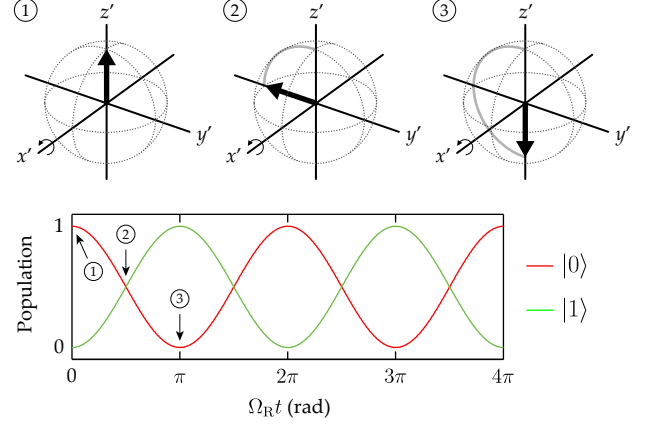


FIG. 15. Evolution of the quantum state of a single qubit in a Bloch sphere under an external drive. Gray solid lines in the Bloch spheres indicate the evolution trajectory of the qubit state. The numbers in circles indicate time steps. The rotation angle of the Bloch vector is determined by $\Omega_R t$, where Ω_R is the Rabi frequency and t is time. These two quantities correspond to the power and length of the external drive, respectively. The rotation of the Bloch vector results in an oscillation of the qubit population with a period Ω_R ; such an oscillation is called the Rabi oscillation. Note that the population of the qubit is inverted at time ③, thus implementing the X gate. The frequency of the rotating frame is the drive frequency, which is on-resonance with the qubit.

where \mathcal{E}_r and ω_d are the amplitude and frequency of the external drive, respectively. Now, we have to perform multiple transformations. First, to focus on the dispersive limit, we apply the Schrieffer–Wolff transformation (Sec. VI B 1) to Eq. (61):

$$\begin{aligned} \hat{\mathcal{H}}_d^{\text{disp}} &= \hat{U}_{\text{disp}} \hat{\mathcal{H}}_d(t) \hat{U}_{\text{disp}}^\dagger \\ &\approx \hbar \mathcal{E}_r(t)(\hat{a}^\dagger e^{-i\omega_d t} + \hat{a} e^{+i\omega_d t}) \\ &\quad - \frac{\hbar \mathcal{E}_r(t)g}{\Delta_{\text{qr}}}(\hat{\sigma}_+ e^{-i\omega_d t} + \hat{\sigma}_- e^{+i\omega_d t}), \end{aligned} \quad (62)$$

where $\Delta_{\text{qr}} \equiv \omega_r - \omega_q$. In Eq. (62), we can see that the first line corresponds to (de)populating the resonator and the second line corresponds to driving the qubit. Next, we combine Eqs. (62) and (58) to obtain the full single-qubit Hamiltonian $\hat{\mathcal{H}}_{1q}^{\text{full}}$:

$$\hat{\mathcal{H}}_{1q}^{\text{full}} \equiv \hat{\mathcal{H}}_{\text{JC}}^{\text{disp}} + \hat{\mathcal{H}}_d^{\text{disp}}. \quad (63)$$

Then, we move to the rotating frame whose Hamiltonian is defined by

$$\hat{\mathcal{H}}_0 = \hbar \omega_d \left(\hat{a}^\dagger \hat{a} + \frac{\hat{\sigma}_z}{2} \right). \quad (64)$$

The final single-qubit Hamiltonian in the rotating frame

$\hat{\mathcal{H}}_{1q}^{\text{rot}}$ can be obtained by the unitary transformation:

$$\begin{aligned}\hat{\mathcal{H}}_{1q}^{\text{rot}} &= e^{i\hat{\mathcal{H}}_0 t/\hbar}(\hat{\mathcal{H}}_{1q}^{\text{full}} - \hat{\mathcal{H}}_0)e^{-i\hat{\mathcal{H}}_0 t/\hbar} \\ &= \hbar(\omega_r - \omega_d)\hat{a}^\dagger\hat{a} + \hbar\mathcal{E}_r(t)(\hat{a} + \hat{a}^\dagger) \\ &\quad + \hbar[\omega_q - \chi(1 + 2\hat{a}^\dagger\hat{a}) - \omega_d]\frac{\hat{\sigma}_z}{2} + \hbar\Omega_R\frac{\hat{\sigma}_x}{2},\end{aligned}\quad (65)$$

where Ω_R is the Rabi frequency given by $-4\mathcal{E}_r g/\Delta_{qr}$, whose physical meaning will be clarified in Eq. (67). For these transformations, we use the formulas in Table V.

As mentioned in Sec. VIB 1, the number of photons in the readout resonator has to be close to zero to maintain the phase coherence of the qubit. Thus, if we choose $\omega_d = \omega_q - \chi$, then the term relevant to the qubit dynamics in Eq. (65) is

$$\hat{\mathcal{H}}_d^{\text{rot}} = \hbar\Omega_R\frac{\hat{\sigma}_x}{2}. \quad (66)$$

Using Eq. (7), we can obtain the evolution driven by Eq. (66) with the time τ :

$$\begin{aligned}\hat{U}(\tau) &= e^{-i\hat{\mathcal{H}}_d^{\text{rot}}\tau/\hbar} \\ &= \begin{pmatrix} \cos(\Omega_R\tau/2) & -i\sin(\Omega_R\tau/2) \\ -i\sin(\Omega_R\tau/2) & \cos(\Omega_R\tau/2) \end{pmatrix}.\end{aligned}\quad (67)$$

Equation (67) is basically a rotation matrix describing a rotation of a Bloch vector around the x' -axis as shown in Fig. 15. This rotation results in an oscillation of the qubit population, the z' component of the Bloch sphere, with a period $\Omega_R\tau = 2\pi$ if we ignore the global phase factor. This is the Rabi oscillation. Using this, the X gate can be implemented by an external drive satisfying $\Omega_R\tau = \pi$. This is the main mechanism for how we flip a qubit.

One might ask how the rotation axis is defined in a real experiment. The answer is that the reference phase of the instruments, such as the phase of the first pulse in the experiment, defines the rotation axis, which is usually set as x (Ref. 102). If we want to change the rotation axis from x to y , then all we have to do is to add a $\pi/2$ phase shift to the subsequent pulses and the reference phase of the measurement instruments. This means that, if we set the x rotation $\cos(\omega t)$, then the y rotation is $-\sin(\omega t)$. (Do not omit the minus sign!)

Note that changing the rotation axis from x to y is actually a z rotation. This suggests that shifting the reference phase of the instruments is functionally equivalent to a rotation about the z -axis, which is called a virtual z rotation.¹⁰³ Since we do not apply a real pulse for this, the virtual z rotation is a nearly perfect and zero-time operation.

D. Two-Qubit Gate

Many two-qubit gates have been implemented by various methods. Among them, four gates and four methods

are introduced in this tutorial. These methods are based on the transverse qubit-qubit interaction whose physics is explored in Sec. V A. The two-qubit gates introduced in this tutorial are summarized in Table III.

1. iSWAP: Coherent Exchange

This method implements a two-qubit gate using changes in the phase and population of the qubit states during the coherent exchange of a photon. The basic mechanism for this is tuning the transition frequency of one of the qubits so that $\omega_{q1} = \omega_{q2}$. The relevant analogy for this is shown in Fig. 9(a).

Consider two capacitively coupled transmons. This system is convenient because the dominant qubit-qubit coupling is transverse, as pointed out in Sec. V B 2, and it is the most popular qubit system. For simplicity, we ignore the readout resonators as qubits are usually far detuned from the resonators. Then, the system Hamiltonian reduces to Eq. (44). After taking the RWA (Sec. V B 2), Eq. (44) can be written in a similar manner to Eq. (41):

$$\hat{\mathcal{H}}_{2q} = \hbar\omega_{q1}\frac{\hat{\sigma}_z^{(1)}}{2} + \hbar\omega_{q2}\frac{\hat{\sigma}_z^{(2)}}{2} + \hbar J(\hat{\sigma}_+^{(1)}\hat{\sigma}_-^{(2)} + \hat{\sigma}_-^{(1)}\hat{\sigma}_+^{(2)}). \quad (68)$$

The resulting energy levels are shown in Fig. 16(a).

Now, we assume that $\omega_{q1} = \omega_{q2}$. To focus on the dynamics induced by the qubit-qubit coupling, we move to the rotating frame with the frequency ω_{q1} . Then, Eq. (68) becomes

$$\hat{\mathcal{H}}_{2q}^{\text{rot}} = \hbar J(\hat{\sigma}_+^{(1)}\hat{\sigma}_-^{(2)} + \hat{\sigma}_-^{(1)}\hat{\sigma}_+^{(2)}). \quad (69)$$

This equation is the same as Eq. (46) with the RWA. The propagator based on $\hat{\mathcal{H}}_{2q}^{\text{rot}}$ with the time interval τ is

$$\begin{aligned}\hat{U}(\tau) &= e^{-i\hat{\mathcal{H}}_{2q}^{\text{rot}}\tau/\hbar} \\ &= \begin{pmatrix} 1 & 0 & 0 & 0 \\ 0 & \cos(J\tau) & -i\sin(J\tau) & 0 \\ 0 & -i\sin(J\tau) & \cos(J\tau) & 0 \\ 0 & 0 & 0 & 1 \end{pmatrix}.\end{aligned}\quad (70)$$

Note that Eq. (70) is practically the same as Eq. (67) because only two states, $|01\rangle$ and $|10\rangle$, contribute to the dynamics.

Equation (70) is easy to derive if we use Eq. (7) with $\alpha = J\tau$ and

$$\hat{\sigma}_+^{(1)}\hat{\sigma}_-^{(2)} + \hat{\sigma}_-^{(1)}\hat{\sigma}_+^{(2)} = \begin{pmatrix} 0 & 0 & 0 & 0 \\ 0 & 0 & 1 & 0 \\ 0 & 1 & 0 & 0 \\ 0 & 0 & 0 & 0 \end{pmatrix} \equiv \begin{pmatrix} 0 & 0 & 0 & 0 \\ 0 & \hat{A} & 0 & 0 \\ 0 & 0 & 0 & 0 \\ 0 & 0 & 0 & 0 \end{pmatrix}. \quad (71)$$

One useful two-qubit gate that can be implemented easily by this method is the iSWAP gate. The iSWAP

TABLE III. Various two-qubit gates. From the columns “Tunable frequency” to “Small ω_q separation”, the name of each column indicates the required condition for implementation. Here, the condition “Tunable frequency” implies that at least one of the qubits has to be out of its sweet spot during the gate operation. Note that these conditions are minimal conditions; having an additional condition can result in better performance. For example, it was reported that the CZ gate can be implemented with high fidelity by adiabatic excursion with one tunable qubit and tunable coupling,¹⁰⁸ or by coherent exchange with two tunable qubits and fixed coupling,¹⁰⁵ although the minimal condition for the CZ gate implementation is one tunable qubit as shown in this table. “Small ω_q separation” means how close two qubit frequencies need to be; the value “Yes” means that $|\omega_{q1} - \omega_{q2}|$ is comparable to or less than the anharmonicity of the qubit. “Distance to CNOT” means the minimum number of two-qubit gates needed to implement the CNOT gate. Each value in this column is an intrinsic property of the corresponding gate; values do not depend on the implementation method.

Gate	Method	Tunable frequency	Tunable coupling	Microwave drive	Negative anharmonicity	Small ω_q separation	Distance to CNOT	Ref.
iSWAP	Coherent exchange	Yes	No	No	No	No	2	105
iSWAP	Parametric coupling	No	Yes	Yes	No	No	2	106
bSWAP	Parametric coupling	No	Yes	Yes	No	No	2	106
CZ	Adiabatic excursion	Yes	No	No	Yes	No	1	107,108
CZ	Coherent exchange	Yes	No	No	Yes	No	1	105
CZ	Parametric coupling	No	Yes	No	No	No	1	109
CR	All microwave control	No	No	Yes	No	Yes	1	110,111

gate swaps the populations of $|10\rangle$ and $|01\rangle$ with an additional phase factor $-i$. In the matrix form,

$$\hat{U}_{\text{iSWAP}} = \begin{pmatrix} 1 & 0 & 0 & 0 \\ 0 & 0 & -i & 0 \\ 0 & -i & 0 & 0 \\ 0 & 0 & 0 & 1 \end{pmatrix}. \quad (72)$$

Thus, Eq. (70) with $J\tau = \pi/2$ implements Eq. (72).

The actual implementation can be done via the following steps [black arrowed path in Fig. 16(a) and lower figure in Fig. 16(c)]: (i) Prepare the initial state. In Fig. 16, $|01\rangle$ was chosen as an example. At this stage, the tunable qubit, qubit 2 in this case, is at its sweet spot. (ii) Increase the flux bias to the point at which the energy levels of $|10\rangle$ and $|01\rangle$ are equal. At this bias, the new eigenstates, $(|01\rangle \pm |10\rangle)/\sqrt{2}$, exchange their energy at a rate of J/π . (iii) Wait for a while to satisfy $J\tau = \pi/2$. (iv) Decrease the flux bias to the sweet spot.

The bias ramping in steps (ii) and (iv) must be as fast as possible for efficient gate operation. Thus, the iSWAP gate implemented using this method is a diabatic gate. For qubits with negative anharmonicity, such as the two-transmon system shown in Fig. 16(a), the gate fidelity of a diabatic gate is limited mainly by population leakage out of the computational subspace. This population leakage is driven by unwanted transitions, such as $|11\rangle$ - $|02\rangle$ and $|11\rangle$ - $|20\rangle$ transitions, because we pass anticrossings associated with $|11\rangle$ during the flux bias ramping. Note that this leakage is still a unitary evolution, suggesting that the population leakage oscillates with time. Thus, the error due to this leakage can be minimized by synchronizing the periods of the leakage and the iSWAP gate time.¹⁰⁵

2. iSWAP and bSWAP: Parametric Coupling

The previous implementation of the iSWAP gate relies on the frequency tunability of the qubit. This means that the qubit must be out of its sweet spot for a while, which potentially degrades the coherence. To resolve this issue, another scheme that allows qubits to stay at their sweet spots during the gate operation has been developed.¹¹⁴

In this scheme, the control knob is the qubit-qubit coupling. Consider the two-qubit Hamiltonian in Eq. (44). (Here, the qubits do not need to be transmons.) If J is static and $|\omega_{q1} - \omega_{q2}| \gg J$, the qubit-qubit interaction is effectively turned off, i.e., the interaction is very slow compared with the time scale we are interested in, as indicated by in Eq. (46).

Now we modulate the coupling constant as $J(t) = J_0 + J_m \cos(\omega_m t)$. Here, the modulation frequency ω_m of the coupler is the control parameter, from which the name “parametric coupling” originates. Such a modulation can be achieved by modulating flux passing through the loop of the coupler shown in Fig. 11. If $\omega_m = |\omega_{q1} - \omega_{q2}|$, the two qubits exchange their energy as we saw in Fig. 9(b). This activates the transition between $|01\rangle$ and $|10\rangle$. In this case, Eq. (46) becomes

$$\hat{\mathcal{H}}_{2q}^{\text{rot}} = \frac{\hbar J_m}{2} \left(\hat{\sigma}_+^{(1)} \hat{\sigma}_-^{(2)} + \hat{\sigma}_-^{(1)} \hat{\sigma}_+^{(2)} \right). \quad (73)$$

Using Eq. (70), we can see that $J_m \tau = \pi$ implements the iSWAP gate.

If $\omega_m = \omega_{q1} + \omega_{q2}$, we can activate the transition between $|00\rangle$ and $|11\rangle$. Using this transition, we can imple-

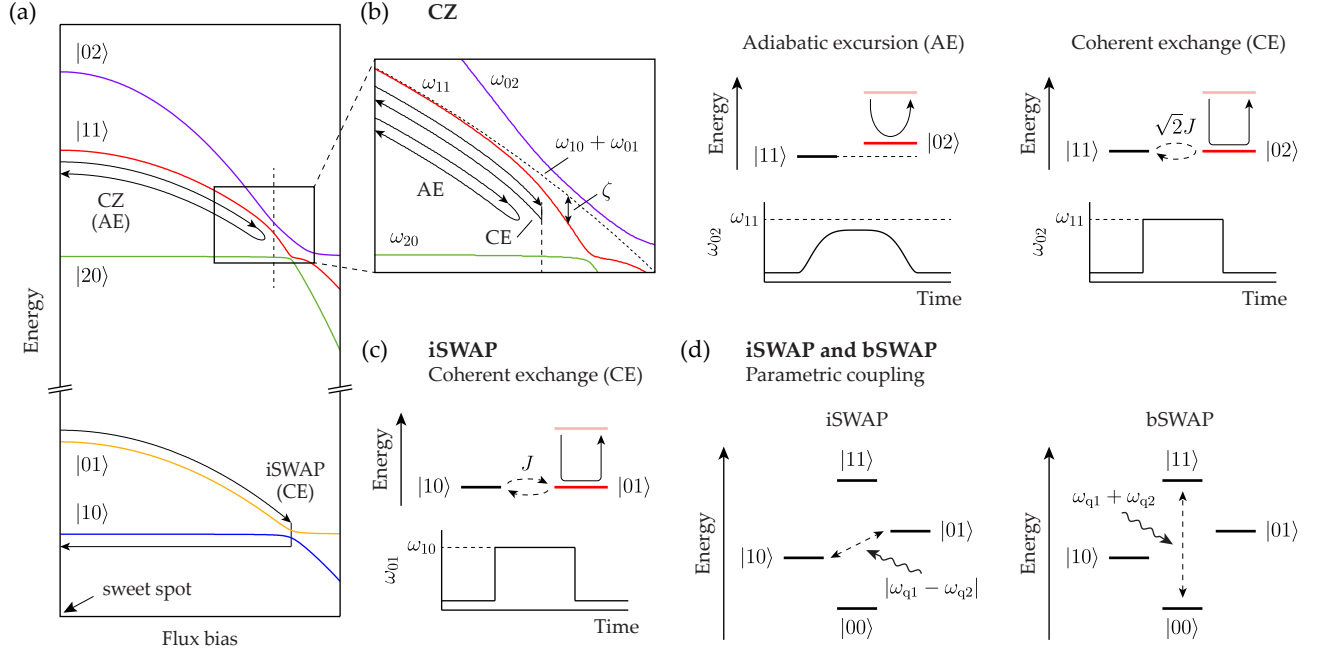


FIG. 16. (a) Energy levels of a two-transmon system as a function of flux bias.¹¹⁶ It is assumed that (i) qubit 2 is tunable, (ii) $\omega_{q2} > \omega_{q1}$ at the sweet spot, and (iii) the qubit-qubit coupling is strong as indicated by anticrossings. The sweet spot of qubit 2 is the leftmost flux bias as indicated by an arrow. The vertical dashed line in (a) indicates the bias at which the energy levels of $|02\rangle$ and $|11\rangle$ are equal. The solid lines with arrows show how the energy levels evolve during the gate operation: the lower one is the trajectory for the iSWAP gate implemented by coherent exchange, and the upper one is for the CZ gate implemented by adiabatic excursion. Here, CE stands for coherent exchange and AE stands for adiabatic excursion. (b) Implementation of the CZ gate via adiabatic excursion and coherent exchange. The left figure shows the energy levels near the anticrossing between $|11\rangle$ and $|02\rangle$ (indicated by the vertical dashed line). $\zeta (\equiv \omega_{10} + \omega_{01} - \omega_{11})$ is the effective coupling constant for the ZZ interaction. In the center and right figures, the upper figure shows the schematic energy level diagram. The curved solid arrows indicate the relative movement of ω_{02} with respect to ω_{11} . The lower figure shows the same movement as a function of time. The dashed arrow for CE indicates the population swapping to $|02\rangle$ and then back to $|11\rangle$ at the rate $\sqrt{2}J/\pi$ when $\omega_{11} = \omega_{02}$. Note that, for adiabatic excursion, $|02\rangle$ does not meet $|11\rangle$ to satisfy adiabaticity. (c) Implementation of the iSWAP gate via coherent exchange. The upper figure shows the schematic energy level diagram. The curved solid arrow indicates the relative movement of ω_{01} with respect to ω_{10} . The lower figure shows the same movement as a function of time. The dashed arrows present the two qubits exchanging their energy at the rate J/π when $\omega_{10} = \omega_{01}$. (d) Implementation of the iSWAP and bSWAP gates via parametric coupling. Here, neither qubit needs to be tuned. The gate operation is performed by applying a microwave to the tunable coupler with the frequency $|\omega_{q1} - \omega_{q2}|$ (iSWAP) or $\omega_{q1} + \omega_{q2}$ (bSWAP).

ment the bSWAP gate:^{106,115}

$$\hat{U}_{\text{bSWAP}} = \begin{pmatrix} 0 & 0 & 0 & -i \\ 0 & 1 & 0 & 0 \\ 0 & 0 & 1 & 0 \\ -i & 0 & 0 & 0 \end{pmatrix}. \quad (74)$$

In this case, Eq. (46) becomes

$$\hat{\mathcal{H}}_{2q}^{\text{rot}} = \frac{\hbar J_m}{2} (\hat{\sigma}_+^{(1)} \hat{\sigma}_+^{(2)} + \hat{\sigma}_-^{(1)} \hat{\sigma}_-^{(2)}). \quad (75)$$

The propagator based on this Hamiltonian is

$$\hat{U}(\tau) = \begin{pmatrix} \cos(J_m \tau/2) & 0 & 0 & -i \sin(J_m \tau/2) \\ 0 & 1 & 0 & 0 \\ 0 & 0 & 1 & 0 \\ -i \sin(J_m \tau/2) & 0 & 0 & \cos(J_m \tau/2) \end{pmatrix}. \quad (76)$$

It is clear that $J_m \tau = \pi$ implements the bSWAP gate.

3. CZ: Adiabatic Excursion

Any two-qubit gate based on the transverse interaction has to be performed at least twice to implement the CNOT gate.¹¹² Since the CNOT gate is the essential gate for quantum error correction (see Sec. VII), a more efficient implementation of the CNOT gate is desired. For this, we need a non-transverse qubit-qubit interaction. It was soon realized that we have an effective ZZ interaction that comes from the transverse interaction associated with higher excitation levels.¹¹⁶ This interaction allows us to implement the controlled-Z (CZ) gate, which is identical to the CNOT gate up to single-qubit

rotations:

$$\begin{array}{c} \bullet \\ | \\ \oplus \end{array} = \begin{array}{c} \bullet \\ | \\ \boxed{H} \end{array} \begin{array}{c} \bullet \\ | \\ \boxed{H} \end{array}, \quad (77)$$

where

$$\hat{U}_{CZ} = \begin{pmatrix} 1 & 0 & 0 & 0 \\ 0 & 1 & 0 & 0 \\ 0 & 0 & 1 & 0 \\ 0 & 0 & 0 & -1 \end{pmatrix} \equiv \begin{array}{c} \bullet \\ | \\ \bullet \end{array}. \quad (78)$$

Equation (78) is read “apply the Z gate to qubit 2 if the state of qubit 1 is $|1\rangle$.”

As we explained in Sec. VB3, if J is static and $\omega_{q1} \neq \omega_{q2}$, the contribution from the transverse qubit-qubit interaction to the dynamics is small [Eq. (46)]. In this case, the propagator has the form

$$\hat{U} = \begin{pmatrix} 1 & 0 & 0 & 0 \\ 0 & e^{i\theta_{01}} & 0 & 0 \\ 0 & 0 & e^{i\theta_{10}} & 0 \\ 0 & 0 & 0 & e^{i\theta_{11}} \end{pmatrix}, \quad (79)$$

where θ_{ij} is the phase of the state $|ij\rangle$ acquired throughout the evolution for the time interval τ : $\theta_{ij} = \int_0^\tau \omega_{ij}(t)dt$. Therefore, to implement the CZ gate, we need to have $\theta_{11} - \theta_{10} - \theta_{01} = \pi$.

If we consider the computational subspace only, the difficulty in implementing the CZ gate is that ω_{11} is always the same as $\omega_{10} + \omega_{01}$; thus, $\theta_{11} = \theta_{10} + \theta_{01}$. This is why we need a ZZ interaction. The crucial observation is that ω_{11} deviates from $\omega_{10} + \omega_{01}$ because of the anticrossing between the $|11\rangle$ and $|02\rangle$ levels [left figure in Fig. 16(b)]. This gives an effective ZZ interaction whose strength ζ is $\omega_{10} + \omega_{01} - \omega_{11}$. As shown in the left figure in Fig. 16(b), ζ increases rapidly as the energy levels of $|02\rangle$ and $|11\rangle$ become closer, suggesting that varying the flux bias can be used to tune ζ by orders of magnitude.¹¹⁶

Now we have the ZZ interaction. Note that, in Eq. (78), the population of each state must remain the same. One way to implement the CZ gate is to tune the energy levels adiabatically. In addition, another condition to make the CZ gate operation feasible is negative anharmonicity such that the $|11\rangle$ - $|02\rangle$ anticrossing appears earlier than the $|10\rangle$ - $|01\rangle$ anticrossing. Otherwise, the transition between $|10\rangle$ and $|01\rangle$ will be activated during the gate operation, resulting in an unwanted population change. Therefore, the most suitable qubit for the CZ gate operation is a transmon and its variants.

Implementing a high-fidelity and fast CZ gate is then reduced to finding an optimal trajectory satisfying $\int_0^\tau \zeta(t)dt = \pi$. In general, the flux must be ramped up fast at the beginning to reduce the gate time. Near the anticrossing, the flux sweep is relatively slow to satisfy adiabaticity and acquire the phase we need [center figure in Fig. 16(b)]. It was found that the Slepian shape is close to the optimal trajectory.¹¹⁷

4. CZ: Coherent Exchange and Parametric Coupling

The CZ gate can also be implemented by coherent exchange between $|11\rangle$ and $|02\rangle$ to acquire the phase factor [right figure in Fig. 16(b)].^{67,105} Regarding coherent exchange, when $\omega_{11} = \omega_{02}$, we can construct a propagator similar to Eq. (70):

$$\hat{U}(\tau) = \begin{array}{c} \langle 00| \quad \langle 01| \quad \langle 10| \quad \langle 11| \quad \langle 02| \quad \langle 20| \\ \begin{array}{l} |00\rangle \\ |01\rangle \\ |10\rangle \\ |11\rangle \\ |02\rangle \\ |20\rangle \end{array} \end{array} \begin{pmatrix} 1 & 0 & 0 & 0 & 0 & 0 \\ 0 & 1 & 0 & 0 & 0 & 0 \\ 0 & 0 & 1 & 0 & 0 & 0 \\ 0 & 0 & 0 & \cos(\sqrt{2}J\tau) & -i\sin(\sqrt{2}J\tau) & 0 \\ 0 & 0 & 0 & -i\sin(\sqrt{2}J\tau) & \cos(\sqrt{2}J\tau) & 0 \\ 0 & 0 & 0 & 0 & 0 & 1 \end{pmatrix}. \quad (80)$$

One difference from Eq. (70) is that the coupling constant is $\sqrt{2}J$ instead of J . In general, the coupling constant for the transverse interaction between $|n_1, n_2 - 1\rangle$ and $|n_1 - 1, n_2\rangle$ is $J\sqrt{n_1 n_2}$ because $\hat{a}|n\rangle = \sqrt{n}|n-1\rangle$ and $\hat{a}^\dagger|n\rangle = \sqrt{n+1}|n+1\rangle$. What we want is $\cos(\sqrt{2}J\tau) = -1$; thus, $\sqrt{2}J\tau = \pi$ implements the CZ gate.

Parametric coupling can also be used.¹⁰⁹ Since we do not need to tune the qubit frequencies, negative anharmonicity is not required. Moreover, we can use the coupling between $|11\rangle$ and either $|02\rangle$ or $|20\rangle$.

5. CR: All Microwave Control

All implementations of two-qubit gates discussed thus far require some tunability of the qubit frequency or qubit-qubit coupling. However, the phase coherence is so delicate that any control line potentially degrades T_2 . This motivates the development of two-qubit gates purely driven by microwave activation. Among them, the cross-resonance (CR) gate is the most widely used one.

The CR gate basically excites one qubit (target qubit) through the other qubit (control qubit). Hence, it is similar to a single-qubit gate, and its classical analogy is Fig. 9(c). The difference is that, instead of a harmonic oscillator (resonator), a nonlinear oscillator (qubit) is used as a control oscillator.¹²⁰ Because of the nonlinearity, the result of the gate operation depends on the state of the control qubit, resulting in a two-qubit gate.

In the following, we repeat the calculations we made in Sec. VIC with slight modifications for a two-qubit system instead of a qubit-resonator system. We make three assumptions. First, $J \ll \Delta_{qq}$, where $\Delta_{qq} \equiv \omega_{q1} - \omega_{q2}$. This is a kind of dispersive limit. Secondly, the control qubit, which is assumed to be qubit 1, is an ideal two-level system, i.e., $\alpha_1 \gg \Delta_{qq}$, where α_1 is the anharmonicity of qubit 1. Lastly, there is no spurious cross-talk between the two qubits.

Since the first assumption is also a kind of dispersive limit, we can apply the Schrieffer–Wolff transformation,

$$\hat{U}_{\text{disp}} = \exp \left[\frac{J}{\Delta_{\text{qq}}} (\hat{\sigma}_+^{(1)} \hat{\sigma}_-^{(2)} - \hat{\sigma}_-^{(1)} \hat{\sigma}_+^{(2)}) \right], \quad (81)$$

to $\hat{\mathcal{H}}_{2\text{q}}$ in Eq. (68) as we did in Sec. VIB 1:

$$\begin{aligned} \hat{\mathcal{H}}_{2\text{q}}^{\text{disp}} &= \hat{U}_{\text{disp}} \hat{\mathcal{H}}_{2\text{q}} \hat{U}_{\text{disp}}^\dagger \\ &\approx \hbar \left(\omega_{\text{q1}} + \frac{J^2}{\Delta_{\text{qq}}} \right) \frac{\hat{\sigma}_z^{(1)}}{2} + \hbar \left(\omega_{\text{q2}} - \frac{J^2}{\Delta_{\text{qq}}} \right) \frac{\hat{\sigma}_z^{(2)}}{2} \end{aligned} \quad (82)$$

Regarding the external drive, we use a Hamiltonian similar to Eq. (61):

$$\hat{\mathcal{H}}_{\text{d}}(t) = \hbar \mathcal{E}_{\text{q}}(t) (\hat{\sigma}_+^{(1)} e^{-i\omega_{\text{d}} t} + \hat{\sigma}_-^{(1)} e^{+i\omega_{\text{d}} t}), \quad (83)$$

where \mathcal{E}_{q} and ω_{d} are the amplitude and frequency of the external drive, respectively. We apply the same Schrieffer–Wolff transformation to Eq. (83):

$$\begin{aligned} \hat{\mathcal{H}}_{\text{d}}^{\text{disp}} &= \hat{U}_{\text{disp}} \hat{\mathcal{H}}_{\text{d}}(t) \hat{U}_{\text{disp}}^\dagger \\ &\approx \hbar \mathcal{E}_{\text{q}}(t) (\hat{\sigma}_+^{(1)} e^{-i\omega_{\text{d}} t} + \hat{\sigma}_-^{(1)} e^{+i\omega_{\text{d}} t}) \\ &\quad + \frac{\hbar \mathcal{E}_{\text{q}}(t) J}{\Delta_{\text{qq}}} \hat{\sigma}_z^{(1)} (\hat{\sigma}_+^{(2)} e^{-i\omega_{\text{d}} t} + \hat{\sigma}_-^{(2)} e^{+i\omega_{\text{d}} t}). \end{aligned} \quad (84)$$

In Eq. (84), we can see that the second line corresponds to driving qubit 2.

Next, we combine Eqs. (82) and (84) to obtain the full two-qubit Hamiltonian $\hat{\mathcal{H}}_{2\text{q}}^{\text{full}}$:

$$\hat{\mathcal{H}}_{2\text{q}}^{\text{full}} \equiv \hat{\mathcal{H}}_{2\text{q}}^{\text{disp}} + \hat{\mathcal{H}}_{\text{d}}^{\text{disp}}. \quad (85)$$

Now, we move to the rotating frame whose Hamiltonian is defined by

$$\hat{\mathcal{H}}_0 = \hbar \omega_{\text{d}} \left(\frac{\hat{\sigma}_z^{(1)}}{2} + \frac{\hat{\sigma}_z^{(2)}}{2} \right). \quad (86)$$

The final two-qubit Hamiltonian in the rotating frame $\hat{\mathcal{H}}_{2\text{q}}^{\text{rot}}$ can be obtained by the unitary transformation:

$$\begin{aligned} \hat{\mathcal{H}}_{2\text{q}}^{\text{rot}} &= e^{i\hat{\mathcal{H}}_0 t/\hbar} (\hat{\mathcal{H}}_{2\text{q}}^{\text{full}} - \hat{\mathcal{H}}_0) e^{-i\hat{\mathcal{H}}_0 t/\hbar} \\ &= \hbar \left(\omega_{\text{q1}} + \frac{J^2}{\Delta_{\text{qq}}} - \omega_{\text{d}} \right) \frac{\hat{\sigma}_z^{(1)}}{2} + \hbar \mathcal{E}_{\text{q}}(t) \hat{\sigma}_x^{(1)} \\ &\quad + \hbar \left(\omega_{\text{q2}} - \frac{J^2}{\Delta_{\text{qq}}} - \omega_{\text{d}} \right) \frac{\hat{\sigma}_z^{(2)}}{2} + \hbar \Omega_{\text{CR}}(t) \hat{\sigma}_z^{(1)} \hat{\sigma}_x^{(2)}, \end{aligned} \quad (87)$$

where $\Omega_{\text{CR}} \equiv \mathcal{E}_{\text{q}} J / \Delta_{\text{qq}}$. For these transformations, we use the formulas in Table V.

If we set $\omega_{\text{d}} = \omega_{\text{q2}} - J^2 / \Delta_{\text{qq}}$, the only term contributing to the two-qubit gate operation is the last term in

Eq. (87), which we denote as $\hat{\mathcal{H}}_{\text{d}}^{\text{rot}}$:

$$\hat{\mathcal{H}}_{\text{d}}^{\text{rot}} = \hbar \Omega_{\text{CR}} \hat{\sigma}_z^{(1)} \hat{\sigma}_x^{(2)}. \quad (88)$$

Thus, the propagator is

$$\begin{aligned} \hat{U}(\tau) &= e^{-i\hat{\mathcal{H}}_{\text{d}}^{\text{rot}} \tau / \hbar} \\ &= \begin{pmatrix} \cos(\Omega_{\text{CR}} \tau) & -i \sin(\Omega_{\text{CR}} \tau) & 0 & 0 \\ -i \sin(\Omega_{\text{CR}} \tau) & \cos(\Omega_{\text{CR}} \tau) & 0 & 0 \\ 0 & 0 & \cos(\Omega_{\text{CR}} \tau) & i \sin(\Omega_{\text{CR}} \tau) \\ 0 & 0 & i \sin(\Omega_{\text{CR}} \tau) & \cos(\Omega_{\text{CR}} \tau) \end{pmatrix}. \end{aligned} \quad (89)$$

The above matrix is read as “rotate the target qubit state $+ \Omega_{\text{CR}} \tau$ about the x -axis if the control qubit state is $|0\rangle$, and rotate the target qubit state $- \Omega_{\text{CR}} \tau$ about the x -axis if the control qubit state is $|1\rangle$.”

Note that the CR gate is related to the CNOT gate by only two single-qubit rotations:¹¹⁸

$$\begin{array}{c} \bullet \\ | \\ \oplus \end{array} = \begin{array}{c} \boxed{R_z(-\frac{\pi}{2})} \quad \bullet \\ | \\ \boxed{\text{CR}(\frac{\pi}{2})} \quad \boxed{R_x(-\frac{\pi}{2})} \end{array}, \quad (90)$$

where

$$\begin{array}{c} \bullet \\ | \\ \boxed{\text{CR}(\frac{\pi}{2})} \end{array} = \hat{U} \left(\Omega_{\text{CR}} \tau = \frac{\pi}{2} \right) = \frac{1}{\sqrt{2}} \begin{pmatrix} 1 & -i & 0 & 0 \\ -i & 1 & 0 & 0 \\ 0 & 0 & 1 & i \\ 0 & 0 & i & 1 \end{pmatrix}. \quad (91)$$

For a qubit such as a transmon, the assumption for an ideal two-level system is not valid. In this case, we have to consider higher level contributions. Since the calculation needs some labor, we just quote the result:^{119,120}

$$\hat{\mathcal{H}}_{\text{d}}^{\text{rot}} = \frac{\mathcal{E}_{\text{q}} J}{\Delta_{\text{qq}} + \alpha_1} \hat{\sigma}_x^{(2)} + \frac{\alpha_1}{\Delta_{\text{qq}} + \alpha_1} \Omega_{\text{CR}} \hat{\sigma}_z^{(1)} \hat{\sigma}_x^{(2)}. \quad (92)$$

Note that Eq. (92) becomes Eq. (88) in the $\alpha_1 \rightarrow \infty$ limit (ideal two-level system). In the $\alpha_1 \rightarrow 0$ limit (bosonic system), only the single-qubit drive term (the first term) survives—Eq. (92) becomes Eq. (66). Equation (92) suggests that, if $\Delta_{\text{qq}} \gg \alpha_1$, the CR drive amplitude is greatly reduced. Therefore, to have a reliable CR drive amplitude, Δ_{qq} must be comparable to α_1 ; if Δ_{qq} is too small, the states of the two qubits are hybridized such that the single-qubit gate operation will be nontrivial. In the actual operation, the unwanted single-qubit drive term in Eq. (92) can be canceled out by applying an additional pulse.¹¹¹

One might wonder about the fate of the effective ZZ interaction, which was a hero for the CZ gate (Sec. VID 3). Now, it is a villain that degrades the fidelity of the CR gate. This interaction can be canceled out by a refocusing technique,¹¹¹ which will be explained in Sec. IX C.

E. Initialization

After computation, qubits should be initialized for the next computation. However, condition 3 in Sec. III A and fast initialization seem to be contradictory. Here, we introduce two categories of qubit initialization and their working principles.

1. Entropy Dumping

This method is to pump entropy of the target system to another system, which we call the pumping system, interacting with the target system. Here, the required condition is that the relaxation of the pumping system has to be much faster than that of the target system. This idea has been used in magnetic resonance for a long time, with the name “Dynamic Nuclear Polarization (DNP).”^{121,122} In DNP, the target system is a nuclear spin; the pumping system is an electron spin; and their interaction is mediated by the hyperfine interaction.

In a superconducting circuit, the target system is a superconducting qubit and the pumping system is usually the readout resonator because the qubit must be isolated as much as possible to maintain the coherence, while the resonator needs to be strongly coupled to the microwave feedline for fast readout. The strategy is to find an efficient and controllable energy transfer path to the environment.

One path is from the qubit state $|e\rangle$ to the resonator state $|1\rangle$ [Fig. 17(a)].^{56,85} For this, the Purcell effect (Sec. VIB 1) is used. By using a frequency-tunable qubit, we can tune ω_q to ω_r to speed up the qubit relaxation process. Once the energy is emitted from the qubit to the resonator, the energy is quickly dissipated to the environment.

An all-microwave option is also available.^{123,124} In this case, the higher excitation level $|f\rangle$ is inserted into the $|e\rangle$ - $|1\rangle$ path [Fig. 17(b)]. The transitions between the steps are induced by microwave drives. Hence, this method is useful for a transmon with the fixed qubit frequency. Note that we cannot induce a direct transition between $|e0\rangle$ and $|g1\rangle$ because this transition is forbidden when the qubit-resonator interaction is Jaynes-Cummings-type [Eq. (40)].¹²⁵

These two methods can be understood using mechanical analogues shown in Fig. 17(a) and (b).

2. Measurement-Based Initialization

This is a completely different initialization method based on the QND measurement mentioned in Sec. VIB 1 and the measurement postulate, which states that a measurement of an observable acting on a quantum state destroys the phase coherence and forces the state to collapse into one of the eigenstates of the observable.^{8,9} If a measurement is QND-type and its outcome is $|0\rangle$, then the

qubit is initialized. If the outcome is $|1\rangle$, we simply apply a π -pulse to flip the qubit state. The flow chart for this procedure is shown in Fig. 17(c). This method is often called measurement-based initialization.^{126–128}

One technical difficulty is that this method heavily relies on high-fidelity projective measurement and fast feedback. It can suffer from latency due to the classical data processing and the pulse generation and injection.

Note that, in this method, we reduce the entropy of the qubit by extracting information about its state. This suggests that information processing and thermodynamics are connected intrinsically. One of the most famous examples showing this connection is Maxwell’s demon that is recently implemented in superconducting qubit systems.^{129–131}

VII. QUANTUM ERROR CORRECTION

A. Introduction

Noise in real physical systems, both classical and quantum, cannot be eliminated completely. As quantum algorithms of scientific and/or commercial use consist of many qubits and time-steps, error correction schemes are essential for reliable quantum computation at scale. The goal of Quantum Error Correction (QEC) is to generate an error-free logical qubit, i.e., two selected quantum states, out of the large Hilbert space of a system composed of multiple quantum systems. This introduces redundancy that can be used to both detect and correct physical errors.

Classical error correction generally can introduce redundancy by duplicating bits multiple times and then errors can be detected and corrected by comparing copies together. However, in QEC, the use of redundancy is different and much more difficult to achieve because of the following reasons. Firstly, the no-cloning theorem^{10,13} prevents this type of error-correction in quantum information as arbitrary quantum states cannot be copied. Secondly, direct measurement of quantum states is not possible as it will collapse the qubit state (measurement postulate in Sec. VIE 2). Hence, measurements that are used to detect actual errors have to be performed in an indirect way. Finally, besides the bit flip error ($|0\rangle \rightarrow |1\rangle$ or $|1\rangle \rightarrow |0\rangle$) which is the standard model for classical information, quantum information can experience a second type of the error, called the phase flip error ($\alpha|0\rangle + \beta|1\rangle \rightarrow \alpha|0\rangle - \beta|1\rangle$). Consequently, a quantum error correction code must be able to simultaneously correct for both bit flips and phase flips.

As a quantum algorithm creates complex entangled states between the constituent qubits, we require a technique that can detect individual errors on any physical qubits *without* extracting any information regarding the computational state of the computing system. Parity measurement that measures bit/phase parity of neighboring qubits is such a technique. For this, additional qubits,

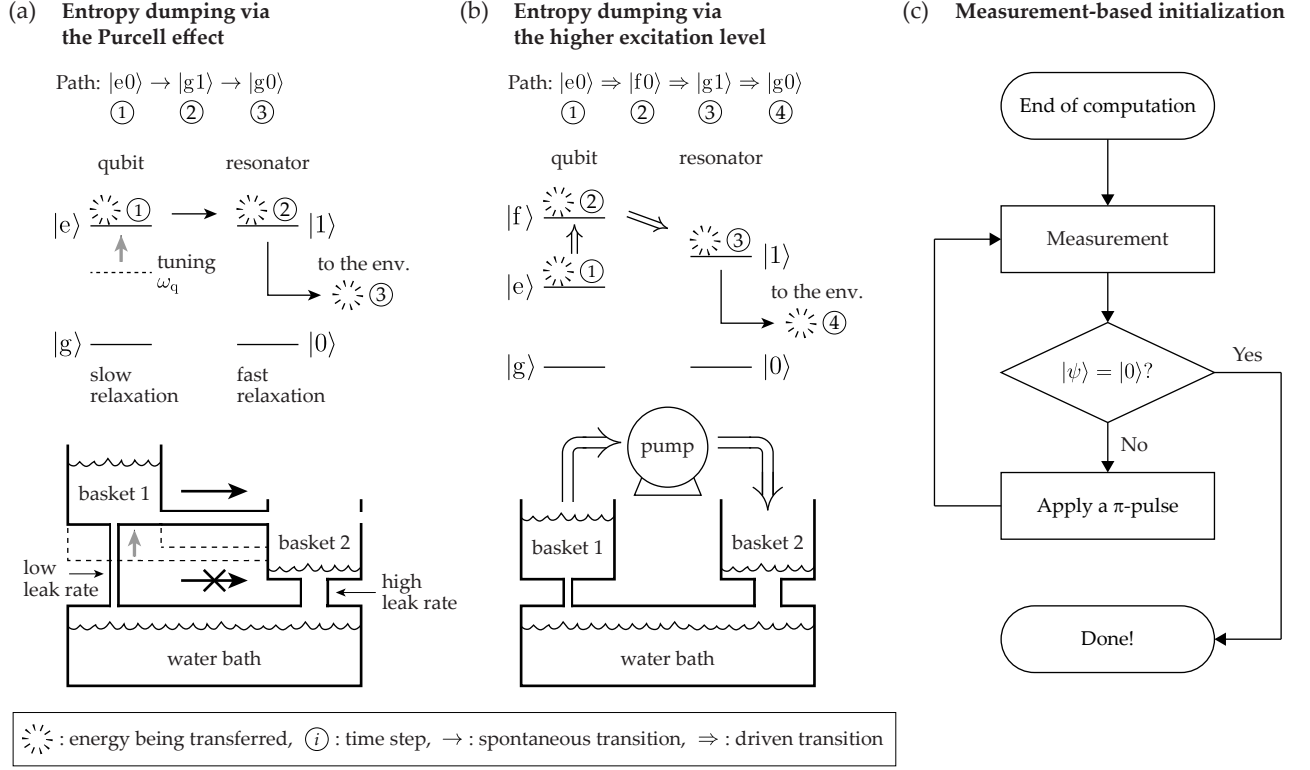


FIG. 17. Qubit initialization methods. (a) and (b) Entropy-dumping-based qubit initialization via the Purcell effect (a) and via the higher excitation level $|f\rangle$ (b). The basic strategies for both methods are the same: transfer the energy in the qubit to a resonator whose relaxation process is significantly faster than that of the qubit. The difference is that, in (a), the qubit state is tuned to satisfy $\omega_q = \omega_r$, such that the energy is transferred directly from qubit state $|e\rangle$ to resonator state $|1\rangle$ via the Purcell effect, while in (b), all energy levels are fixed and the energy is transferred through $|f\rangle$ by our microwave drives. The diagram named “Path” shows the state of the qubit-resonator system during the initialization process. Below this, the energy levels of the qubit and resonator are shown. The lower figures show mechanical analogies. Baskets 1 and 2 correspond to the qubit and resonator, respectively. Water in each basket corresponds to the entropy of each system. In (a), the vertical position of the pipe connecting the two baskets must be matched to the position of the holes on the side of basket 2 to yield the water flow. This represents the condition for the Purcell effect, $\omega_q = \omega_r$. The dashed boundary represents the moment at which this condition is not satisfied. In (b), the pump represents our active microwave radiation to the system to activate the transitions $|e0\rangle \leftrightarrow |f0\rangle$ and $|f0\rangle \leftrightarrow |g1\rangle$. (c) Flow chart describing the measurement-based initialization.

which are not used for actual computation, are introduced. These are commonly referred to as ancilla qubits or syndrome qubits. Syndrome qubits are entangled with encoded qubits, often called data qubits, within a logical qubit and are used to extract information only related to physical errors that may have occurred on individual data qubits. These syndrome qubits are then measured, generating classical information called the error syndrome. This syndrome extraction procedure is specifically designed to avoid direct measurement of the computational state of any qubit and hence preserves the computation during the error-correction process. Multiple syndrome measurements of the data qubit are taken and this classical information is decoded. This decoding procedure determines the most likely physical errors that resulted in the specific set of syndrome measurements that were observed.

Since we have to detect errors without knowing any

information about the qubit state, to define a state as an eigenstate of a certain operator in the Heisenberg representation is more convenient than to write the state itself. A formalism based on this idea is stabilizer formalism.^{139,140} As it will be shown in the following, the stabilizer formalism describes our action for error detection and logical state construction in a unified manner.

A stabilizer set is a set of commuting multiqubit operators, made up of tensor products of Pauli- X , Y , and Z operators. These multiqubit operators are commonly known as stabilizer operators or simply stabilizers. By using multiqubit projective measurement, we can force an arbitrary quantum state into simultaneous eigenstates of these stabilizers. One consequence is that, if we repeat these projective measurements in the absence of errors, we will repeatedly measure the same eigenvalue and project the quantum state into the same eigenstate; this is why these operators are called stabilizer operators.

Note that the projective measurement on each stabilizer is actually parity measurement and its outcome is an error syndrome. Physical errors cause eigenvalues to flip between $+1$ and -1 , depending on if the physical errors commute or anti-commute with stabilizers. Bit flip errors will anti-commute with stabilizers made up of Pauli- Y or Z operators and phase flip errors will anti-commute with stabilizers made up of Pauli- X and Y operators, allowing for the correction of both types of errors.

Another consequence is that the size of the stabilizer set determines the size of the restricted subspace of states that satisfy the eigen-conditions, thus defining a logical qubit. An N -qubit state is spanned by 2^N possible basis states, where a single qubit is spanned by two ($|0\rangle$ and $|1\rangle$). Consequently, we say that there are N degrees of freedom for an N -qubit state. Taking N physical qubits and encoding them into a single logical qubit requires us to fix $N - 1$ degrees of freedom with the one left over to represent the logical qubit. This is done by requiring the multiqubit state that defines the logical qubit to be in definite eigenstates of stabilizers whose eigenvalue is $+1$. The logical qubit states, $|0\rangle_L$ and $|1\rangle_L$, both satisfy the eigen-conditions defined by these stabilizers.

In a real system, physical errors do not occur as discrete bit and phase flips, instead either coherent (such as imprecise control errors) or incoherent errors (such as thermalization or dephasing) act to perturb a qubit state in a continuous manner. However, measuring the eigenvalues of the stabilizer operators acts to discretize this noise, which translates the continuous nature of the noise into a probability of detecting a discrete error through the measurement of the syndrome qubit. An arbitrary error operator can be written as a linear combination of X errors, Z errors, and Y errors. Therefore, correcting all three is sufficient to correct for all possible errors on a single physical qubit. Here, as Y error can be decomposed into Z and X errors, $\hat{Y} = i\hat{Z}\hat{X}$, correcting for Z and X errors will together correct for any Y errors. Z and X errors are conventionally referred to as bit flip and phase flip errors, respectively.

There are a plethora of QEC codes in existence and many of them have been studied extensively. Amongst these, the surface code remains the most suitable scheme for solid-state qubit systems.^{132,133} One of the advantages of the surface code is that it requires each qubit to be coupled to at most, four nearest neighboring qubits. This allows us to arrange qubits into two-dimensional lattice (Fig. 18). A single square patch of qubits defines a single, logically encoded qubit. This patch is generally parameterized by the number of physical qubits along an edge, which is also related to the distance, d , of the underlying quantum code—the distance of a quantum code is the minimum number of physical errors needed to induce a logical error. Another advantage is the fault-tolerant threshold of the surface code. The fault-tolerant threshold is the maximum physical error rate that the code can correct. For the surface code, the fault-tolerant threshold is approximately one-percent including errors related to

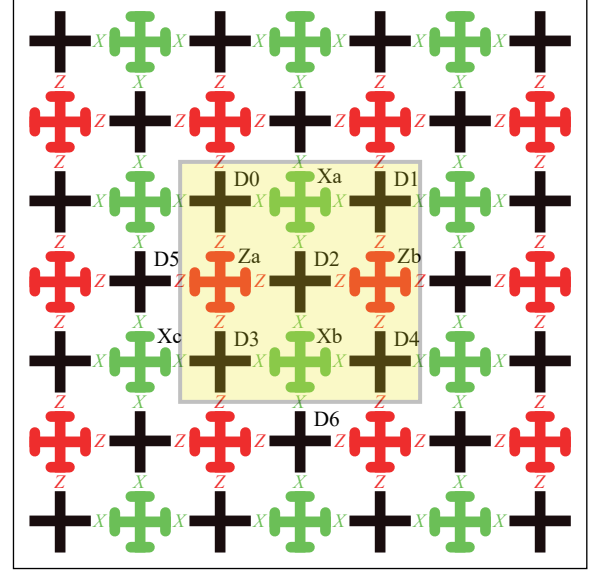


FIG. 18. Arrangement of physical qubits in the surface code with $d = 4$, where d is the number of data qubits along the horizontal or vertical edge at the lattice boundary, which is represented by black solid lines. The black crosses are data qubits, the red crosses are Z syndrome qubits, and the green crosses are X syndrome qubits. The data and syndrome qubits are physically the same; only their functions are different. All qubits in the lattice boundary form a single logical qubit. In Sec. VII B 2, we will reduce the lattice boundary to the yellow square to give a simple example of logical qubit construction.

state readout and all gate operations. This error threshold is one of the highest of any error correction scheme to date and remains the highest of a code that is compatible with the architectural constraints of current quantum computing hardware. However, we emphasize that fault-tolerant thresholds vary significantly, depending on the actual QEC code that is utilized.

In this tutorial, we explain how to construct a logical qubit, how to detect and correct errors, and how to perform gate operations on a logical qubit in the context of the surface code. Interested readers are referred Ref. 10, 13, 134, and 135 for introductions to QEC and Refs. 136–138 for comprehensive reviews.

B. Surface Code

1. Definition

The surface code is defined over a two-dimensional lattice of physical qubits that allow for nearest neighbor interactions. For a distance d code, the size of the lattice is $(2d - 1) \times (2d - 1)$ physical qubits. Of the total $4d^2 - 4d + 1$ physical qubits in the lattice, approximately half $(2d^2 - 2d + 1)$ are data qubits and the rest of the

physical qubits are syndrome qubits. It is sufficient to detect $\lceil (d-1)/2 \rceil$ single-qubit errors, i.e., errors associated with a single data qubit, or correct $\lfloor (d-1)/2 \rfloor$ single-qubit errors. Thus, the smallest d required to correct any single-qubit error is 3. Figure 18 illustrates for a $d = 4$ surface code, which can detect 2 single-qubit errors and correct 1 single-qubit error.

2. Logical Qubit Construction

In this subsection, we give an example for constructing a logical qubit with physical data qubits in the yellow square of Fig. 18. Although the yellowed lattice is too small ($d = 2$) to specify the position and the type of an arbitrary single-qubit error uniquely (see Sec. VII B 1), we use this yellowed lattice to give the simplest example for logical qubit construction and logical gate operation. We first write the logical qubit in the state vector notation. Then we will re-express the same logical qubit using the stabilizer formalism. In the state vector notation, the logical qubit states are written as

$$\begin{aligned} |0\rangle_L &= \frac{1}{2} (|0000\rangle + |0011\rangle + |1101\rangle + |1110\rangle), \\ |1\rangle_L &= \frac{1}{2} (|1001\rangle + |1010\rangle + |0100\rangle + |0111\rangle), \end{aligned} \quad (93)$$

where each ket represents $|\psi_{D0}\psi_{D1}\psi_{D2}\psi_{D3}\psi_{D4}\rangle$. In general, the logical qubit state during computations is $|\psi\rangle_L = \alpha|0\rangle_L + \beta|1\rangle_L$, where α and β are complex numbers, and $|\alpha|^2 + |\beta|^2 = 1$.

In the stabilizer formalism, the same logical states are defined by

$$|\psi\rangle = \hat{S}|\psi\rangle. \quad (94)$$

In the literature, Eq. (94) is often read as “ $|\psi\rangle$ is stabilized by the operator set \hat{S} .” Here, $\{\hat{S}\}$ is a stabilizer set in which stabilizers are given by

$$\begin{aligned} \hat{S}_0 &= \hat{X}_{D0}\hat{X}_{D1}\hat{X}_{D2}\hat{I}_{D3}\hat{I}_{D4}, \\ \hat{S}_1 &= \hat{I}_{D0}\hat{I}_{D1}\hat{X}_{D2}\hat{X}_{D3}\hat{X}_{D4}, \\ \hat{S}_2 &= \hat{Z}_{D0}\hat{I}_{D1}\hat{Z}_{D2}\hat{Z}_{D3}\hat{I}_{D4}, \\ \hat{S}_3 &= \hat{I}_{D0}\hat{Z}_{D1}\hat{Z}_{D2}\hat{I}_{D3}\hat{Z}_{D4}, \end{aligned} \quad (95)$$

where \hat{X}_i and \hat{Z}_i are the Pauli matrices applied to data qubit i . Here, \hat{S}_0 and \hat{S}_1 are X stabilizers, and \hat{S}_2 and \hat{S}_3 are Z stabilizers. All these stabilizers commute with each other and satisfy Eq. (94). Since both $|0\rangle_L$ and $|1\rangle_L$ are eigenstates of this stabilizer set with the same eigenvalue, $+1$, repeatedly measuring these operators preserves the logical qubit states without destroying the phase coherence between them.

There are other methods for constructing a logical qubit when logical qubits are defined using defects in a qubit lattice. But these methods are out of the scope of

this tutorial. The standard introduction to this topic is Ref. 133.

3. Error Detection and Correction

Error detection requires repeated parity measurements of the stabilizers of the surface code. The syndrome qubits are used for this. These syndrome qubits are the only qubits measured during the error detection (syndrome extraction) process to avoid destruction of the logical information stored.

As shown in Fig. 18, there are two types of syndrome qubits, namely, Z syndrome qubits, which are measured in the Z basis, and X syndrome qubits, which are measured in the X basis. These syndrome qubits are used to measure the eigenvalue of Z and X stabilizers of the surface code, respectively. Having these two types of syndrome qubits allows us to detect both bit and phase flip errors as physical bit flip errors will be detected by the measurement of Z stabilizers and physical phase flip errors will be detected by the measurement of X stabilizers.

The following quantum circuits show one surface code cycle for the Z_a and the X_b syndrome qubits.

$$\begin{array}{l} D0 \ |\psi_{D0}\rangle \\ D2 \ |\psi_{D2}\rangle \\ D3 \ |\psi_{D3}\rangle \\ D5 \ |\psi_{D5}\rangle \\ Z_a \ |0\rangle \end{array} \begin{array}{c} \bullet \\ \bullet \\ \bullet \\ \bullet \\ \oplus \oplus \oplus \oplus \end{array} \begin{array}{c} \text{---} \\ \text{---} \\ \text{---} \\ \text{---} \\ \text{---} \end{array} \quad (96)$$

$$\begin{array}{l} D2 \ |\psi_{D2}\rangle \\ D3 \ |\psi_{D3}\rangle \\ D4 \ |\psi_{D4}\rangle \\ D6 \ |\psi_{D6}\rangle \\ X_b \ |0\rangle \end{array} \begin{array}{c} \oplus \\ \oplus \\ \oplus \\ \oplus \\ \text{---} \end{array} \begin{array}{c} \text{---} \\ \text{---} \\ \text{---} \\ \text{---} \\ \text{---} \end{array} \quad (97)$$

Syndrome qubit measurements in these circuits occur in the computational (Z) basis. Equation (97) can be rewritten as

$$\begin{array}{l} D2 \ |\psi_{D2}\rangle \\ D3 \ |\psi_{D3}\rangle \\ D4 \ |\psi_{D4}\rangle \\ D6 \ |\psi_{D6}\rangle \\ X_b \ |0\rangle \end{array} \begin{array}{c} \text{---} \text{---} \text{---} \text{---} \\ \text{---} \text{---} \text{---} \text{---} \\ \text{---} \text{---} \text{---} \text{---} \\ \text{---} \text{---} \text{---} \text{---} \\ \oplus \oplus \oplus \oplus \end{array} \begin{array}{c} \text{---} \\ \text{---} \\ \text{---} \\ \text{---} \\ \text{---} \end{array} \quad (98)$$

based on the following identity,

$$\begin{array}{c} \bullet \\ \oplus \end{array} = \begin{array}{c} \text{---} \text{---} \text{---} \text{---} \\ \text{---} \text{---} \text{---} \text{---} \end{array} \quad (99)$$

By using the H gates, the CNOTs in Eq. (98) can be inverted, ensuring that both circuits have the ancilla qubit

as target for all CNOTs. Of course, for actual implementation, Eq. (97) is more economical than Eq. (98) because of the reduced number of gates.

The quantum circuits [Eqs. (96) and (97)], called parity check circuits, are designed to infer the bit and phase parities of neighboring data qubits by measuring the eigenvalue of specific four qubit Pauli operators. This not only extracts the eigenvalue of the relevant Pauli operator but also projects the four data qubits into the appropriate eigenstate. In Eq. (96), our measurement on the Za syndrome qubit forces the neighboring data qubits (D0, D2, D3, and D5) into an eigenstate of $\hat{Z}_{D0}\hat{Z}_{D2}\hat{Z}_{D3}\hat{Z}_{D5}$ (Z stabilizer). Similarly, in Eq. (97), the measurement on the Xb syndrome qubit forces the neighboring data qubits (D2, D3, D4, and D6) into an eigenstate of $\hat{X}_{D2}\hat{X}_{D3}\hat{X}_{D4}\hat{X}_{D6}$ (X stabilizer).

If the D2 qubit has a phase error, Xa and Xb syndrome qubits [Eq. (97)] return -1 as the error syndromes if there is no error in the syndrome qubits; if the D2 qubit has a bit flip error, Za and Zb syndrome qubits [Eq. (96)] return -1 . Note that the existence of both a bit flip error and a phase flip error can be detected simultaneously because $\hat{Z}_{D0}\hat{Z}_{D2}\hat{Z}_{D3}\hat{Z}_{D5}$ and $\hat{X}_{D2}\hat{X}_{D3}\hat{X}_{D4}\hat{X}_{D6}$ commute. Therefore, the parity measurement allows us to know the existence of both the bit flip and the phase flip errors without collapsing the quantum state of data qubits.

These circuits has to be performed across the entire lattice, with measurement of all X syndromes occurring simultaneously followed by simultaneous measurement of all Z syndromes. The measurement of every X and Z syndrome is referred to as an error correction cycle, which is repeated continuously as the quantum computer is in operation. Consequently, after each error correction cycle, there will be $d^2 - d$ classical bits of information (error syndromes) related to X errors and $d^2 - d$ classical bits of information related to Z errors. After multiple cycles of error-correction, all this information is then processed by a classical error-correction decoder to determine the most likely set of *actual* errors that resulted in the syndrome measurements that are observed.¹⁴³

Once the existence of an error is confirmed, the error can be corrected by applying the microwave pulse to flip phase or bit of the D2 qubit. However, in practice, we can simply record the error in a classical computer and correct measurement outcomes that are affected by the error. This is known as tracking the Pauli frame.¹⁴¹

In the above example, the position and the type (bit or phase flip) of the error were already known. However, determining the position and the type of the error from syndrome measurements are difficult because it is an inverse problem. Moreover, the error position cannot be determined uniquely for some error patterns. For example, error syndromes of Xa and Xc resulting from phase errors in D0 and D5 are identical to that from phase errors in D2 and D3. However, if the number of such an error is reasonably small, the identity of each error can be almost completely inferred by minimum-weight perfect matching algorithm.¹³³ This accuracy in using mini-

mum weight matching to identify the most likely physical errors corresponding to a measured syndrome pattern is what effectively determines the fault-tolerant threshold. If error rates are too high, or errors spread too much through the quantum circuits used in the syndrome extraction process, then decoding algorithms will not decode physical errors accurately and corrections may induce logical errors.

One interesting consequence is that initialization of a logical qubit can be considered as a kind of error correction starting from a known state, such as $|00000\rangle$. Initializing the logical qubit from this state only requires projective measurement of the X stabilizers as the state $|00000\rangle$ already satisfies the eigen-conditions of the Z stabilizers. Additionally, when starting in the $|00000\rangle$ state, we initialize into the logical $|0\rangle_L$, because again our initial state before encoding is already in the $+1$ eigenstate of the logical Z operator. Further examples can be found in Ref. 135.

Lastly, we briefly mention how we perform readout of a logical qubit. The logical readout of an error-corrected qubit ideally requires the direct measurement of all the physical qubits in an encoded block.^{133,142} To maintain correct fault-tolerant operation, all of these physical measurements on the encoded block have to take place. While it is possible to perform readout of an encoded qubit by performing a logical single qubit parity check of the X or Z operator,¹⁴² this would still require the assistance of a fully encoded ancillary qubit that would still require the physical measurement of all component qubits to perform the readout.

4. Logical Gate Operation

After encoding, computing is performed on the code using logical gates. Logical gates must preserve the symmetries enforced by the stabilizer operators, but manipulate the operators that define the logical state of the encoded qubit in the same way as operations on physical qubits do. Consequently, logical gate operators commute with all elements in the stabilizer set $\{\hat{S}\}$, but by definition are not contained in $\{\hat{S}\}$. For the surface code, for example, the logical X gate, \hat{X}_L , corresponds to applying the physical X gate to all data qubits in one of columns—not including the Z syndrome qubits. The logical Z gate is achieved by applying the physical Z gate to the all data qubits in one of rows—not including the X syndrome qubits.

Figure 19 reproduces the yellow area in Fig. 18 with the logical Z and the logical X operations. Applying $\hat{Z}_L = \hat{Z}_{D0}\hat{Z}_{D1}\hat{Z}_{D2}\hat{Z}_{D3}\hat{I}_{D4}$ and $\hat{X}_L = \hat{X}_{D0}\hat{I}_{D1}\hat{I}_{D2}\hat{X}_{D3}\hat{I}_{D4}$ to Eq. (93) helps to understand these logical operations. Note that \hat{Z}_L and \hat{X}_L commute with every stabilizers in Eq. (95) and anti-commute with each other as they must intersect on an odd number of physical qubits and physical X and Z gates anti-commute. Consequently, they

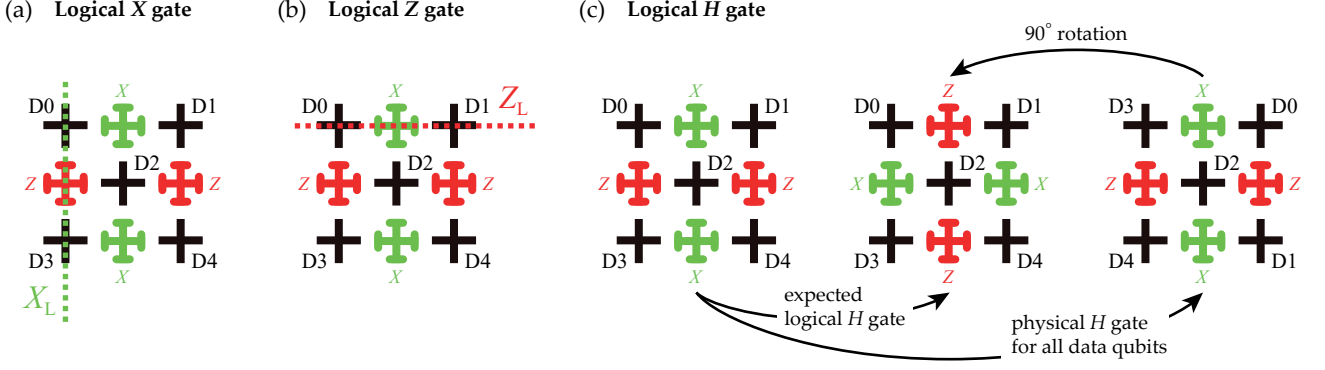


FIG. 19. Schematic images of (a) logical X gate, (b) logical Z gate, and (c) logical H gate. As in Fig. 18, the black crosses are data qubits, the red crosses are Z syndrome qubits, and the green crosses are X syndrome qubits.

form a pair of Pauli operators that have the same commutation properties as physical X and Z .

Another important single qubit gate is the Hadamard (H) gate. What we expect from the logical H gate is the following operations:

$$\begin{aligned}\hat{H}_L |0\rangle_L &= \frac{1}{\sqrt{2}}(|0\rangle_L + |1\rangle_L), \\ \hat{H}_L |1\rangle_L &= \frac{1}{\sqrt{2}}(|0\rangle_L - |1\rangle_L),\end{aligned}\quad (100)$$

i.e., the same operations as those for a physical qubit. In the Heisenberg representation, the role of the physical H gate is to exchange the physical X gate with the physical Z gate, and vice versa. In other words, a qubit that is in the $+1$ eigenstate of \hat{Z} turns into a state that is in the $+1$ eigenstate of \hat{X} because $\hat{H}^\dagger \hat{X} \hat{H} = \hat{Z}$ and $\hat{H}^\dagger \hat{Z} \hat{H} = \hat{X}$. As the logical operation must preserve the stabilizer set while interchanging the actual logical operators, the logical H needs to: (i) swap the operation of \hat{Z}_L and \hat{X}_L by flipping a vertical chain of X operators into a horizontal chain of X operators; and (ii) maintain the X and Z stabilizers in Fig. 19(c). These operations can be achieved by applying physical H gates to all data qubits (this changes all physical X operators to Z operators and visa versa), followed by 90° counterclockwise rotation of the lattice (which interchanges horizontal chains with vertical ones and ensures that the X and Z stabilizer operators stay in the same place in the lattice).

To see how this actually works, we apply the physical H gate to all data qubits composing $|0\rangle_L$ [left qubit lattice in Fig. 19(c)]:

$$\begin{aligned}\hat{H}_{D0}\hat{H}_{D1}\hat{H}_{D2}\hat{H}_{D3}\hat{H}_{D4} |0\rangle_L &= \\ \frac{1}{2\sqrt{2}} (&|00000\rangle + |01101\rangle + |11011\rangle + |10110\rangle \\ &+ |00011\rangle + |01110\rangle + |11000\rangle + |01110\rangle),\end{aligned}\quad (101)$$

which is certainly not $(|0\rangle_L + |1\rangle_L)/\sqrt{2}$. Actually, this is the right qubit lattice in Fig. 19(c), whereas what we

want is the center qubit lattice in Fig. 19(c). Thus, we have to rotate the qubit lattice 90° counterclockwise (exchanging the X stabilizers to the Z stabilizers) to obtain the logical H gate we want. This operation is equivalent to changing indices of the data qubits (i.e. performing SWAP operations): $D0$ to $D1$, $D1$ to $D4$, $D3$ to $D0$, and $D4$ to $D3$. As a result,

$$\begin{aligned}\hat{H}_L |0\rangle_L &= \\ \frac{1}{2\sqrt{2}} (&\underbrace{|00000\rangle + |00111\rangle + |11011\rangle + |11100\rangle}_{|0\rangle_L} \\ &+ \underbrace{|10010\rangle + |10101\rangle + |01001\rangle + |01110\rangle}_{|1\rangle_L}).\end{aligned}\quad (102)$$

Now, we have what we expect from the H gate. The actual operations for rotating the qubit lattice can be found in Ref. 142.

The logical two-qubit gate, such as the logical CNOT gate, is not as simple compared to the logical single-qubit gates. Implementing a non-Clifford gate, such as the T gate (see Table I for its definition), for a logical qubit is even more difficult than implementing the logical CNOT gate. The reason for this is that non-Clifford gates cannot be operated directly on the stabilizer codes in a fault-tolerant manner, i.e., ensuring errors do not cascade out of control; whereas gates in the Clifford group (gates that map Pauli operators to Pauli operators) can generally be applied directly to encoded data. It should be noted that not all stabilizer codes can enact the full Clifford group of logical operations directly. In fact, the surface code cannot enact the S gate (Table I) directly and must use other constructions.¹³³ Thus, these gates will not be covered in this tutorial. Interested readers are referred Ref. 142 for the logical CNOT gate and Refs. 144 and 145 for non-Clifford logical gates.

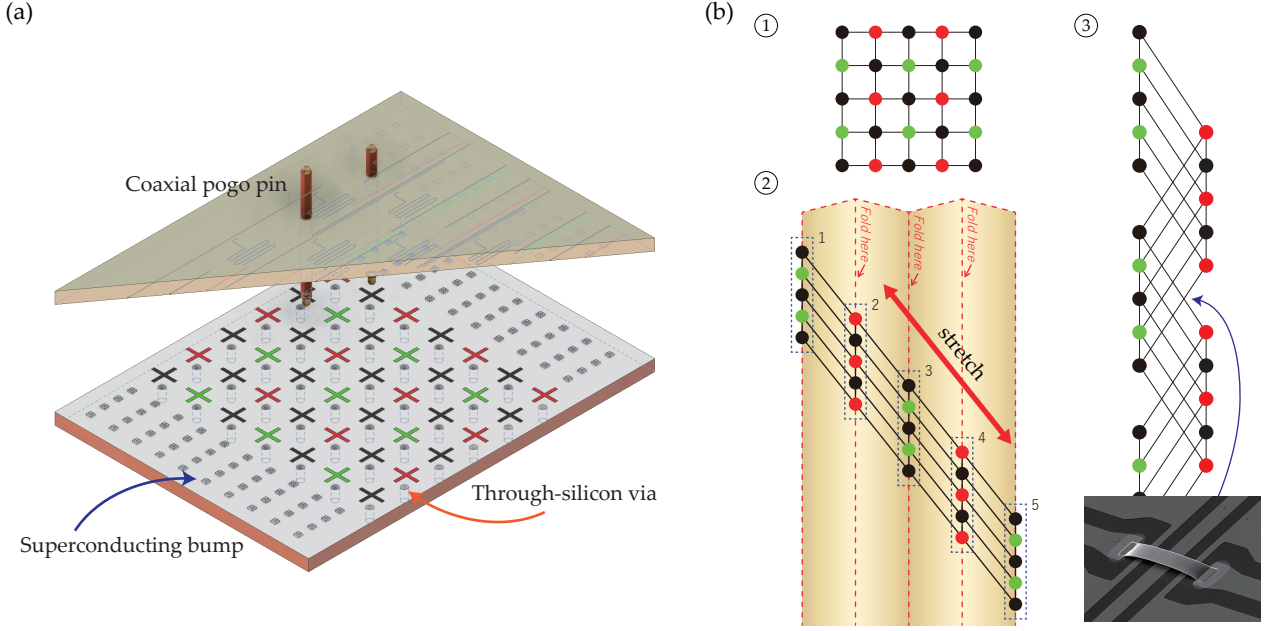


FIG. 20. (a) Schematic image of 3D wiring techniques for quantum circuit: flip-chip bonding using superconducting bumps, pogo pins, and through-silicon vias. (b) Pseudo-2D architecture. All three figures have the same lattice structure and circles represent qubits. The numbers in circles indicate how the original qubit lattice evolves to the pseudo-2D architecture. The inset shows a scanning electron microscopy image of an air bridge, which can be used at resonator intersections.

C. Proposed Device Architectures

One of the biggest problems in scaling up a superconducting qubit system is the so-called wiring problem.¹⁴⁶ The wiring problem is that the number of wires required to operate qubits increases too fast with the number of qubits because each qubit requires multiple channels such as control lines and measurement devices. In such a situation, it will be difficult to access a qubit inside a chip.

One natural idea that avoids this problem and fits well with Figs. 18 and 19 is the use of the third dimension [Fig. 20(a)].¹⁰⁷ For a classical solid-state circuit, a three-dimensional (3D) structure is made by employing a silicon oxide film as an interlayer insulator. However, this method cannot be used for quantum systems because such layers are so lossy that they can be severe decoherence channels. To get around this problem, flip-chip bonding is often used. On one chip, qubits are arranged into a square lattice; on another chip, other circuit components such as control lines and readout resonators are fabricated. Then, the two chips are combined face-to-face using superconducting bumps.^{147,148} To introduce microwaves to qubits from the top or back side of the wafer, pogo pins¹⁴⁹ and through-silicon vias^{150,151} can be used, respectively. Here, a through-silicon via is a coaxial structure that passes through a silicon wafer.

Recently, it has been reported that the 2D lattice for the surface code can be folded like origami as shown in Fig. 20(b).¹⁵² In this architecture, qubits and control lines can be fabricated on the same plane if the coupling

resonators are allowed to intersect by air bridges [inset in Fig. 20(b)].¹⁴⁹ Because of these cross-connections, this method was named a pseudo-2D architecture. The appealing point of this architecture is that all qubits and their associated lines can exist on the same chip. Moreover, it can be made by utilizing the standard 2D microwave technology so that we can avoid the complex techniques required for a 3D architecture.

Possible concerns are cross-talk between intersecting resonators and the degradation of the quality factor caused by air bridges. In Ref. 152, it was shown that the cross-talk is at most about -50 dB; in addition, resonators with 15–20 air bridges showed an internal quality factor in a range where the infidelity is lower than the threshold value of the surface code.

VIII. CHARACTERIZING A QUANTUM SYSTEM

To control a quantum system precisely, we have to know the Hamiltonian of the system. In other words, a set of parameters, called system parameters, that characterize the system must be determined. Since the system parameters are based on our model describing the system, appropriate modeling is essential. For example, if we treat our qubit as an ideal two-level system as we did in Sec. VB1, knowing ω_q might be good enough to set up the Hamiltonian. However, for high-fidelity gate operation, we must consider higher excitation levels; hence, we have to extract more information, such as the transi-

TABLE IV. Minimal procedure for extracting system parameters and related experimental methods.

Measured quantities	Method	Comment
Resonator: resonance frequency, quality factor Anticrossing in the flux bias sweep (if existing): qubit-resonator coupling constant	Single-tone spectroscopy	
Qubit: transition frequency, sweet spot Anticrossing in the flux bias sweep (if existing): qubit-qubit coupling constant	Two-tone spectroscopy	
Rabi oscillation: pulse strength calibration	Time domain	ready for time-domain measurements
Dispersive shift: qubit-resonator coupling constant	Pulsed spectroscopy	ready for setting up the Hamiltonian
T_1 and T_2	Time domain	show the quality of qubits

tion frequency between $|1\rangle$ and $|2\rangle$. If our target operation requires strong drive, we may also have to consider the nonlinearity of the readout resonator.

In this section, we explain the minimal procedure for extracting system parameters and the related experimental methods. These are summarized in Table IV.

A. Spectroscopy

1. Single-Tone Spectroscopy

The first step in characterizing a superconducting qubit system is finding the resonance frequency of the readout resonator, ω_r . For this, we inject a microwave continuously (Continuous Wave, CW) and measure the S-parameters of the system as a function of microwave frequency [Fig. 21(a)]. This task is usually done using a vector network analyzer (VNA). Since a single microwave source, which is a part of the VNA, is used in this step, this type of measurement is called single-tone spectroscopy.

Since the transition frequency of the qubit, ω_q , is usually designed to be far detuned from ω_r for dispersive readout (Sec. VIB 1), most of the microwave power whose frequency is close to ω_q is filtered out by the resonator. As a result, the qubit signal is not visible in single-tone spectroscopy. This is why we need another type of spectroscopy, called two-tone spectroscopy.

If the qubit and the readout resonator are on-resonance at a certain external bias, we can estimate the qubit-resonator coupling constant g by observing the peak splitting as explained in Sec. VC. If the qubit is not tunable, we can still estimate g using the dispersive shift (Sec. VIIIA 3).

2. Two-Tone Spectroscopy

Once ω_r is known, we fix the excitation frequency of the VNA near ω_r for readout. Subsequently, we inject

another microwave to the circuit to drive the qubit. ω_q is found by sweeping the frequency of the second microwave, called the drive frequency ω_d , while monitoring the changes in the S-parameters of the readout resonator. If ω_d becomes close to ω_q , the S-parameters of the readout resonator will vary because of the dispersive shift in resonance frequency [Fig. 13(a)]. This type of measurement is called two-tone spectroscopy.

When we characterize ω_q , we have to minimize the excitation power of the VNA; if the excitation power is too high, then the readout resonator is populated by multiple photons, resulting in the shift or splitting of the qubit spectrum as mentioned in Sec. VIB 1.

We can repeat this procedure for different external biases to obtain the full bias dependence of ω_q , which informs us of the position of the sweet spot. If the transition frequencies of two qubits coincide at a certain bias, we can see an anticrossing. From this, we can estimate the qubit-qubit coupling constant.

3. Dispersive Shift

As explained in Sec. VIB 1, the dispersive shift χ is the qubit-state-dependent frequency shift of the readout resonator. From this, we can estimate the qubit-resonator coupling g using $\chi = g^2/\Delta_{qr}$, where $\Delta_{qr} = \omega_r - \omega_q$.

To measure χ , we first prepare the qubit state of either $|0\rangle$ or $|1\rangle$. In this step, a π -pulse is required to prepare $|1\rangle$. Because of this, the dispersive shift measurement has to be preceded by the Rabi oscillation measurement (Sec. VIIIB 1). Once the qubit state is prepared, we apply the readout pulse and measure the S-parameters. The sweep parameter is the frequency of the readout pulse [Fig. 21(a)]. Hence, the measurement of the dispersive shift is like pulsed single-tone spectroscopy with the qubit state preparation. By comparing the spectrum of the readout resonator with two different qubit states, we can obtain χ as shown in Fig. 13(a).

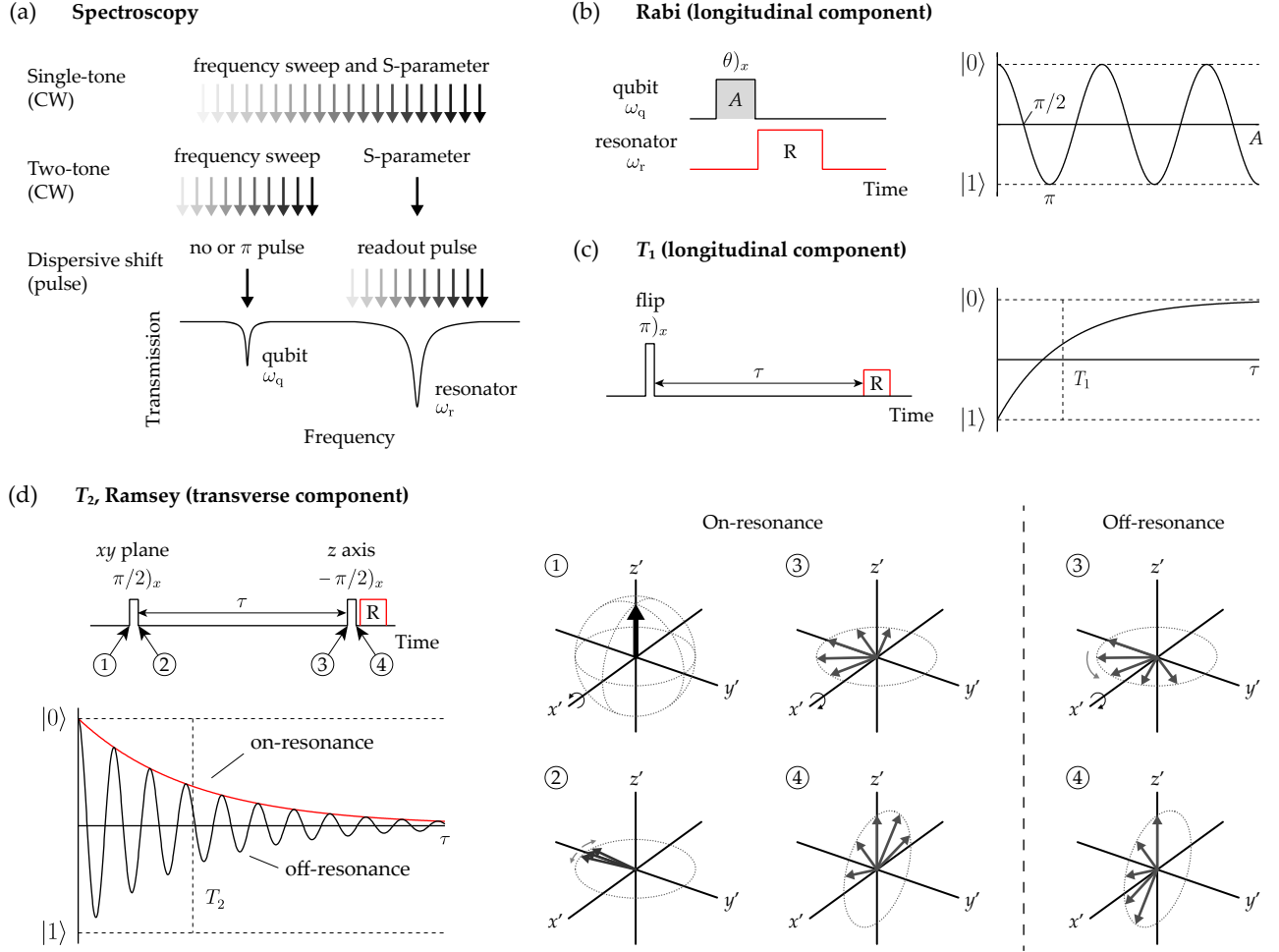


FIG. 21. (a) Spectroscopy (frequency domain). The control parameter of this type of measurement is the frequency of the applied microwave. Arrows represent microwave excitation, and the gradient of the arrows represents the frequency sweep direction from low to high frequency. The resonator and qubit signals are detected by the changes in the S-parameters of the system. For the circuit in Fig. 10(a), the qubit and the resonator signals can be detected through the transmission. “CW” stands for continuous wave. (b–d) Time domain measurements. Each figure represents the pulse sequence and typical measurement result for (b) Rabi oscillation, (c) T_1 , and (d) T_2 measured via the Ramsey fringes. Note that each graph represents the averaged result of a set of identical measurements; the result of a single-shot readout is digital. The readout pulses are in red and labeled “R”. τ indicates the time interval, which is the independent variable. “A” in (b) indicates the area of the drive pulse. $(\theta)_x$ is shorthand notation of $\hat{R}_x(\theta)$. The circled numbers in (d) describe the evolution of the qubit state in the Bloch sphere. (The longitudinal relaxation process is ignored for clarity.) Each arrow represents the qubit state for each measurement. The average z' -component in ④ is recorded as a result. Note that, in (d), $\pm\pi/2)_x$ pulses are required at the beginning and end of the sequence to transfer the z' -component of the Bloch vector to the y' -component, and vice versa. If the external drive and qubit transition frequency are off-resonance, the Bloch vector rotates about the z' -axis. This results in an oscillation called Ramsey fringes.

B. Time-Domain Measurement

According to quantum theory, the measurement forces the qubit state to collapse to either the $|0\rangle$ or $|1\rangle$ state, as emphasized in Secs. VIE 2 and VII. Hence, to extract the parameters mentioned in this section, we have to make a set of measurements and take the average.

1. Rabi Oscillation

In time-domain measurements, we calibrate the qubit drive by observing the Rabi oscillation [Fig. 21(b)]. First, the qubit drive pulse with ω_q is applied to excite the qubit. After the drive pulse, the readout pulse near ω_r is applied, and the S-parameters of this readout pulse are measured via quadrature detection.^{4,102} The sweep parameter is the area of the drive pulse; in actual exper-

iments, it can be either the length or amplitude of the drive pulse.

Since the drive pulse rotates the qubit state in the Bloch sphere (Fig. 15), and the dispersive measurement detects the longitudinal component of the Bloch vector (Sec. VIB 1), the amplitude of the signal oscillates with the drive pulse area: this oscillation is the Rabi oscillation. The Rabi oscillation provides a correspondence between the nutation angle of the Bloch vector and the drive pulse area. The names of frequently used pulses, such as π - and $\pi/2$ -pulses, indicates the nutation angles induced by such pulses.

If the sweep parameter is the length of the drive pulse τ_p , the following function is used for fitting:

$$f(\tau_p) = A_0 + A_1 \cos(\Omega_R \tau_p + A_2) \exp\left(-\frac{\tau_p}{T_R}\right), \quad (103)$$

where the fitting parameters are A_0 , A_1 , A_2 , Ω_R , and T_R . Among them, only Ω_R (Rabi frequency) and T_R (characteristic decay time of the Rabi oscillation) are physically meaningful quantities. Note that the exponential decay is also required to fit the data properly. The main reason for this decay is finite T_1 and fluctuations in Ω_R .^{21,153}

With the extracted system parameters, we can establish the correspondence between the control parameters we set and the actual response of the system. This process is called calibration. The Rabi oscillation measurement is the simplest calibration procedure; however, the Rabi frequency estimated from this method is usually not accurate enough for high-fidelity control. Probably the next simplest and more accurate one is to apply a train of pulses; interested readers should see Refs. 154 and 155. Optimal control theory can also be adopted; see Refs. 156 and 157. More advanced techniques for Google's devices can be found in Refs. 158 and 159 and the supplementary materials for Ref. 160.

2. Relaxation Time: T_1

The measurement procedure for the longitudinal relaxation time (T_1) is shown in Fig. 21(c). Since the dispersive readout measures the longitudinal component of the Bloch vector, all we have to do is apply a pulse (often but not necessarily a π -pulse) and detect the population of $|0\rangle$ as a function of the time interval. During this time interval, the qubit relaxes back to $|0\rangle$. By fitting the population of $|0\rangle$ with an exponential function, we can extract T_1 . Hence, the fitting function has the following form:

$$f(\tau) = A_0 + A_1 \exp\left(-\frac{\tau}{T_1}\right), \quad (104)$$

where τ is the time interval between the drive and readout pulses, and the fitting parameters are A_0 , A_1 , and T_1 .

3. Relaxation Time: T_2

The standard measurement procedure for the transverse relaxation time (T_2) is to observe the Ramsey fringes [Fig. 21(d)]. Since we need to detect the transverse component of the Bloch sphere, we apply a $\pi/2$ pulse at the beginning of the time interval and then a $-\pi/2$ pulse to transfer the transverse component back to the longitudinal component. Subsequently, we make a detection. The time constant for the decay of the $|0\rangle$ population is T_2 .

If $\omega_d = \omega_q$ (on-resonance), we observe single exponential decay shown on the left side of Fig. 21(d). However, if $\omega_d \neq \omega_q$ (off-resonance), the Bloch vector will acquire an additional rotation in the $x'y'$ plane during the time interval, resulting in an oscillation with the frequency $\omega_d - \omega_q$. The reason for the oscillation is that only the transverse component perpendicular to the rotating axis is transferred to the longitudinal component. This oscillation is called Ramsey fringes.

The fitting function is

$$f(\tau) = A_0 + A_1 \cos(\omega_{qd}\tau + A_2) \exp\left(-\frac{\tau}{T_2}\right), \quad (105)$$

where τ is the time interval between the $\pm\pi/2$ pulses, and the fitting parameters are A_0 , A_1 , A_2 , ω_{qd} , and T_2 . Here, ω_{qd} is the frequency detuning ($\equiv \omega_d - \omega_q$) from which we can obtain a precise value of ω_q .

If the dephasing process is dominated by low-frequency noise, the line shape of the qubit spectrum is close to Gaussian rather than Lorentzian.^{25,26} This happens easily when the flux bias is out of the sweet spot. In this case, the fitting function (ω_{qd} is assumed to be zero for simplicity)

$$f(\tau) = A_0 + A_1 \exp\left(-\frac{\tau^2}{T_G^2}\right) \exp\left(-\frac{\tau}{2T_1}\right) \quad (106)$$

fits the data better than the simple exponential decay function because the Fourier transformation of a Gaussian is also a Gaussian. Here, T_1 is not a fitting parameter; it has to be measured independently (Sec. VIIB 2). The fitting parameter T_G can be practically considered as $1/\Gamma_\varphi$, although it is not mathematically identical to $1/\Gamma_\varphi$ because Γ_φ is defined in an exponential decay function (see Sec. IVA 1).

IX. CONTROLLING A QUANTUM SYSTEM

In this section, we discuss how to control a superconducting qubit system. As a quantum computing system becomes larger, its precise control becomes as important as making the system itself. Without efficient control, we cannot reduce errors enough to perform quantum error correction.

What does “controlling a quantum system” mean?

Consider the Hamiltonian

$$\hat{\mathcal{H}}(t) = \hat{\mathcal{H}}_0 + \sum_{k=1}^K u_k(t) \hat{\mathcal{H}}_k, \quad (107)$$

where $\hat{\mathcal{H}}_0$ is the system Hamiltonian, $\hat{\mathcal{H}}_k$ is the control Hamiltonian, u_k are the control parameters, and K is the number of the control parameters. Controlling a quantum system means finding $u_k(t)$ that drive a quantum state of the system to the desired state.¹⁶¹ Single qubit gates in Sec. VIC are good examples. In this case, the control Hamiltonian is $\hat{\mathcal{H}}_d$ [Eq. (61)], and the control parameters are $\mathcal{E}_r(t)$ and the phase of the drive pulse, which selects the rotation axis.

To achieve a high-fidelity gate operation, a control pulse must satisfy the following conditions:

1. *Fast qubit manipulation*: The control pulse must be as short as possible to avoid loss of coherence.
2. *Narrow excitation bandwidth*: The excitation bandwidth has to be sufficiently narrow to minimize the information leakage through an unwanted transition. For a multiqubit system, the excitation bandwidth of the readout pulse is also important because the readout of a certain qubit might induce the dephasing of other qubits by populating readout resonators for these qubits (see Sec. VIB1).
3. *Decoupling from unwanted interactions*: Couplings to uncharted or unaccountable external degrees of freedom, which induce unwanted interactions and information leakage, should be minimized.
4. *Self-compensating*: The gate operation must compensate for the complex response of classical control electronics: bandwidth and long-time transients or nonlinearity such as kinetic inductance in a superconducting resonator, amplifier nonlinearity, or mixer imbalance. Although these nonlinearity is controllable in principle,¹⁶² it is a difficult task. Thus, the best option is to minimize any unnecessary nonlinearity by careful device design and operating the amplifier in the linear regime, which will set the power limit.
5. *Robustness against experimental imperfections*: The control must be robust against uncertainties and stochastic variations in the system's internal and control Hamiltonians, such as amplitude and phase noises in the control pulse.

This section is presented to answer the question of how to optimize the control pulse to satisfy the above criteria. A good introduction to this topic can be found in Refs. 163 and 164.

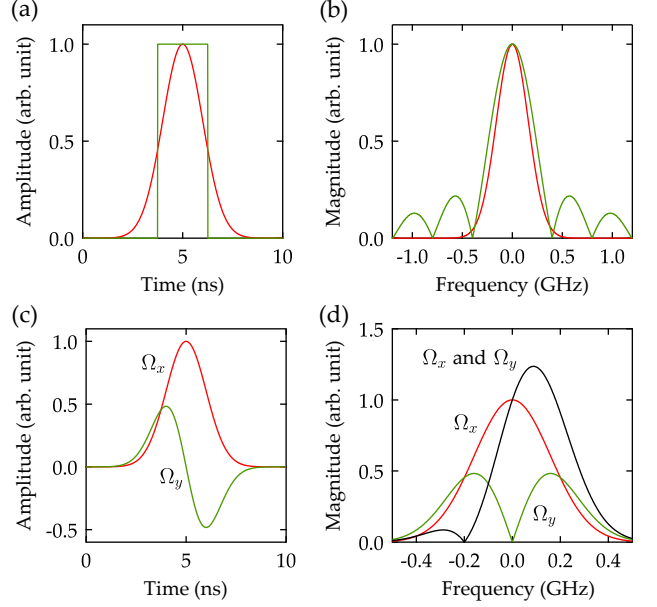


FIG. 22. (a) Square (green) and Gaussian (red) pulses with the same area in the time domain. (b) In the frequency domain, it is evident that the excitation bandwidth of a Gaussian pulse (red) is narrower than that of a square pulse (green). (The Fourier transformation of a Gaussian is also Gaussian.) (c) and (d) DRAG pulse implemented in Gaussian pulse with anharmonicity $\alpha = 2\pi(-200)$ MHz. Ω_x and Ω_y indicate the quadratures of the pulse [Eq. (108)]. In (d), note that the Fourier component of the DRAG pulse (black curve) is suppressed at the position of anharmonicity, resulting in the suppression of the information leakage from $|1\rangle$ to $|2\rangle$.

A. Elementary Pulse Shaping

1. Excitation Bandwidth

In this subsection, we estimate the excitation bandwidth by Fourier transforming the pulse applied to the qubit. We stress that this method is valid only if the system's response is linear, while the evolution on the Bloch sphere is intrinsically nonlinear.^{165,166} To control the excitation bandwidth precisely, we must solve the full equation of motion of the system. Here, we use the concept of Fourier transformation because it simplifies our discussion and helps develop intuition.

To grasp the concept of controlling the excitation bandwidth, we compare two widely used pulses: square and Gaussian pulses. As shown in Fig. 22(a) and (b), the excitation bandwidth of a Gaussian pulse is significantly narrower than that of a square pulse.¹⁶⁷ One drawback of a Gaussian pulse is that it does not have well-defined starting and end points; hence, the pulse envelope must be truncated somewhere.¹⁶⁸ Because of this, a cosine pulse is also widely used.

For qubits like transmons, however, a Gaussian pulse is still not enough to perform nanosecond qubit control

because of the bandwidth of 100 MHz order, which is comparable to the typical anharmonicity of a transmon [Fig. 22(b)]. A pulse with this bandwidth is likely to induce transitions not only between $|0\rangle$ and $|1\rangle$ but also between $|1\rangle$ and $|2\rangle$, resulting in information leakage out of the computational subspace. A more advanced pulse resolving this issue is the Derivative Removal by Adiabatic Gate (DRAG) pulse.¹⁶⁹ The DRAG scheme is very effective for weakly nonlinear qubits, such as transmons; all high-fidelity controls achieved in superconducting qubit systems are based on the DRAG pulse and its variants.

Here, we explain the DRAG pulse in an intuitive way using the Fourier transformation following Ref. 170. Consider a single qubit driven by the following Hamiltonian (in the rotating frame):

$$\hat{\mathcal{H}}_d^{\text{rot}} = \hbar\Omega_x(t)\frac{\hat{\sigma}_x}{2} + \hbar\Omega_y(t)\frac{\hat{\sigma}_y}{2}, \quad (108)$$

where $\Omega_{x(y)}$ is the amplitude for the rotation about the $x(y)$ -axis. This is just an extension of Eq. (66). For a qubit system whose anharmonicity is α , the DRAG condition is given by

$$\Omega_y(t) = -\frac{\dot{\Omega}_x(t)}{\alpha}. \quad (109)$$

That is, the imaginary part of the pulse is the derivative of the real part as shown in Fig. 22(c).

In the frequency domain, taking the derivative gives sharp suppression at a certain frequency [black curve in Fig. 22(d)]. The coefficient $-1/\alpha$ in Eq. (109) matches this suppressed frequency and the transition frequency between $|1\rangle$ and $|2\rangle$. This idea is very intuitive and easy to apply; for example, if we want to suppress two frequencies, one higher and the other lower than our working frequency, we can simply take a second derivative of the pulse as the imaginary part.¹⁷⁰ Although we explained the DRAG scheme for a Gaussian pulse, the concept of the DRAG pulse can also be applied to other pulse shapes.

One interesting point of view is to consider the DRAG scheme as an extension of “shortcuts to adiabaticity”, which are fast routes to the final results of slow, adiabatic changes of the controlling parameters of a system.¹⁷¹ From this point of view, the imaginary part of the pulse makes the qubit couple to the non-computational subspace only adiabatically, resulting in the removal of population leakage.¹⁷² Interested readers should see Refs. 171 and 172.

2. Pulse Distortion

Although we carefully design a microwave or a DC pulse for qubit control, the shape of the pulse is distorted as it travels from the pulse generator to the qubit. This is mainly due to the finite bandwidth of various electrical components, such as cables, filters, and resonators. The

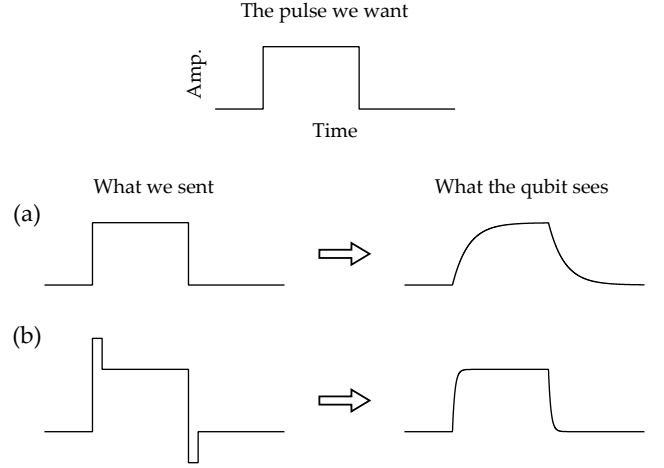


FIG. 23. Pulse distortion due to the finite response time of various electronics.

problem is even worse for the readout pulse because, in this case, the pulse is close to the resonance of the high-quality superconducting resonator. A typical example of pulse distortion is shown in Fig. 23(a). If the time scale of the transient is not negligible compared with T_1 , which is often the case, the readout fidelity will be limited. The simplest solution is to add overshoot and negative pulses at the beginning and end of the readout pulse as shown in Fig. 23(b).¹⁷³

A more advanced way to solve this problem is to model the transient behavior using various filter functions^{174,175} or an RLC circuit.^{162,176}

B. Numerical Optimization

The goal of optimal control is to find a set of control parameters that minimize the cost function. Here, the cost function, also called the performance measure, is a measure of how far the performance of a system is from the target one.¹⁷⁷ If our interest is unitary gate optimization, gate infidelity J_{gate} is a natural choice as the cost function. Mathematically, J_{gate} is defined by

$$J_{\text{gate}} \equiv 1 - \left| \text{tr} \left\{ \hat{U}_{\text{target}}^\dagger \hat{U}(T) \right\} \right|^2, \quad (110)$$

where \hat{U}_{target} and $\hat{U}(T)$ are the target and the final unitary gates, respectively. For ideal gate operation, $J_{\text{gate}} = 0$. If we want to let the system evolve to the target state (state-to-state transfer), state infidelity $J_{\text{state}} (\equiv 1 - |\langle \psi_{\text{target}} | \psi(T) \rangle|^2)$ is used as the cost function.

There are two types of optimization algorithm: gradient-based and gradient-free. In gradient-based algorithms, the performance of the pulse is evaluated by the cost function. Then, the control parameters are updated for the next iteration based on the derivative of the cost function with respect to the control parameters.

The advantage of gradient-based algorithms is that they are much faster than gradient-free algorithms. However, gradient-based algorithms do not work well if the cost function is discontinuous or noisy because calculating the gradient is difficult in such a case. Thus, they are difficult to use for direct optimization on an experimental system, i.e., closed-loop optimal control.

Despite their slowness, gradient-free algorithms are simple to implement and work well with a noisy measurement outcome, suggesting that we can perform closed-loop optimal control using these algorithms. Thus, gradient-free algorithms are useful for the calibration or optimization of pulses defined by a limited number of parameters.^{156,157}

There are many numerical optimization algorithms that have been used widely in quantum control. One helpful “decision tree” for the choice of an optimization algorithm is available in Ref. 178.

1. GRAPE Algorithm

We introduce Gradient Ascent Pulse Engineering (GRAPE)¹⁷⁹ because it has been found to be one of the most reliable algorithms for controlling quantum systems. As the name implies, GRAPE is a gradient-based algorithm. Hence, it is fast but the control parameters are determined in simulations. This suggests that the GRAPE algorithm requires complete system modeling.

In the GRAPE algorithm, the control pulses are defined as a collection of pulses with a piecewise constant amplitude and phase over a number of intervals N , each of length Δt , which yields an overall pulse length of $T = N\Delta t$ [see Figs. 24(insets) and 25]. Hence, the control parameters are a set of amplitudes and phases (or amplitudes of two quadratures) of these piecewise pulses.

A brief description of the GRAPE algorithm for unitary gate optimization is as follows (Fig. 24):

1. *Characterize the system*: In this step, the system parameters are extracted as described in Sec. VIII. From these parameters, we set up the model Hamiltonian that describes the dynamics of the system properly [$\hat{\mathcal{H}}_0$ in Eq. (107)].
2. *Guess initial control parameters and construct the Hamiltonian*: With a set of initial control parameters, we can construct the full Hamiltonian [$\hat{\mathcal{H}}$ in Eq. (107)]. An example of the initial pulse shape is shown in the upper inset of Fig. 24.
3. *Calculate the propagator*: The time evolution of the system during a time step j is given by the propagator [Eq. (49)]

$$\hat{U}_j = \exp \left[-i \frac{\Delta t}{\hbar} \left\{ \hat{\mathcal{H}}_0 + \sum_k^K u_k(j) \hat{\mathcal{H}}_k \right\} \right]. \quad (111)$$

Thus, $\hat{U}(T) = \hat{U}_N \cdots \hat{U}_1$.

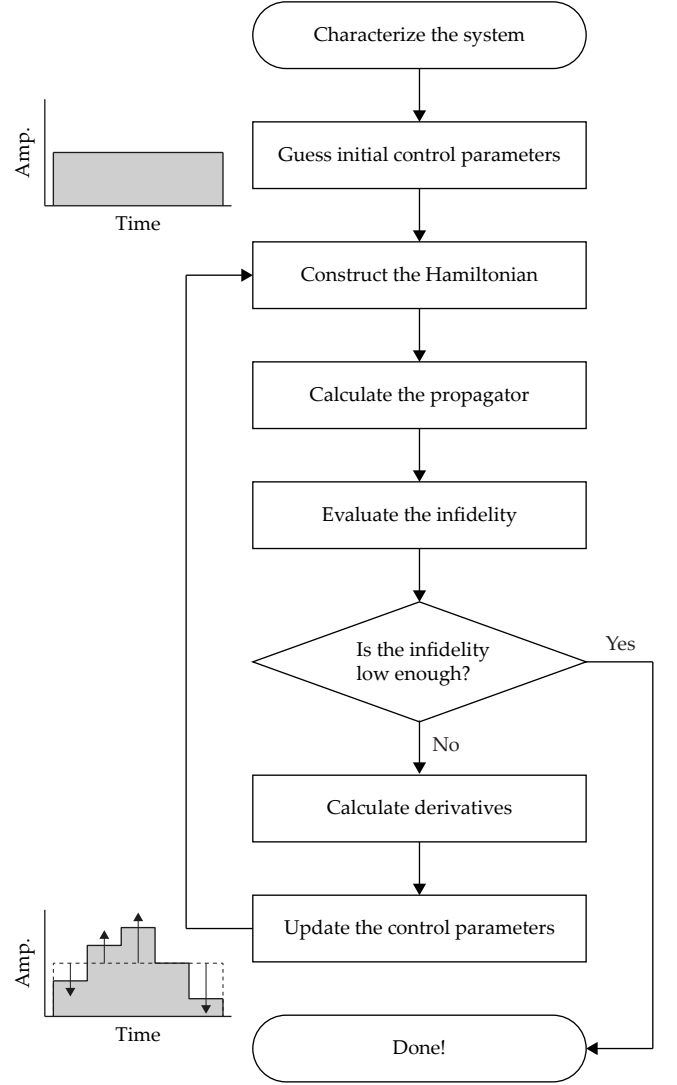


FIG. 24. Procedure for typical gradient-based numerical pulse optimization. The upper inset shows an example of the initial pulse shape. In the lower inset, the dashed line indicates the initial pulse, and the vertical arrows represent gradients, indicating how each amplitude should be modified in the next iteration in order to reduce the cost function. The solid line represents the resulting updated pulse shape.

4. *Evaluate the fidelity*: In this step, it is determined how close the resulting state is to the target one via J_{gate} .
5. *Calculate derivatives and update the control parameters*: The update of the control parameters can be written as

$$u_k(j) \rightarrow u_k(j) + \epsilon \frac{\delta J_{\text{gate}}}{\delta u_k(j)}, \quad (112)$$

where ϵ is an adjustable small step size. An example is shown in the lower inset of Fig. 24. For small enough Δt , the gradients are calculated using the

following formula¹⁷⁹

$$\frac{\delta J_{\text{gate}}}{\delta u_k(j)} \approx -2 \text{Re} \left\{ \text{tr} \left(i \frac{\Delta t}{\hbar} \hat{\mathcal{H}}_k \hat{V}_j \hat{\Lambda}_j^\dagger \right) \text{tr} \left(\hat{V}_j^\dagger \hat{\Lambda}_j \right) \right\}, \quad (113)$$

where \hat{V}_j and $\hat{\Lambda}_j$ are defined by

$$\begin{aligned} J_{\text{gate}} &= 1 - \left| \text{tr} \left\{ \underbrace{\hat{U}_{\text{target}} \hat{U}_N \cdots \hat{U}_{j+1}}_{\equiv \hat{\Lambda}_j^\dagger} \underbrace{\hat{U}_j \cdots \hat{U}_1}_{\equiv \hat{V}_j} \right\} \right|^2 \\ &= 1 - \text{tr} \left(\hat{V}_j \hat{\Lambda}_j^\dagger \right) \text{tr} \left(\hat{V}_j^\dagger \hat{\Lambda}_j \right). \end{aligned} \quad (114)$$

Here, the property that the trace is invariant under cyclic permutations was used.

Note that the piecewise constant amplitude and phase assumption is not valid in reality because of the pulse distortion mentioned in Sec. IX A 2. However, this does not make the pulse optimization particularly harder. Once the transient behavior is suitably modeled, it can be integrated into the GRAPE algorithm easily by introducing an additional level of discretization. One discretization is for integrating the state evolution and the other is for the control parameters.^{176,180,181}

2. Example: Controlling Excitation Bandwidth

Here, we use GRAPE to control the excitation bandwidth. For simplicity, we consider a single transmon system (Sec. IV B 1) controlled by an on-resonance external drive, $\omega_d = \omega_q$.

a. Goal. The quantum state of a transmon can evolve easily outside of the computational subspace because of the small anharmonicity. This causes the qubit state to acquire an unwanted phase that degrades the fidelity. Hence, our goal is to find the shortest pulse shape that suppresses the qubit evolution outside of the computational subspace. If our target gate U_{target} is the X gate, it can be written in matrix form as

$$U_{\text{target}} = \begin{matrix} & \langle 0| & \langle 1| & \langle 2| \\ \begin{matrix} |0\rangle \\ |1\rangle \\ |2\rangle \end{matrix} & \begin{pmatrix} 0 & 1 & 0 \\ 1 & 0 & 0 \\ 0 & 0 & e^{i\phi_2} \end{pmatrix} \end{matrix}. \quad (115)$$

where ϕ_2 is the relative phase of $|2\rangle$ acquired during the evolution. Although we do not need ϕ_2 for the gate operation, the fidelity must be calculated as a function of ϕ_2 because only a certain range of ϕ_2 gives a high-fidelity gate solution.

b. Hamiltonian. Our system Hamiltonian $\hat{\mathcal{H}}_0$ in the rotating frame, whose angular velocity is the same as ω_q ,

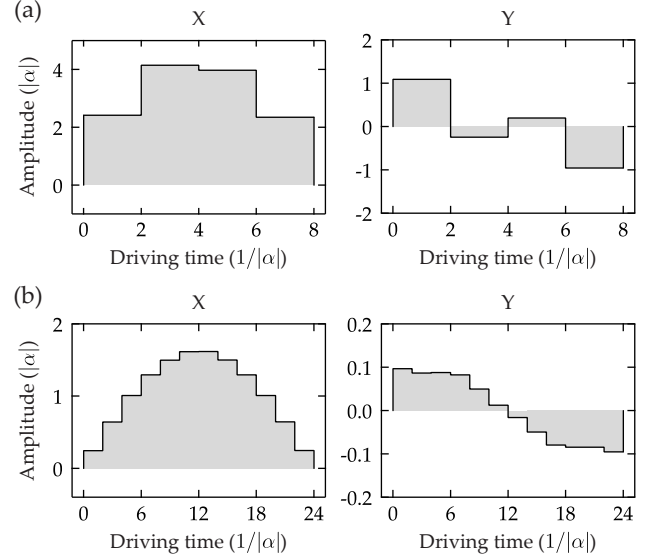


FIG. 25. Examples of optimal solutions (smallest length and maximum amplitude) for π -rotation obtained from the GRAPE algorithm. The fidelity is higher than 0.99999. The left figures show the Ω_x (X) quadrature and the right figures show the Ω_y (Y) quadrature. (a) When the width of the time slice is $2/|\alpha|$, the minimal number of slices required to reach ≥ 0.99999 fidelity is 4. (b) If there are amplitude constraints caused by hardware limitations, we can find an optimal solution with a longer gating time in a limited power range. Note that the amplitude of the Y quadrature is only 1/10 that in (a). This is due to the longer pulse having narrower bandwidth; thus, less phase correction is needed. Also note that the shape of the Y quadrature is close to the derivative of the X quadrature, implying that GRAPE takes the idea of the DRAG scheme. For a system with $\alpha = 2\pi(-200)$ MHz, the unit step $1/|\alpha|$ corresponds to 0.8 ns. In this case, the gating times for (a) and (b) are 6.4 ns and 19.2 ns, respectively. The initial control parameters for the X quadrature are a Gaussian-like shape whose area is roughly π ; for the Y quadrature, they are all zeros. For these figures, the Quantum Util package was used.¹⁸⁰

is given by

$$\hat{\mathcal{H}}_0 = \begin{pmatrix} 0 & 0 & 0 \\ 0 & 0 & 0 \\ 0 & 0 & \alpha \end{pmatrix}, \quad (116)$$

where $\alpha(\equiv \omega_{12} - \omega_q)$ is the anharmonicity.

The control parameter is the amplitude of the external drive. Thus, the control Hamiltonian $\hat{\mathcal{H}}_{\text{ctrl}}$ is given by

$$\hat{\mathcal{H}}_{\text{ctrl}}(t) = \frac{\hbar \Omega_x(t)}{2} \begin{pmatrix} 0 & 1 & 0 \\ 1 & 0 & \lambda \\ 0 & \lambda & 0 \end{pmatrix} + \frac{\hbar \Omega_y(t)}{2} \begin{pmatrix} 0 & -i & 0 \\ i & 0 & -i\lambda \\ 0 & i\lambda & 0 \end{pmatrix}. \quad (117)$$

Here, $\Omega_{x(y)}$ is the amplitude of the rotation about the $x(y)$ -axis, and the matrix next to $\Omega_{x(y)}$ is the three-level-system version of the $\hat{\sigma}_{x(y)}$ operator with the relative strength of the $|1\rangle$ - $|2\rangle$ transition with respect to

the $|0\rangle\text{--}|1\rangle$ transition denoted as λ . For a transmon, $\lambda = \sqrt{2}$ (Ref. 20). We also use this number. We emphasize that the y -rotation is implemented by $-\sin(\omega_d t)$, not by $+\sin(\omega_d t)$, as mentioned in Sec. VIC.

c. Constraint. The constraint is usually set by our instruments. In this case, it is the maximal power of the drive.

d. Result. The optimal pulse shape found by GRAPE is shown in Fig. 25. If the system is an ideal two-level system, i.e., $\lambda = 0$, we do not need one of the quadratures, say Ω_y , and any shape satisfying $\int_0^\tau \mathcal{E}_x(t)dt = \pi$ achieves a perfect π -rotation, where τ is the total gate time. However, because of the existence of $|2\rangle$, the numerical solutions found by GRAPE have $\Omega_y(t)$ whose shape is similar to that of the DRAG pulse as shown in Fig. 25.

C. Refocusing Technique

Although a qubit must interact with external systems to be controlled or read, the interaction must be turned on only when we need it. Any unwanted interaction makes the qubit lose its coherence and degrades the performance of gate operation. The problem is that interactions associated with qubits are not always controllable; even if we can control some of the interactions using a tunable coupler or flux bias, such control knobs always introduce additional noises. A refocusing technique¹⁸⁵ allows us to cancel the evolution caused by unwanted interactions by applying appropriate pulses that can effectively reverse the direction of evolution. In this context, such a pulsing technique is also called dynamical decoupling.^{186,187}

The simplest and most well-known refocusing scheme is the Hahn echo sequence [Fig. 26(a)].⁸ The Bloch spheres with circled numbers show how the qubit state evolves in repeated identical measurements. If the transition frequency of a qubit fluctuates for each measurement because of noise or unwanted interactions, then the qubit will lose its phase coherence [③ in Fig. 26(a)] (Sec. IV A 3). Here, the role of the π pulse is to flip the population of the qubit, thus reversing the direction of evolution [④ in Fig. 26(a)]. This makes the net area of the “direction of evolution” in Fig. 26(a) zero, indicating that the unwanted evolution is canceled out. Thus, T_2 measured using this pulse sequence is usually much longer than that measured via the Ramsey fringes (Sec. VIII B 3). To distinguish the relaxation time constants obtained from the Ramsey fringes and Hahn echo sequence, notations such as T_2^{Ramsey} and T_2^{echo} are often

used.⁹

Now, we explain more precisely how the Hahn echo sequence works. The first thing we have to do is distinguish the state preparation from the actual refocusing operation. For this, we rewrite the Hahn echo sequence as

$$\pi/2)_x - \tau/2 - \pi)_x - \tau/2 - \pi)_x - -\pi/2)_x. \quad (118)$$

Combining the last two pulses gives the sequence in Fig. 26(a). Note that, in the pulse sequence for the Ramsey fringes [Fig. 21(d)], the $\pm\pi/2$ -pulse transfers the longitudinal component to the transverse component and vice versa for the state preparation and measurement. The role of the $\pm\pi/2$ -pulse in Eq. (118) is the same—it is not an essential part of the refocusing process. The refocusing for an arbitrary qubit state is done by two π -pulses.

Consider an interaction between a qubit of interest and the coupled system, such as other qubits or the environment, with the following form:

$$\hat{\mathcal{H}}_{\text{qe}} = \hbar J_z \hat{\sigma}_z^{(q)} \hat{A}^{(e)}, \quad (119)$$

where J_z is the coupling constant, $\hat{\sigma}_z^{(q)}$ is the Pauli operator for the qubit, and $\hat{A}^{(e)} (\in \{\hat{I}^{(e)}, \hat{\sigma}_x^{(e)}, \hat{\sigma}_y^{(e)}, \hat{\sigma}_z^{(e)}\})$, where \hat{I} is the identity operator) is an operator associated with the coupled system. If we ignore this interaction during the time when the pulse is turned on, i.e., the pulse length is very small compared with τ , the propagator for the Hahn echo sequence can be written as [using Eq. (49)]

$$\hat{U}_{\text{echo}} = \hat{X} \hat{U}_{\text{qe}}(\tau/2) \hat{X} \hat{U}_{\text{qe}}(\tau/2), \quad (120)$$

where

$$\hat{U}_{\text{qe}}(t) = e^{-i\hat{\mathcal{H}}_{\text{qe}}t/\hbar}, \quad (121)$$

and \hat{X} is the X gate acting on the qubit. Using the two identities

$$\hat{U}e^{\hat{B}}\hat{U}^\dagger = e^{\hat{U}\hat{B}\hat{U}^\dagger}, \quad \hat{\sigma}_x\hat{\sigma}_z\hat{\sigma}_x = -\hat{\sigma}_z, \quad (122)$$

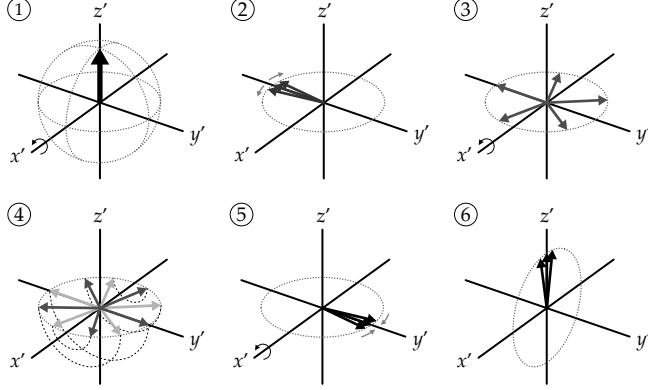
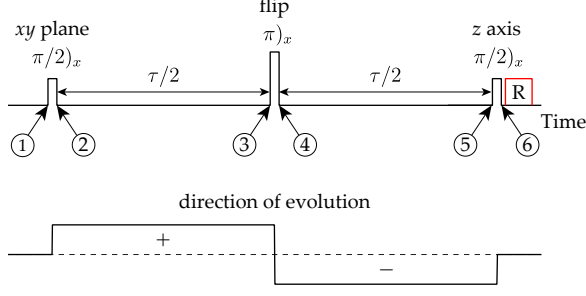
where \hat{U} is a unitary operator and \hat{B} is an arbitrary operator, it is easy to show that

$$\begin{aligned} \hat{X} \hat{U}_{\text{qe}}(\tau/2) \hat{X} &= \hat{\sigma}_x^{(q)} e^{-i\hat{\mathcal{H}}_{\text{qe}}\tau/2\hbar} \hat{\sigma}_x^{(q)} \\ &= e^{-i\hat{\sigma}_x^{(q)} \hat{\mathcal{H}}_{\text{qe}} \hat{\sigma}_x^{(q)} \tau/2\hbar} \\ &= e^{-iJ_{zz}(\hat{\sigma}_x^{(q)} \hat{\sigma}_z^{(q)} \hat{\sigma}_x^{(q)}) \hat{A}^{(e)} \tau/2} \\ &= e^{-iJ_{zz}(-\hat{\sigma}_z^{(q)}) \hat{A}^{(e)} \tau/2} \\ &= \hat{U}_{\text{qe}}(-\tau/2), \end{aligned} \quad (123)$$

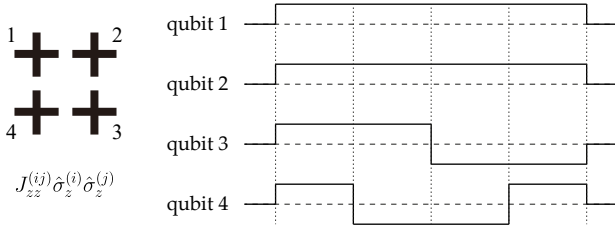
⁸ Although the majority of the literature, including this tutorial, calls the pulse sequence in Fig. 26(a) the Hahn echo sequence, it was proposed by Carr and Purcell.¹⁸³ In Hahn’s original paper, he applied pulses with the same rotation angle.¹⁸²

⁹ In the magnetic resonance literature, the notations T_2^* and T_2 are used for T_2^{Ramsey} and T_2^{echo} , respectively, for historical reasons.

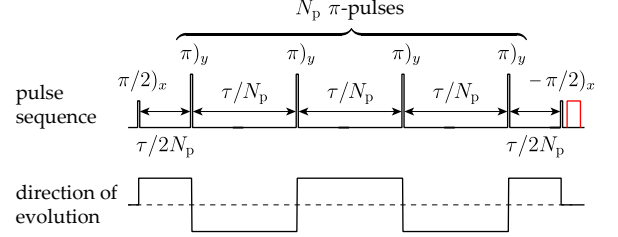
(a) Hahn echo pulse sequence



(b) Canceling the longitudinal qubit-qubit interaction



(c) CPMG pulse sequence



(d) Filter function

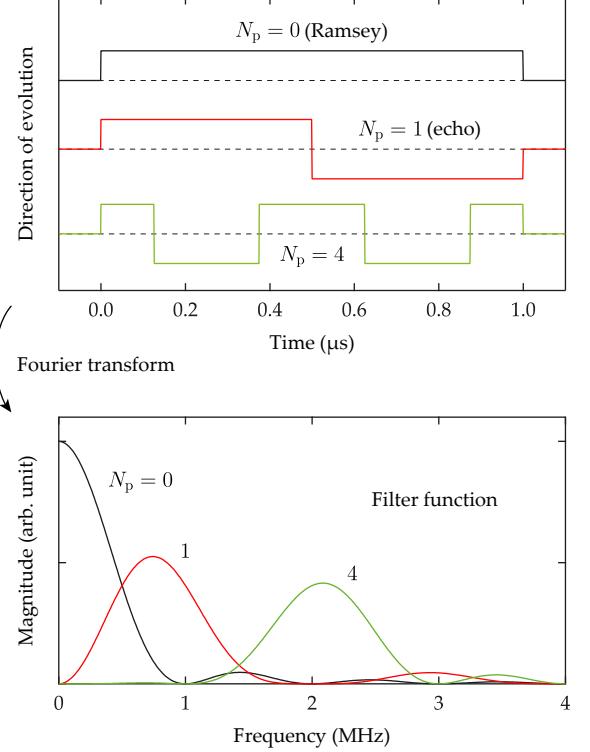


FIG. 26. (a) Hahn echo pulse sequence. τ is the time interval of the pulse sequence. The red pulse labeled “R” is the readout pulse. The circled numbers describe the evolution of the qubit state in the Bloch sphere. (The thermalization process is ignored for clarity.) (b) Refocusing scheme for a four-qubit system (four crosses) designed to control the ZZ interactions between qubit i and qubit j , $J_{zz}^{(ij)}$ (Ref. 104). In this sequence, all possible $J_{zz}^{(ij)}$ will be canceled out, except $J_{zz}^{(12)}$. The time interval is divided into four slices of equal duration by dotted lines. (c) Carr–Purcell–Meiboom–Gill (CPMG) pulse sequence. The red pulse is the readout pulse. Note that π -rotations are about the y -axis, while $\pi/2$ -rotations are about the x -axis. This change of the rotation axis prevents the accumulation of the error caused by imperfect π -pulses.¹²² (d) Concept of filter function. The modulation of the direction of evolution acts as a filter function in the frequency domain.

where the global phase was ignored. This suggests that two π -pulses act as a time-reversal operator. Thus, the Hahn echo sequence cancels any static interaction in the form of $\hat{\sigma}_z^{(q)} \hat{A}^{(e)}$.

Note that the Hahn echo sequence also cancels the $\hat{\sigma}_y^{(q)} \hat{A}^{(e)}$ interaction because $\hat{\sigma}_x \hat{\sigma}_y \hat{\sigma}_x = -\hat{\sigma}_y$. If we use an additional axis for π -pulses, either the y - or z -axis, we can also remove the $\hat{\sigma}_x^{(q)} \hat{A}^{(e)}$ interaction. Here, we choose

the z -axis as an example:

$$\begin{aligned} \hat{U}_{XY4} &= \hat{Z} \hat{U}_{\text{echo}} \hat{Z} \hat{U}_{\text{echo}} \\ &= \hat{Z} \hat{X} \hat{U}_{\text{qe}} \hat{X} \hat{U}_{\text{qe}} \hat{Z} \hat{X} \hat{U}_{\text{qe}} \hat{X} \hat{U}_{\text{qe}} \\ &= \hat{Y} \hat{U}_{\text{qe}} \hat{X} \hat{U}_{\text{qe}} \hat{Y} \hat{U}_{\text{qe}} \hat{X} \hat{U}_{\text{qe}}, \end{aligned} \quad (124)$$

where $\hat{Z}(\hat{Y})$ is the $Z(Y)$ gate acting on the qubit, and we omit the time interval in \hat{U}_{qe} to simplify the notation.

This pulse sequence is called XY4 (Refs. 189 and 190).

The Hahn echo sequence is also useful for a multiqubit system. Figure 26(b) shows an example of engineering ZZ interactions in a four-qubit system.¹⁰⁴ We can intuitively see which interaction will be eliminated by multiplying the two directions of evolution curves and checking if the net area is zero.

One might notice that, if we use the Hahn echo sequence to remove the ZZ interaction for the CR gate operation as mentioned in Sec. VID5, our gate operation based on the ZX interaction will also be removed. To prevent such a situation, we apply the π -pulses to the control qubit and change the sign of the CR drive after the first π -pulse.¹¹¹ As a result, the ZX interaction survives, while the ZZ interaction is canceled out.

The Hahn echo sequence works well only when the unwanted interaction is static in the time scale of τ . This means that only low frequency noise can be canceled out by the Hahn echo sequence. The Carr–Purcell–Meiboom–Gill (CPMG) pulse sequence [Fig. 26(c)], an extension of the Hahn echo sequence, can remove a wider frequency range of noise by applying multiple π -pulses.^{183,184} This can be understood using the concept of the filter function, which is basically the Fourier transformation of the direction of evolution.^{26,188} Figure 26(d) clearly shows that increasing the number of π -pulses filters out a wider range of low-frequency noise.

As the number of qubits increases, the dimension of the Hilbert space associated with the qubits increase exponentially and cannot be efficiently simulated on a classical computer, which is a requirement for optimization as suggested in Sec. IX B. Furthermore, the mere task of perfectly characterizing all multiqubit Hamiltonian terms becomes impossible. Nevertheless, the increase in T_2 by refocusing techniques shows us that we can engineer the system dynamics without full knowledge of the system-environment couplings and the state of the environment in some large Hilbert space that cannot be characterized. This success of the refocusing techniques arises from treating the problem perturbatively for a class of possible perturbations. These same ideas can be employed when controlling multiqubit systems whose Hilbert space can be divided into small manageable sectors (e.g., either one or a few qubits) with unwanted/uncharacterized Hamiltonian terms treated as perturbations. An approach based on this philosophy is effective Hamiltonian engineering. The most popular theoretical tool for this is average Hamiltonian theory. Interested readers should see Refs. 104, 165, 191–193.

D. Evaluation of Gate Operation

For precise quantum control, a quantitative measure that shows how close the actual gate operation is to the target operation is required. The quantity showing this is the error rate or gate infidelity J_{gate} [see Eq. (110) for the definition]. For the surface code, $J_{\text{gate}} \lesssim 0.01$ is required.

The standard method of estimating J_{gate} in the early days of quantum computation (before the 2010s) was quantum process tomography (QPT).¹⁰ Although it gives complete information about the dynamics occurring in the system during a given time, QPT has two drawbacks. First, it is not scalable—the time for fidelity estimation increases exponentially with the number of qubits. Second, QPT is susceptible not only to errors associated with gate operation but also to errors associated with state preparation and measurement (SPAM), resulting in inaccurate gate fidelity estimation.

Nowadays, the Clifford group randomized benchmarking (standard RB) is the standard measure of error rates associated with a set of gate operations, i.e., average gate fidelity, because of the following advantages. First, the Clifford group RB is scalable: the time for fidelity estimation increases polynomially with the number of qubits. Secondly, the estimated error is insensitive to the type of gate. Lastly, this protocol is robust against SPAM errors.

The idea of RB is to observe how the gate error accumulates with the number of gate operations, while SPAM errors remain similar with increasing number of gate operations. We can understand the idea of RB with a toy block analogy in the following way [Fig. 27(a)]. Imagine that we have lots of toy blocks in a toy storage bag with different height errors. Our job is to measure the average height error of these blocks. For this, we pick a set of m blocks randomly from the toy storage bag. Then, we stack these blocks and measure their total height. By comparing the measured height and our expected height from the design, we can estimate the error ε as shown in Fig. 27(a). We can repeat this process by varying m to obtain ε as a function of m [Fig. 27(c)]. The slope from the fitting indicates the average height error of the toy blocks [ε_1 in Fig. 27(c)]. The advantage of measuring the slope is that it is free from errors originating from an unintended position offset of the stack [ε_0 in Fig. 27(c)].

The procedure of RB is essentially the same as that of the toy blocks explained above. A toy block corresponds to a quantum gate, and the toy storage bag corresponds to the Clifford group. The main difference is that the experimentally measured quantity for the toy blocks is the error in height, which increases linearly with m , whereas the measured quantity for quantum gates is the survival probability, which decays exponentially with m . Here, the survival probability means the probability that the initial state is not changed by the gate sequence. After the entire process, the survival probability is fitted with the function $Ap^m + B$. The crucial point is that the average gate fidelity is estimated from p only; the effects of SPAM errors are reflected in A and B .

The detailed protocol of the standard RB is as follows:¹⁹⁴

1. Generate a sequence of $m+1$ gates picked uniformly at random from the Clifford group. Here, the last gate is chosen so that the net sequence is the identity operation.

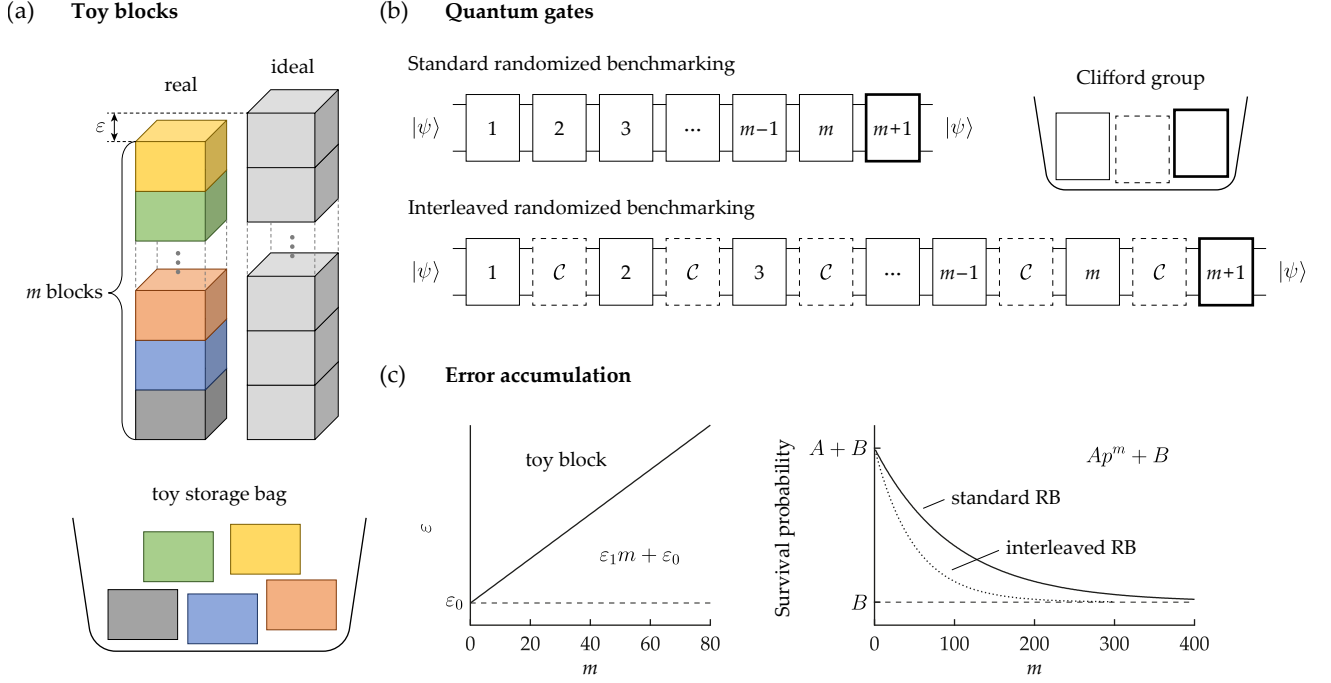


FIG. 27. (a) Toy block analogy of the Clifford group randomized benchmarking (standard RB). The toy storage bag corresponds to the Clifford group, and each toy block corresponds to a single gate operation. ε is the cumulative error in the total height. (b) In the standard RB, m gates randomly selected from the Clifford group are applied sequentially. In the interleaved RB, a random gate and the gate of interest \mathcal{C} (dashed rectangle) appear alternately. Here, the $(m+1)$ th gate (thick rectangle) is chosen so that the net sequence is the identity operation. (c) In the toy block analogy, the cumulative height error ε is fitted with the function $\varepsilon_1 m + \varepsilon_0$. This separates the average height error ε_1 (what we want) from an unintended position offset ε_0 (what we do not want). In RB, the survival probability, which is the probability that the initial state is not changed by the gate sequence, is fitted with the function $Ap^m + B$. Here, the average gate fidelity is estimated from p only; the effects of state preparation and measurement errors are reflected in A and B . Therefore, RB separates errors due to gate operations from that due to state preparation and measurement. In the graph, the survival probability for the interleaved RB decays faster than that for the standard RB. This is because there are twice as many applied gates in the interleaved RB.

2. Prepare a state, such as $|0\rangle$ for a single-qubit system or $|00\rangle$ for a two-qubit system.
3. Perform the gate operation.
4. Repeat steps 1–3 to measure the survival probability.
5. Repeat steps 1–4 for various m to obtain the survival probability as a function of m .
6. Fit the survival probability with the decay function $Ap^m + B$.
7. The average gate fidelity is given by $1 - r$, where $r = (d-1)(1-p)/d$, $d \equiv 2^n$ is the dimension of the Hilbert space, and n is the number of qubits.

The standard RB gives a single value, the average gate fidelity. Although such convenience is an advantage of RB, we often need to know the fidelity of a specific gate. One example is the fidelity evaluation for the closed-loop optimization of a certain gate operation.^{156,157} In this case, we use the interleaved RB.¹⁹⁵

The procedure for the interleaved RB is similar to that for the standard RB. The differences are (i) a random gate and the gate of interest \mathcal{C} appear alternately; (ii)

the infidelity associated with the gate of interest, $r_{\mathcal{C}}$, is given by $r_{\mathcal{C}} = (d-1)(1-p_{\mathcal{C}}/p)/d$, where $p_{\mathcal{C}}$ is the fitting parameter in the decay function and p is the fitting parameter obtained from the standard RB. Note that this formula works only when the gate error is due to a stochastic process, such as thermalization or dephasing. If the gate error is due to coherent errors, such as imprecise control errors, we might have interferences between these errors. In this case, we have to estimate the upper and lower bounds of $p_{\mathcal{C}}$ assuming the best and worst cases of interference.¹⁹⁶

Lastly, we point out that, although RB is scalable in principle, it is not clear in practice. The reason for this is that the implementation of the N -qubit Clifford operation requires $\mathcal{O}(N^2/\log N)$ primitive two-qubit gate operations,¹⁹⁷ which implies that, even if the gate fidelity of a primitive two-qubit gate looks reasonably good, the quality of the gate degrades rapidly with increasing number of qubits. This increases the number of measurements required to estimate the fidelity. One of the scalable alternatives is cycle benchmarking: in this protocol, the uncertainty of the fidelity estimate is independent of the

number of qubits. Interested readers should see Ref. 198.

ACKNOWLEDGMENTS

S.K. thanks Sota Ino, Paul Magnard, Hiroto Mukai, Shotaro Shirai, Teruaki Yoshioka, and Dengke Zhang for helpful discussions and Giuseppe Falci, Holger Haas, Ian Hincks, Anita Fadavi Roudsari, Rui Wang, Alex Wozniakowski, and anonymous reviewers for valuable comments on the manuscript. This work was supported by CREST, JST (Grant No. JPMJCR1676) and the New Energy and Industrial Technology Development Organization (NEDO).

- ¹J. Q. You and F. Nori, *Atomic physics and quantum optics using superconducting circuits*, Nature **474**, 589 (2011).
- ²G. Wendin, *Quantum information processing with superconducting circuits: a review*, Rep. Prog. Phys. **80**, 106001 (2017).
- ³X. Gu, A. F. Kockum, A. Miranowicz, Y.-x. Liu, and F. Nori, *Microwave photonics with superconducting quantum circuits*, Phys. Rep. **718–719**, 1 (2017).
- ⁴P. Krantz, M. Kjaergaard, F. Yan, T. P. Orlando, S. Gustavsson, and W. D. Oliver, *A quantum engineer's guide to superconducting qubits*, Appl. Phys. Rev. **6**, 021318 (2019).
- ⁵M. Kjaergaard, M. E. Schwartz, J. Braumüller, P. Krantz, J. I.-J. Wang, S. Gustavsson, and W. D. Oliver, *Superconducting Qubits: Current State of Play*, Annu. Rev. Condens. Matter Phys. **11**, 369 (2020).
- ⁶A. Blais, A. L. Grimsmo, S. M. Girvin, and A. Wallraff, *Circuit Quantum Electrodynamics*, arXiv:2005.12667.
- ⁷Transnational College of LEX, *What is Quantum Mechanics? A Physics Adventure* (Language Research Foundation, 1996).
- ⁸R. Shankar, *Principles of Quantum Mechanics* (Springer, 1994).
- ⁹J. J. Sakurai and J. Napolitano, *Modern Quantum Mechanics*, 2nd ed. (Pearson Education, 2011).
- ¹⁰M. Nielsen and I. Chuang, *Quantum Computation and Quantum Information: 10th Anniversary Edition* (Cambridge University Press, 2010).
- ¹¹N. Cody Jones, R. Van Meter, A. G. Fowler, P. L. McMahon, J. Kim, T. D. Ladd, and Y. Yamamoto, *Layered Architecture for Quantum Computing*, Phys. Rev. X **2**, 031007 (2012).
- ¹²J. M. Gambetta, J. M. Chow, and M. Steffen, *Building logical qubits in a superconducting quantum computing system*, npj Quantum Inf **3**, 2 (2017).
- ¹³G. Benenti, G. Casati, D. Rossini, and G. Strini, *Principles of Quantum Computation and Information: A Comprehensive Textbook*, 2nd ed. (World Scientific, 2018).
- ¹⁴B. Yurke and J. S. Denker, *Quantum network theory*, Phys. Rev. A **29**, 1419 (1984).
- ¹⁵A. J. Leggett, *Quantum Liquids* (Oxford University Press, 2006).
- ¹⁶M. Tinkham, *Introduction to Superconductivity*, 2nd ed. (McGraw-Hill, 1996).
- ¹⁷J.-S. Tsai, *Toward a superconducting quantum computer: Harnessing macroscopic quantum coherence*, Proc. Jpn. Acad., Ser. B **86**, 275 (2010).
- ¹⁸U. Vool and M. Devoret, *Introduction to quantum electromagnetic circuits*, Int. J. Circ. Theor. Appl. **45**, 897 (2017).
- ¹⁹L. Mandel and E. Wolf, *Optical Coherence and Quantum Optics* (Cambridge University Press, 1995), Chap. 10.7.
- ²⁰J. Koch, T. M. Yu, J. Gambetta, A. A. Houck, D. I. Schuster, J. Majer, A. Blais, M. H. Devoret, S. M. Girvin, and R. J. Schoelkopf, *Charge-insensitive qubit design derived from the Cooper pair box*, Phys. Rev. A **76**, 042319 (2007).
- ²¹G. Ithier, E. Collin, P. Joyez, P. J. Meeson, D. Vion, D. Esteve, F. Chiarello, A. Shnirman, Y. Makhlin, J. Schrieffer, and G. Schön, *Decoherence in a superconducting quantum bit circuit*, Phys. Rev. B **72**, 134519 (2005).
- ²²O. Astafiev, Yu. A. Pashkin, Y. Nakamura, T. Yamamoto, and J. S. Tsai, *Quantum Noise in the Josephson Charge Qubit*, Phys. Rev. Lett. **93**, 267007 (2004).
- ²³F. Yan, S. Gustavsson, A. Kamal, J. Birenbaum, A. P. Sears, D. Hover, T. J. Gudmundsen, D. Rosenberg, G. Samach, S. Weber, J. L. Yoder, T. P. Orlando, J. Clarke, A. J. Kerman, and W. D. Oliver, *The flux qubit revisited to enhance coherence and reproducibility*, Nat. Commun. **7**, 12964 (2016).
- ²⁴E. Paladino, Y. M. Galperin, G. Falci, and B.L. Altshuler, *1/f noise: Implications for solid-state quantum information*, Rev. Mod. Phys. **86**, 361 (2014).
- ²⁵F. Yoshihara, K. Harrabi, A. O. Niskanen, Y. Nakamura, and J. S. Tsai, *Decoherence of Flux Qubits due to 1/f Flux Noise*, Phys. Rev. Lett. **97**, 167001 (2006).
- ²⁶J. Bylander, S. Gustavsson, F. Yan, F. Yoshihara, K. Harrabi, G. Fitch, D. G. Cory, Y. Nakamura, J.-S. Tsai, and W. D. Oliver, *Noise spectroscopy through dynamical decoupling with a superconducting flux qubit*, Nat. Phys. **7**, 565 (2011).
- ²⁷W. D. Oliver and P. B. Welander, *Materials in superconducting qubits*, MRS Bull. **38**, 816 (2013).
- ²⁸R. Barends, J. Kelly, A. Megrant, D. Sank, E. Jeffrey, Y. Chen, Y. Yin, B. Chiaro, J. Mutus, C. Neill, P. O'Malley, P. Roushan, J. Wenner, T. C. White, A. N. Cleland, and J. M. Martinis, *Coherent Josephson Qubit Suitable for Scalable Quantum Integrated Circuits*, Phys. Rev. Lett. **111**, 080502 (2013).
- ²⁹A. Dunsworth, A. Megrant, C. Quintana, Z. Chen, R. Barends, B. Burkett, B. Foxen, Yu Chen, B. Chiaro, A. Fowler, R. Graff, E. Jeffrey, J. Kelly, E. Lucero, J. Y. Mutus, M. Neeley, C. Neill, P. Roushan, D. Sank, A. Vainsencher, J. Wenner, T. C. White, and J. M. Martinis, *Characterization and reduction of capacitive loss induced by sub-micron Josephson junction fabrication in superconducting qubits*, Appl. Phys. Lett. **111**, 022601 (2017).
- ³⁰Y. Chu, C. Axline, C. Wang, T. Brecht, Y. Y. Gao, L. Frunzio, and R. J. Schoelkopf, *Suspending superconducting qubits by silicon micromachining*, Appl. Phys. Lett. **109**, 112601 (2016).
- ³¹C. Müller, J. H. Cole, and J. Lisenfeld, *Towards understanding two-level-systems in amorphous solids: insights from quantum circuits*, Rep. Prog. Phys. **82**, 124501 (2019).
- ³²C. Wang, C. Axline, Y. Y. Gao, T. Brecht, Y. Chu, L. Frunzio, M. H. Devoret, and R. J. Schoelkopf, *Surface participation and dielectric loss in superconducting qubits*, Appl. Phys. Lett. **107**, 162601 (2015).
- ³³Z. K. Mineev, Z. Leghtas, S. O. Mundhada, L. Christakis, I. M. Pop, M. H. Devoret, *Energy-participation quantization of Josephson circuits*, arXiv:2010.00620.
- ³⁴B. Douçot and L. B. Ioffe, *Physical implementation of protected qubits*, Rep. Prog. Phys. **75**, 072001 (2012).
- ³⁵P. Brooks, A. Kitaev, and J. Preskill, *Protected gates for superconducting qubits*, Phys. Rev. A **87**, 052306 (2013).
- ³⁶M. T. Bell, J. Paramanandam, L. B. Ioffe, and M. E. Gershenson, *Protected Josephson Rhombus Chains*, Phys. Rev. Lett. **112**, 167001 (2014).
- ³⁷J. M. Dempster, B. Fu, D. G. Ferguson, D. I. Schuster, and J. Koch, *Understanding degenerate ground states of a protected quantum circuit in the presence of disorder*, Phys. Rev. B **90**, 094518 (2014).
- ³⁸P. Groszkowski, A. Di Paolo, A. L. Grimsmo, A. Blais, D. I. Schuster, A. A. Houck, and J. Koch, *Coherence properties of the 0- π qubit*, New J. Phys. **20**, 043053 (2018).
- ³⁹A. Gyenis, P. S. Mundada, A. Di Paolo, T. M. Hazard, X. You, D. I. Schuster, J. Koch, A. Blais, and A. A. Houck, *Experimental realization of an intrinsically error-protected superconducting qubit*, arXiv:1910.07542.
- ⁴⁰H. Paik, D. I. Schuster, L. S. Bishop, G. Kirchmair, G. Catelani, A. P. Sears, B. R. Johnson, M. J. Reagor, L. Frunzio, L. I. Glazman, S. M. Girvin, M. H. Devoret, and R. J. Schoelkopf, *Observation of High Coherence in Josephson Junction Qubits Measured in a Three-Dimensional Circuit QED Architecture*,

TABLE V. Useful formulas.

$$\begin{aligned}
e^{\hat{A}} \hat{B} e^{-\hat{A}} &= \hat{B} + [\hat{A}, \hat{B}] + \frac{1}{2!} [\hat{A}, [\hat{A}, \hat{B}]] + \frac{1}{3!} [\hat{A}, [\hat{A}, [\hat{A}, \hat{B}]]] + \frac{1}{4!} [\hat{A}, [\hat{A}, [\hat{A}, [\hat{A}, \hat{B}]]]] + \dots, \\
[\hat{A}\hat{B}, \hat{C}] &= \hat{A}[\hat{B}, \hat{C}] + [\hat{A}, \hat{C}]\hat{B}, \quad [\hat{a}, \hat{a}^\dagger] = 1, \quad [\hat{a}^\dagger \hat{a}, \hat{a}^\dagger] = \hat{a}^\dagger, \quad [\hat{a}^\dagger \hat{a}, \hat{a}] = -\hat{a}, \\
[\hat{\sigma}_x, \hat{\sigma}_y] &= 2i\hat{\sigma}_z, \quad [\hat{\sigma}_y, \hat{\sigma}_z] = 2i\hat{\sigma}_x, \quad [\hat{\sigma}_z, \hat{\sigma}_x] = 2i\hat{\sigma}_y, \\
\hat{\sigma}_\pm &= \frac{\hat{\sigma}_x \pm i\hat{\sigma}_y}{2}, \quad \hat{\sigma}_+ \hat{\sigma}_- = \frac{\hat{\sigma}_z + \hat{I}}{2}, \quad [\hat{\sigma}_z, \hat{\sigma}_\pm] = \pm 2\hat{\sigma}_\pm, \quad [\hat{\sigma}_+, \hat{\sigma}_-] = \hat{\sigma}_z.
\end{aligned}$$

- Phys. Rev. Lett. **107**, 240501 (2011).
- ⁴¹C. Rigetti, J. M. Gambetta, S. Poletto, B. L. T. Plourde, J. M. Chow, A. D. Córcoles, John A. Smolin, S. T. Merkel, J. R. Rozen, G. A. Keefe, M. B. Rothwell, M. B. Ketchen, and M. Steffen, *Superconducting qubit in a waveguide cavity with a coherence time approaching 0.1 ms*, Phys. Rev. B **86**, 100506(R) (2012).
- ⁴²L. B. Nguyen, Y.-H. Lin, A. Somoroff, R. Mencia, N. Grabon, and V. E. Manucharyan, *High-Coherence Fluxonium Qubit*, Phys. Rev. X **9**, 041041 (2019).
- ⁴³M. D. Hutchings, J. B. Hertzberg, Y. Liu, N. T. Bronn, G. A. Keefe, M. Brink, J. M. Chow, and B. L. T. Plourde, *Tunable Superconducting Qubits with Flux-Independent Coherence*, Phys. Rev. Applied **8**, 044003 (2017).
- ⁴⁴G. Rastelli, I. M. Pop, and F. W. J. Hekking, *Quantum phase slips in Josephson junction rings*, Phys. Rev. B **87**, 174513 (2013).
- ⁴⁵T. P. Orlando, J. E. Mooij, L. Tian, C. H. van der Wal, L. S. Levitov, S. Lloyd, and J. J. Mazo, *Superconducting persistent-current qubit*, Phys. Rev. B **60**, 15398 (1999).
- ⁴⁶T. L. Robertson, B. L. T. Plourde, P. A. Reichardt, T. Hime, C.-E. Wu, and J. Clarke, *Quantum theory of three-junction flux qubit with non-negligible loop inductance: Towards scalability*, Phys. Rev. B **73**, 174526 (2006).
- ⁴⁷J. Q. You, X. Hu, S. Ashhab, and F. Nori, *Low-decoherence flux qubit*, Phys. Rev. B **75**, 140515(R) (2007).
- ⁴⁸V. E. Manucharyan, J. Koch, L. I. Glazman, and M. H. Devoret, *Fluxonium: Single Cooper-Pair Circuit Free of Charge Offsets*, Science **326**, 113 (2009).
- ⁴⁹M. Peruzzo, A. Trioni, F. Hassani, M. Zemlicka, and J. M. Fink, *Surpassing the Resistance Quantum with a Geometric Superinductor*, Phys. Rev. Applied **14**, 044055 (2020).
- ⁵⁰O. V. Astafiev, L. B. Ioffe, S. Kafanov, Yu. A. Pashkin, K. Yu. Arutyunov, D. Shahar, O. Cohen, and J. S. Tsai, *Coherent quantum phase slip*, Nature **484**, 355 (2012).
- ⁵¹L. Grünhaupt, M. Spiecker, D. Gusenkova, N. Maleeva, S. T. Skacel, I. Takmakov, F. Valenti, P. Winkel, H. Rotzinger, W. Wernsdorfer, A. V. Ustinov, and I. M. Pop, *Granular aluminium as a superconducting material for high-impedance quantum circuits*, Nat. Mater. **18**, 816 (2019).
- ⁵²I. V. Pechenezhskiy, R. A. Mencia, L. B. Nguyen, Y.-H. Lin, and V. E. Manucharyan, *The superconducting quasicharge qubit*, Nature **585**, 368 (2020).
- ⁵³S. Haroche and J.-M. Raimond, *Exploring the Quantum: Atoms, Cavities, and Photons* (Oxford University Press, 2013).
- ⁵⁴S. M. Girvin, *Circuit QED: superconducting qubits coupled to microwave photons* in *Quantum Machines: Measurement and Control of Engineered Quantum Systems—Lecture Notes of the Les Houches Summer School: Volume 96, July 2011*, edited by M. Devoret, B. Huard, R. Schoelkopf, and L. F. Cugliandolo (Oxford University Press, 2014).
- ⁵⁵A. Blais, R.-S. Huang, A. Wallraff, S. M. Girvin, and R. J. Schoelkopf, *Cavity quantum electrodynamics for superconducting electrical circuits: An architecture for quantum computation*, Phys. Rev. A **69**, 062320 (2004).
- ⁵⁶A. A. Houck, J. A. Schreier, B. R. Johnson, J. M. Chow, J. Koch, J. M. Gambetta, D. I. Schuster, L. Frunzio, M. H. Devoret, S. M. Girvin, and R. J. Schoelkopf, *Controlling the Spontaneous Emission of a Superconducting Transmon Qubit*, Phys. Rev. Lett. **101**, 080502 (2008).
- ⁵⁷S. E. Nigg, H. Paik, B. Vlastakis, G. Kirchmair, S. Shankar, L. Frunzio, M. H. Devoret, R. J. Schoelkopf, and S. M. Girvin, *Black-Box Superconducting Circuit Quantization*, Phys. Rev. Lett. **108**, 240502 (2012).
- ⁵⁸J. Bourassa, F. Beaudoin, J. M. Gambetta, and A. Blais, *Josephson-junction-embedded transmission-line resonators: From Kerr medium to in-line transmon*, Phys. Rev. A **86**, 013814 (2012).
- ⁵⁹M. Leib, F. Deppe, A. Marx, R. Gross, and M. J. Hartmann, *Networks of nonlinear superconducting transmission line resonators*, New J. Phys. **14**, 075024 (2012).
- ⁶⁰F. Solgun, D. W. Abraham, and D. P. DiVincenzo, *Blackbox quantization of superconducting circuits using exact impedance synthesis*, Phys. Rev. B **90**, 134504 (2014).
- ⁶¹N. Didier, J. Bourassa, and A. Blais, *Fast Quantum Nondemolition Readout by Parametric Modulation of Longitudinal Qubit-Oscillator Interaction*, Phys. Rev. Lett. **115**, 203601 (2015).
- ⁶²G. S. Agarwal, *Quantum Optics* (Cambridge University Press, 2012).
- ⁶³P.-M. Billangeon, J. S. Tsai, and Y. Nakamura, *Circuit-QED-based scalable architectures for quantum information processing with superconducting qubits*, Phys. Rev. B **91**, 094517 (2015).
- ⁶⁴S. Richer and D. DiVincenzo, *Circuit design implementing longitudinal coupling: A scalable scheme for superconducting qubits*, Phys. Rev. B **93**, 134501 (2016).
- ⁶⁵X. Wang, A. Miranowicz, and F. Nori, *Ideal Quantum Nondemolition Readout of a Flux Qubit without Purcell Limitations*, Phys. Rev. Applied **12**, 064037 (2019).
- ⁶⁶J. Majer, J. M. Chow, J. M. Gambetta, J. Koch, B. R. Johnson, J. A. Schreier, L. Frunzio, D. I. Schuster, A. A. Houck, A. Wallraff, A. Blais, M. H. Devoret, S. M. Girvin, and R. J. Schoelkopf, *Coupling superconducting qubits via a cavity bus*, Nature **449**, 443 (2007).
- ⁶⁷X.-Y. Lü, S. Ashhab, W. Cui, R. Wu, and F. Nori, *Two-qubit gate operations in superconducting circuits with strong coupling and weak anharmonicity*, New J. Phys. **14**, 073041 (2012).
- ⁶⁸S. Filipp, M. Göppl, J. M. Fink, M. Baur, R. Bianchetti, L. Steffen, and A. Wallraff, *Multimode mediated qubit-qubit coupling and dark-state symmetries in circuit quantum electrodynamics*, Phys. Rev. A **83**, 063827 (2011).
- ⁶⁹B. Schumacher and M. Westmoreland, *Quantum Processes, Systems, and Information* (Cambridge University Press, 2010).
- ⁷⁰C. Gardiner and P. Zoller, *Quantum Noise: A Handbook of Markovian and Non-Markovian Quantum Stochastic Methods with Applications to Quantum Optics*, 3rd ed. (Springer, 2004).
- ⁷¹B. Yurke, *Input-Output Theory*, in *Quantum Squeezing*, edited by P. D. Drummond and Z. Ficek (Springer, 2004).
- ⁷²A. A. Clerk, M. H. Devoret, S. M. Girvin, F. Marquardt, and R. J. Schoelkopf, *Introduction to Quantum Noise, Measurement, and Amplification*, Rev. Mod. Phys. **82**, 1155 (2010).
- ⁷³J. R. Johansson, P. D. Nation, and F. Nori, *QuTiP: An open-source Python framework for the dynamics of open quantum*

- systems, *Comp. Phys. Comm.* **183**, 1760 (2012).
- ⁷⁴J. R. Johansson, P. D. Nation, and F. Nori, *QuTiP 2: A Python framework for the dynamics of open quantum systems*, *Comp. Phys. Comm.* **184**, 1234 (2013).
 - ⁷⁵P. Phillips, *Advanced Solid State Physics*, 2nd ed. (Cambridge University Press, 2012).
 - ⁷⁶C. Cohen-Tannoudji, J. Dupont-Roc, and G. Grynberg, *Atom—Photon Interactions: Basic Process and Applications* (John Wiley & Sons, 1998), p. 41. Note that this book does not use the name Schrieffer–Wolff transformation.
 - ⁷⁷V. B. Braginsky and F. Ya. Khalili, *Quantum Measurement* (Cambridge University Press, 1992).
 - ⁷⁸V. B. Braginsky and F. Ya. Khalili, *Quantum Nondemolition Measurements: the Route from Toys to Tools*, *Rev. Mod. Phys.* **68**, 1 (1996).
 - ⁷⁹J. E. Johnson, C. Macklin, D. H. Slichter, R. Vijay, E. B. Weingarten, J. Clarke, and I. Siddiqi, *Heralded State Preparation in a Superconducting Qubit*, *Phys. Rev. Lett.* **109**, 050506 (2012).
 - ⁸⁰T. Walter, P. Kurpiers, S. Gasparinetti, P. Magnard, A. Potočnik, Y. Salathé, M. Pechal, M. Mondal, M. Oppliger, C. Eichler, and A. Wallraff, *Rapid High-Fidelity Single-Shot Dispersive Readout of Superconducting Qubits*, *Phys. Rev. Applied* **7**, 054020 (2017).
 - ⁸¹J. Gambetta, A. Blais, M. Boissonneault, A. A. Houck, D. I. Schuster, and S. M. Girvin, *Quantum trajectory approach to circuit QED: Quantum jumps and the Zeno effect*, *Phys. Rev. A* **77**, 012112 (2008).
 - ⁸²J. Heinssoo, C. K. Andersen, A. Remm, S. Krinner, T. Walter, Y. Salathé, S. Gasparinetti, J.-C. Besse, A. Potočnik, A. Wallraff, and C. Eichler, *Rapid High-Fidelity Multiplexed Readout of Superconducting Qubits*, *Phys. Rev. Applied* **10**, 034040 (2018).
 - ⁸³A. F. Kockum, A. Miranowicz, S. De Liberato, S. Savasta, and F. Nori, *Ultrastrong coupling between light and matter*, *Nat. Rev. Phys.* **1**, 19 (2019).
 - ⁸⁴P. Forn-Díaz, L. Lamata, E. Rico, J. Kono, and E. Solano, *Ultrastrong coupling regimes of light-matter interaction*, *Rev. Mod. Phys.* **91**, 025005 (2019).
 - ⁸⁵M. D. Reed, B. R. Johnson, A. A. Houck, L. DiCarlo, J. M. Chow, D. I. Schuster, L. Frunzio, and R. J. Schoelkopf, *Fast reset and suppressing spontaneous emission of a superconducting qubit*, *Appl. Phys. Lett.* **96**, 203110 (2010).
 - ⁸⁶E. A. Sete, J. M. Martinis, and A. N. Korotkov, *Quantum theory of a bandpass Purcell filter for qubit readout*, *Phys. Rev. A* **92**, 012325 (2015).
 - ⁸⁷T. Yamamoto, K. Inomata, K. Koshino, P.-M. Billangeon, Y. Nakamura, and J. S. Tsai, *Superconducting flux qubit capacitively coupled to an LC resonator*, *New J. Phys.* **16**, 015017 (2014).
 - ⁸⁸G. Zhu, D. G. Ferguson, V. E. Manucharyan, and J. Koch, *Circuit QED with fluxonium qubits: Theory of the dispersive regime*, *Phys. Rev. B* **87**, 024510 (2013).
 - ⁸⁹T. Yamamoto, K. Inomata, M. Watanabe, K. Matsuba, T. Miyazaki, W. D. Oliver, Y. Nakamura, and J. S. Tsai, *Flux-driven Josephson parametric amplifier*, *Appl. Phys. Lett.* **93**, 042510 (2008).
 - ⁹⁰R. Vijay, M. H. Devoret, and I. Siddiqi, *Invited Review Article: The Josephson bifurcation amplifier*, *Rev. Sci. Instrum.* **80**, 111101 (2009).
 - ⁹¹*The Duffing Equation: Nonlinear Oscillators and Their Behaviour*, edited by I. Kovacic and M. J. Brennan (Wiley, 2011).
 - ⁹²A. Roy and M. Devoret, *Quantum-limited parametric amplification with Josephson circuits in the regime of pump depletion*, *Phys. Rev. B* **98**, 045405 (2018).
 - ⁹³M. A. Castellanos-Beltrana and K. W. Lehnert, *Widely tunable parametric amplifier based on a superconducting quantum interference device array resonator*, *Appl. Phys. Lett.* **91**, 083509 (2007); <https://doi.org/10.1063/1.2773988>
 - ⁹⁴C. Macklin, K. O’Brien, D. Hover, M. E. Schwartz, V. Bolkhovsky, X. Zhang, W. D. Oliver, and I. Siddiqi, *A Near-Quantum-Limited Josephson Traveling-Wave Parametric Amplifier*, *Science* **350**, 307 (2015).
 - ⁹⁵K. O’Brien, C. Macklin, I. Siddiqi, and X. Zhang, *Resonant Phase Matching of Josephson Junction Traveling Wave Parametric Amplifiers*, *Phys. Rev. Lett.* **113**, 157001 (2014).
 - ⁹⁶L. Planat, A. Ranadive, R. Dassonneville, J. P. Martínez, S. Léger, C. Naud, O. Buisson, W. Hasch-Guichard, D. M. Basko, and N. Roch, *Photonic-Crystal Josephson Traveling-Wave Parametric Amplifier*, *Phys. Rev. X* **10**, 021021 (2020).
 - ⁹⁷C. M. Caves, *Quantum limits on noise in linear amplifiers*, *Phys. Rev. D* **26**, 1817 (1982).
 - ⁹⁸C. M. Caves, J. Combes, Z. Jiang, and S. Pandey, *Quantum limits on phase-preserving linear amplifiers*, *Phys. Rev. A* **86**, 063802 (2012).
 - ⁹⁹C. Eichler and A. Wallraff, *Controlling the dynamic range of a Josephson parametric amplifier*, *EPJ Quantum Technol.* **1**, 2 (2014); <https://doi.org/10.1140/epjqt2>
 - ¹⁰⁰H. J. Carmichael, *Statistical Methods in Quantum Optics 2: Non-Classical Fields* (Springer, 2008).
 - ¹⁰¹H. A. Haus, *Electromagnetic Noise and Quantum Optical Measurements* (Springer, 2000).
 - ¹⁰²M. H. Levitt, *Spin Dynamics: Basics of Nuclear Magnetic Resonance*, 2nd ed. (John Wiley & Sons, 2008).
 - ¹⁰³D. C. McKay, C. J. Wood, S. Sheldon, J. M. Chow, and J. M. Gambetta, *Efficient Z gates for quantum computing*, *Phys. Rev. A* **96**, 022330 (2017).
 - ¹⁰⁴L. M. K. Vandersypen and I. L. Chuang, *NMR techniques for quantum control and computation*, *Rev. Mod. Phys.* **76**, 1037 (2005).
 - ¹⁰⁵R. Barends, C.M. Quintana, A.G. Petukhov, Y. Chen, D. Kafri, K. Kechedzhi, R. Collins, O. Naaman, S. Boixo, F. Arute, K. Arya, D. Buell, B. Burkett, Z. Chen, B. Chiaro, A. Dunsworth, B. Foxen, A. Fowler, C. Gidney, M. Giustina, R. Graff, T. Huang, E. Jeffrey, J. Kelly, P.V. Klimov, F. Kostritsa, D. Landhuis, E. Lucero, M. McEwen, A. Megrant, X. Mi, J. Mutus, M. Neeley, C. Neill, E. Ostby, P. Roushan, D. Sank, K.J. Satzinger, A. Vainsencher, T. White, J. Yao, P. Yeh, A. Zalcman, H. Neven, V.N. Smelyanskiy, and J. M. Martinis, *Diabatic Gates for Frequency-Tunable Superconducting Qubits*, *Phys. Rev. Lett.* **123**, 210501 (2019).
 - ¹⁰⁶A. O. Niskanen, K. Harrabi, F. Yoshihara, Y. Nakamura, S. Lloyd, J. S. Tsai, *Quantum Coherent Tunable Coupling of Superconducting Qubits*, *Science* **316**, 723 (2007).
 - ¹⁰⁷R. Barends, J. Kelly, A. Megrant, A. Veitia, D. Sank, E. Jeffrey, T. C. White, J. Mutus, A. G. Fowler, B. Campbell, Y. Chen, Z. Chen, B. Chiaro, A. Dunsworth, C. Neill, P. O’Malley, P. Roushan, A. Vainsencher, J. Wenner, A. N. Korotkov, A. N. Cleland, and J. M. Martinis, *Superconducting quantum circuits at the surface code threshold for fault tolerance*, *Nature* **508**, 500 (2014).
 - ¹⁰⁸Y. Chen, C. Neill, P. Roushan, N. Leung, M. Fang, R. Barends, J. Kelly, B. Campbell, Z. Chen, B. Chiaro, A. Dunsworth, E. Jeffrey, A. Megrant, J.Y. Mutus, P.J.J. O’Malley, C.M. Quintana, D. Sank, A. Vainsencher, J. Wenner, T.C. White, Michael R. Geller, A.N. Cleland, and J. M. Martinis, *Qubit Architecture with High Coherence and Fast Tunable Coupling*, *Phys. Rev. Lett.* **113**, 220502 (2014).
 - ¹⁰⁹S. A. Caldwell, N. Didier, C. A. Ryan, E. A. Sete, A. Hudson, P. Karalekas, R. Manenti, M. P. da Silva, R. Sinclair, E. Acala, N. Alidoust, J. Angeles, A. Bestwick, M. Block, B. Bloom, A. Bradley, C. Bui, L. Capelluto, R. Chilcott, J. Cordova, G. Crossman, M. Curtis, S. Deshpande, T. El Bouayadi, D. Girshovich, S. Hong, K. Kuang, M. Lenihan, T. Manning, A. Marchenkov, J. Marshall, R. Maydra, Y. Mohan, W. O’Brien, C. Osborn, J. Otterbach, A. Papageorge, J.-P. Paquette, M. Pelstring, A. Polloreno, G. Prawiroatmodjo, V. Rawat, M. Reagor, R. Renzas, N. Rubin, D. Russell, M. Rust, D. Scarabelli, M. Scheer, M. Selvanayagam, R. Smith, A. Staley, M. Suska, N. Tezak, D. C. Thompson, T.-W. To, M. Vahidpour, N. Vodrahalli, T. Whyland, K. Yadav, W. Zeng, and C. Rigetti, *Parametrically Activated Entangling Gates Using Transmon Qubits*, *Phys. Rev.*

- Applied **10**, 034050 (2018).
- ¹¹⁰J. M. Chow, A. D. Córcoles, J. M. Gambetta, C. Rigetti, B. R. Johnson, J. A. Smolin, J. R. Rozen, G. A. Keefe, M. B. Rothwell, M. B. Ketchen, and M. Steffen, *Simple All-Microwave Entangling Gate for Fixed-Frequency Superconducting Qubits*, Phys. Rev. Lett. **107**, 080502 (2011).
 - ¹¹¹S. Sheldon, E. Magesan, J. M. Chow, and J. M. Gambetta, *Procedure for systematically tuning up cross-talk in the cross-resonance gate*, Phys. Rev. A **93**, 060302(R) (2016).
 - ¹¹²N. Schuch and J. Siewert, *Natural two-qubit gate for quantum computation using the XY interaction*, Phys. Rev. A **67**, 032301 (2003).
 - ¹¹³J. Zhang, J. Vala, S. Sastry, and K. Birgitta Whaley, *Minimum Construction of Two-Qubit Quantum Operations*, Phys. Rev. Lett. **93**, 020502 (2004).
 - ¹¹⁴A. O. Niskanen, Y. Nakamura, and J.-S. Tsai, *Tunable coupling scheme for flux qubits at the optimal point*, Phys. Rev. B **73**, 094506 (2006).
 - ¹¹⁵S. Poletto, J. M. Gambetta, S. T. Merkel, J. A. Smolin, J. M. Chow, A. D. Córcoles, George A. Keefe, M. B. Rothwell, J. R. Rozen, D. W. Abraham, C. Rigetti, and M. Steffen, *Entanglement of Two Superconducting Qubits in a Waveguide Cavity via Monochromatic Two-Photon Excitation*, Phys. Rev. Lett. **109**, 240505 (2012).
 - ¹¹⁶L. DiCarlo, J. M. Chow, J. M. Gambetta, L. S. Bishop, B. R. Johnson, D. I. Schuster, J. Majer, A. Blais, L. Frunzio, S. M. Girvin, and R. J. Schoelkopf, *Demonstration of two-qubit algorithms with a superconducting quantum processor*, Nature **460**, 240 (2009).
 - ¹¹⁷J. M. Martinis and M. R. Geller, *Fast adiabatic qubit gates using only σ_z control*, Phys. Rev. A **90**, 022307 (2014).
 - ¹¹⁸C. Rigetti and M. Devoret, *Fully microwave-tunable universal gates in superconducting qubits with linear couplings and fixed transition frequencies*, Phys. Rev. B **81**, 134507 (2010).
 - ¹¹⁹J. L. Allen, R. Kosut, J. Joo, P. Leek, and E. Ginossar, *Optimal control of two qubits via a single cavity drive in circuit quantum electrodynamics*, Phys. Rev. A **95**, 042325 (2017).
 - ¹²⁰V. Tripathi, M. Khezri, and A. N. Korotkov, *Operation and intrinsic error budget of a two-qubit cross-resonance gate*, Phys. Rev. A **100**, 012301 (2019).
 - ¹²¹A. Abragam and M. Goldman, *Principles of Dynamic Nuclear Polarisation*, Rep. Prog. Phys. **41**, 395 (1978).
 - ¹²²C. P. Slichter, *Principles of Magnetic Resonance*, 3rd ed. (Springer, 1990).
 - ¹²³D. J. Egger, M. Werninghaus, M. Ganzhorn, G. Salis, A. Fuhrer, P. Müller, and S. Filipp, *Pulsed Reset Protocol for Fixed-Frequency Superconducting Qubits*, Phys. Rev. Applied **10**, 044030 (2018).
 - ¹²⁴P. Magnard, P. Kurpiers, B. Royer, T. Walter, J.-C. Besse, S. Gasparinetti, M. Pechal, J. Heinsoo, S. Storz, A. Blais, and A. Wallraff, *Fast and Unconditional All-Microwave Reset of a Superconducting Qubit*, Phys. Rev. Lett. **121**, 060502 (2018).
 - ¹²⁵A. Blais, J. Gambetta, A. Wallraff, D. I. Schuster, S. M. Girvin, M. H. Devoret, and R. J. Schoelkopf, *Quantum-information processing with circuit quantum electrodynamics*, Phys. Rev. A **75**, 032329 (2007).
 - ¹²⁶D. Ristè, C. C. Bultink, K. W. Lehnert, and L. DiCarlo, *Feedback Control of a Solid-State Qubit Using High-Fidelity Projective Measurement*, Phys. Rev. Lett. **109**, 240502 (2012).
 - ¹²⁷P. Campagne-Ibarcq, E. Flurin, N. Roch, D. Darson, P. Morfin, M. Mirrahimi, M. H. Devoret, F. Mallet, and B. Huard, *Persistent Control of a Superconducting Qubit by Stroboscopic Measurement Feedback*, Phys. Rev. X **3**, 021008 (2013).
 - ¹²⁸Y. Salathé, P. Kurpiers, T. Karg, C. Lang, C. Kraglund Andersen, A. Akin, S. Krinner, C. Eichler, and A. Wallraff, *Low-Latency Digital Signal Processing for Feedback and Feedforward in Quantum Computing and Communication*, Phys. Rev. Applied **9**, 034011 (2018).
 - ¹²⁹N. Cottet, S. Jezouin, L. Bretheau, P. Campagne-Ibarcq, Q. Ficheux, J. Anders, A. Auffèves, R. Azouit, P. Rouchon, and B. Huard, *Observing a quantum Maxwell demon at work*, Proc. Natl. Acad. Sci. USA **114**, 7561 (2017).
 - ¹³⁰Y. Masuyama, K. Funo, Y. Murashita, A. Noguchi, S. Kono, Y. Tabuchi, R. Yamazaki, M. Ueda, and Y. Nakamura, *Information-to-work conversion by Maxwell's demon in a superconducting circuit quantum electrodynamical system*, Nat. Commun. **9**, 1291 (2018).
 - ¹³¹M. Naghiloo, J.J. Alonso, A. Romito, E. Lutz, and K.W. Murch, *Information Gain and Loss for a Quantum Maxwell's Demon*, Phys. Rev. Lett. **121**, 030604 (2018).
 - ¹³²A. Y. Kitaev, *Fault-tolerant quantum computation by anyons*, Annals of Physics **303**, 2 (2003).
 - ¹³³A. G. Fowler, M. Mariantoni, J. M. Martinis, and A. N. Cleland, *Surface codes: Towards practical large-scale quantum computation*, Phys. Rev. A **86**, 032324 (2012).
 - ¹³⁴D. Gottesman, *An Introduction to Quantum Error Correction and Fault-Tolerant Quantum Computation*, in *Quantum Information Science and Its Contributions to Mathematics* edited by S. J. Lomonaco Jr., Proceedings of Symposia in Applied Mathematics **68**, 13 (2010); <http://dx.doi.org/10.1090/psapm/068/2762145>
 - ¹³⁵S. J. Devitt, W. J. Munro, and K. Nemoto, *Quantum error correction for beginners*, Rep. Prog. Phys. **76**, 076001 (2013).
 - ¹³⁶D. A. Lidar and T. A. Brun (eds.), *Quantum Error Correction*, (Cambridge University Press, 2013).
 - ¹³⁷B. M. Terhal, *Quantum error correction for quantum memories*, Rev. Mod. Phys. **87**, 307 (2015).
 - ¹³⁸E. Campbell, B. Terhal, and C. Vuillot, *Roads towards fault-tolerant universal quantum computation*, Nature **549**, 172 (2017); <https://doi.org/10.1038/nature23460>
 - ¹³⁹D. Gottesman, *Stabilizer Codes and Quantum Error Correction*, arXiv:quant-ph/9705052.
 - ¹⁴⁰D. Gottesman, *The Heisenberg Representation of Quantum Computers*, arXiv:quant-ph/9807006.
 - ¹⁴¹A. Paler, S. Devitt, K. Nemoto, and I. Polian, *Software-based Pauli tracking in fault-tolerant quantum circuits*, 2014 Design, Automation and Test in Europe Conference & Exhibition (DATE), 1-4 (2014).
 - ¹⁴²C. Horsman, A. G. Fowler, S. Devitt, and R. V. Meter, *Surface code quantum computing by lattice surgery*, New J. Phys. **14**, 123011 (2012).
 - ¹⁴³S. J. Devitt, A. G. Fowler, T. Tilma, W. J. Munro, and K. Nemoto, *Classical processing requirements for a topological quantum computing system*, Int. J. Quant. Inf. **8**, 121 (2010).
 - ¹⁴⁴S. Bravyi and A. Kitaev, *Universal quantum computation with ideal Clifford gates and noisy ancillas*, Phys. Rev. A **71**, 022316 (2005).
 - ¹⁴⁵A. M. Meier, B. Eastin, and E. Knill, *Magic-state distillation with the four-qubit code*, Quantum Inf. Comput. **13**, 195 (2013).
 - ¹⁴⁶L. M. K. Vandersypen, H. Bluhm, J. S. Clarke, A. S. Dzurak, R. Ishihara, A. Morello, D. J. Reilly, L. R. Schreiber, and M. Veldhorst, *Interfacing spin qubits in quantum dots and donors—hot, dense, and coherent*, npj Quantum Inf. **3**, 34 (2017).
 - ¹⁴⁷D. Rosenberg, D. Kim, R. Das, D. Yost, S. Gustavsson, D. Hover, P. Krantz, A. Melville, L. Racz, G. O. Samach, S. J. Weber, F. Yan, J. L. Yoder, A. J. Kerman, and W. D. Oliver, *3D integrated superconducting qubits*, npj Quantum Inf. **3**, 1 (2017).
 - ¹⁴⁸B. Foxen, J. Y. Mutus, E. Lucero, E. Jeffrey, D. Sank, R. Barends, K. Arya, B. Burkett, Y. Chen, Z. Chen, B. Chiaro, A. Dunsworth, A. Fowler, C. Gidney, M. Giustina, R. Graff, T. Huang, J. Kelly, P. Klimov, A. Megrant, O. Naaman, M. Neeley, C. Neill, C. Quintana, P. Roushan, A. Vainsencher, J. Wenner, T. C. White, and J. M. Martinis, *High speed flux sampling for tunable superconducting qubits with an embedded cryogenic transducer*, Supercond. Sci. Technol. **32**, 015012 (2018).
 - ¹⁴⁹N. T. Bronn, V. P. Adiga, S. B. Olivadese, X. Wu, J. M. Chow, and D. P. Pappas, *High coherence plane breaking packaging for superconducting qubits*, Quantum Sci. Technol. **3**, 024007 (2018).

- ¹⁵⁰M. Vahidpour, W. O'Brien, J. T. Whyland, J. Angeles, J. Marshall, D. Scarabelli, G. Crossman, K. Yadav, Y. Mohan, C. Bui, V. Rawat, R. Renzas, N. Vodrahalli, A. Bestwick, and C. Rigetti, *Superconducting Through-Silicon Vias for Quantum Integrated Circuits*, arXiv:1708.02226 (2017).
- ¹⁵¹D. R. W. Yost, M. E. Schwartz, J. Mallek, D. Rosenberg, C. Stull, J. L. Yoder, G. Calusine, M. Cook, R. Das, A. L. Day, E. B. Golden, D. K. Kim, A. Melville, B. M. Niedzielski, W. Woods, A. J. Kerman, and W. D. Oliver, *Solid-state qubits integrated with superconducting through-silicon vias*, npj Quantum Inf. **6**, 59 (2020).
- ¹⁵²H. Mukai, K. Sakata, S. J. Devitt, R. Wang, Y. Zhou, Y. Nakajima, and J. S. Tsai, *Pseudo-2D superconducting quantum computing circuit for the surface code: proposal and preliminary tests*, New J. Phys. **22**, 043013 (2020).
- ¹⁵³F. Yoshihara, Y. Nakamura, F. Yan, S. Gustavsson, J. Bylander, W. D. Oliver, and J.-S. Tsai, *Flux qubit noise spectroscopy using Rabi oscillations under strong driving conditions*, Phys. Rev. B **89**, 020503(R) (2014).
- ¹⁵⁴D. P. Burum, M. Under, and R. R. Ernst, *A new "tune-up" NMR pulse cycle for minimizing and characterizing phase transients*, J. Magn. Reson. **43**, 463 (1981).
- ¹⁵⁵B. M. Vlastakis, *Controlling Coherent State Superpositions with Superconducting Circuits*, PhD thesis, Yale University (2015).
- ¹⁵⁶J. Kelly, R. Barends, B. Campbell, Y. Chen, Z. Chen, B. Chiaro, A. Dunsworth, A. G. Fowler, I.-C. Hoi, E. Jeffrey, A. Megrant, J. Mutus, C. Neill, P. J. J. O'Malley, C. Quintana, P. Roushan, D. Sank, A. Vainsencher, J. Wenner, T. C. White, A. N. Cleland, and J. M. Martinis, *Optimal Quantum Control Using Randomized Benchmarking*, Phys. Rev. Lett. **112**, 240504 (2014).
- ¹⁵⁷M. Werninghaus, D. J. Egger, F. Roy, S. Machnes, F. K. Wilhelm, and S. Filipp, *Leakage reduction in fast superconducting qubit gates via optimal control*, arXiv:2003.05952.
- ¹⁵⁸J. Kelly, R. Barends, A. G. Fowler, A. Megrant, E. Jeffrey, T. C. White, D. Sank, J. Y. Mutus, B. Campbell, Yu Chen, Z. Chen, B. Chiaro, A. Dunsworth, E. Lucero, M. Neeley, C. Neill, P. J. J. O'Malley, C. Quintana, P. Roushan, A. Vainsencher, J. Wenner, and J. M. Martinis, *Scalable in situ qubit calibration during repetitive error detection*, Phys. Rev. A **94**, 032321 (2016).
- ¹⁵⁹J. Kelly, P. O'Malley, M. Neeley, H. Neven, and J. M. Martinis, *Physical qubit calibration on a directed acyclic graph*, arXiv:1803.03226.
- ¹⁶⁰C. Neill, P. Roushan, K. Kechedzhi, S. Boixo, S. V. Isakov, V. Smelyanskiy, A. Megrant, B. Chiaro, A. Dunsworth, K. Arya, R. Barends, B. Burkett, Y. Chen, Z. Chen, A. Fowler, B. Foxen, M. Giustina, R. Graff, E. Jeffrey, T. Huang, J. Kelly, P. Klimov, E. Lucero, J. Mutus, M. Neeley, C. Quintana, D. Sank, A. Vainsencher, J. Wenner, T. C. White, H. Neven, and J. M. Martinis, *A blueprint for demonstrating quantum supremacy with superconducting qubits*, Science **360**, 195 (2018).
- ¹⁶¹D. D'Alessandro, *Introduction to Quantum Control and Dynamics* (Chapman and Hall/CRC, 2007).
- ¹⁶²I. N. Hincks, C. E. Granade, T. W. Borneman, and D. G. Cory, *Controlling Quantum Devices with Nonlinear Hardware*, Phys. Rev. Applied **4**, 024012 (2015).
- ¹⁶³F. K. Wilhelm, S. Kirchhoff, S. Machnes, N. Witter, and D. Sugny, *An introduction into optimal control for quantum technologies*, arXiv:2003.10132.
- ¹⁶⁴P. Rembold, N. Oshnik, M. M. Müller, S. Montangero, T. Calarco, and E. Neu, *Introduction to quantum optimal control for quantum sensing with nitrogen-vacancy centers in diamond*, AVS Quantum Sci. **2**, 024701 (2020).
- ¹⁶⁵R. R. Ernst, G. Bodenhausen, and A. Wokaun, *Principles of Nuclear Magnetic Resonance in One and Two Dimensions* (Oxford University Press, 1987).
- ¹⁶⁶R. Freeman, *Shaped radiofrequency pulses in high resolution NMR*, Prog. Nucl. Magn. Reson. Spectrosc. **32**, 59 (1998).
- ¹⁶⁷C. Bauer, R. Freeman, T. Frenkiel, J. Keeler, A. J. Shaka, *Gaussian pulses*, J. Magn. Reson. **58**, 442 (1984).
- ¹⁶⁸J. M. Gambetta, F. Motzoi, S. T. Merkel, and F. K. Wilhelm, *Analytic control methods for high-fidelity unitary operations in a weakly nonlinear oscillator*, Phys. Rev. A **83**, 012308 (2011).
- ¹⁶⁹F. Motzoi, J. M. Gambetta, P. Rebentrost, and F. K. Wilhelm, *Simple Pulses for Elimination of Leakage in Weakly Nonlinear Qubits*, Phys. Rev. Lett. **103**, 110501 (2009).
- ¹⁷⁰F. Motzoi, *Controlling Quantum Information Devices*, PhD thesis, University of Waterloo (2012).
- ¹⁷¹D. Guéry-Odelin, A. Ruschhaupt, A. Kiely, E. Torrontegui, S. Martínez-Garaot, and J. G. Muga, *Shortcuts to adiabaticity: Concepts, methods, and applications*, Rev. Mod. Phys. **91**, 045001 (2019).
- ¹⁷²L. S. Theis, F. Motzoi, S. Machnes, and F. K. Wilhelm, *Counteracting systems of diabolicities using DRAG controls: The status after 10 years*, EPL **123**, 60001 (2018).
- ¹⁷³D. I. Hoult, *Fast recovery, high sensitivity NMR probe and preamplifier for low frequencies*, Rev. Sci. Instrum. **50**, 193 (1979).
- ¹⁷⁴J. Butscher, *Shaping of Fast Flux Pulses for Two-Qubit Gates: Inverse Filtering*, master thesis, ETH Zürich (2018).
- ¹⁷⁵M. A. Rol, L. Ciorciaro, F. K. Malinowski, B. M. Tarasinski, R. E. Sagastizabal, C. C. Bultink, Y. Salathe, N. Haandbaek, J. Sedivy, and L. DiCarlo, *Time-domain characterization and correction of on-chip distortion of control pulses in a quantum processor*, Appl. Phys. Lett. **116**, 054001 (2020).
- ¹⁷⁶T. W. Borneman and D. G. Cory, *Bandwidth-limited control and ringing suppression in high-Q resonators*, J. Magn. Reson. **225**, 120 (2012).
- ¹⁷⁷D. E. Kirk, *Optimal Control Theory: An Introduction* (Dover, 2004).
- ¹⁷⁸https://qucontrol.github.io/krotov/v1.2.0/11_other_methods.html
- ¹⁷⁹N. Khaneja, T. Reiss, C. Kehlet, T. Schulte-Herbrüggen, S. J. Glaser, *Optimal Control of Coupled Spin Dynamics: Design of NMR Pulse Sequences by Gradient Ascent Algorithms*, J. Magn. Reson. **172**, 296 (2005).
- ¹⁸⁰C. J. Wood, I. N. Hincks, and C. E. Granade, *QuantumUtils for mathematica*, <http://quantumutils.org> (2015).
- ¹⁸¹F. Motzoi, J. M. Gambetta, S. T. Merkel, and F. K. Wilhelm, *Optimal control methods for rapidly time-varying Hamiltonians*, Phys. Rev. A **84**, 022307 (2011).
- ¹⁸²E. L. Hahn, *Spin Echoes*, Phys. Rev. **80**, 580 (1950).
- ¹⁸³H. Y. Carr and E. M. Purcell, *Effects of Diffusion on Free Precession in Nuclear Magnetic Resonance Experiments*, Phys. Rev. **94**, 630 (1954).
- ¹⁸⁴S. Meiboom and D. Gill, *Modified Spin-Echo Method for Measuring Nuclear Relaxation Times*, Rev. Sci. Instrum. **29**, 688 (1958).
- ¹⁸⁵A. Sodickson and D. G. Cory, *A generalized k-space formalism for treating the spatial aspects of a variety of NMR experiments*, Prog. Nucl. Magn. Reson. Spectrosc. **33**, 77 (1998).
- ¹⁸⁶A. M. Souza, G. A. Álvarez, and D. Suter, *Robust dynamical decoupling*, Phil. Trans. R. Soc. A **370**, 4748 (2012).
- ¹⁸⁷D. A. Lidar, *Review of Decoherence-Free Subspaces, Noiseless Subsystems, and Dynamical Decoupling*, Adv. Chem. Phys. **154**, 295 (2014).
- ¹⁸⁸L. Cywiński, R. M. Lutchyn, C. P. Nave, and S. Das Sarma, *How to enhance dephasing time in superconducting qubits*, Phys. Rev. B **77**, 174509 (2008).
- ¹⁸⁹A. A. Maudsley, *Modified Carr-Purcell-Meiboom-Gill sequence for NMR fourier imaging applications*, J. Magn. Reson. **69**, 488 (1986).
- ¹⁹⁰T. Gullion, D. B. Baker, and M. S. Conradi, *New, compensated Carr-Purcell sequences*, J. Magn. Reson. **89**, 479 (1990).
- ¹⁹¹U. Haeberlen, *High Resolution NMR in Solids: Selective Averaging* (Academic Press, 1976); <https://doi.org/10.1016/B978-0-12-025561-0.X5001-1>
- ¹⁹²A. Brinkmann, *Introduction to average Hamiltonian theory. I. Basics*, Concepts Magn. Reson. Part A **45A**, e21414 (2016).
- ¹⁹³H. Haas, D. Puzzuoli, F. Zhang, and D. G. Cory, *Engineering effective Hamiltonians*, New J. Phys. **21**, 103011 (2019).
- ¹⁹⁴E. Magesan, J. M. Gambetta, and J. Emerson, *Scalable and Ro-*

- bust Randomized Benchmarking of Quantum Processes*, Phys. Rev. Lett. **106**, 180504 (2011).
- ¹⁹⁵E. Magesan, J. M. Gambetta, B. R. Johnson, C. A. Ryan, J. M. Chow, S. T. Merkel, M. P. da Silva, G. A. Keefe, M. B. Rothwell, T. A. Ohki, M. B. Ketchen, and M. Steffen, *Efficient Measurement of Quantum Gate Error by Interleaved Randomized Benchmarking*, Phys. Rev. Lett. **109**, 080505 (2012).
- ¹⁹⁶A. Carignan-Dugas, J. J. Wallman, and J. Emerson, *Bounding the average gate fidelity of composite channels using the unitarity*, New J. Phys. **21**, 053016 (2019).
- ¹⁹⁷S. Aaronson and D. Gottesman, *Improved simulation of stabilizer circuits*, Phys. Rev. A **70**, 052328 (2004).
- ¹⁹⁸A. Erhard, J. J. Wallman, L. Postler, M. Meth, R. Stricker, E. A. Martinez, P. Schindler, T. Monz, J. Emerson, and R. Blatt, *Characterizing large-scale quantum computers via cycle benchmarking*, Nat. Commun. **10**, 5347 (2019).